UNIVERSITY OF CALIFORNIA
RIVERSIDE

# Plasmonic Nanowire Waveguide for Chemical Sensing and Imaging at Nanoscale

A Dissertation submitted in partial satisfaction
of the requirements for the degree of

Doctor of Philosophy

in

Chemical and Environmental Engineering

by

Sanggon Kim

June 2018

Dissertation Committee:
Dr. Ruoxue Yan, Chairperson
Dr. Juchen Guo
Dr. Bryan M. Wong

The Dissertation of Sanggon Kim is approved:

_____

_____

_____

Committee Chairperson

University of California, Riverside

**Acknowledgements**

First and foremost, I would like to express my sincere gratitude to my PhD adviser, Prof. Ruoxue Yan for her, patience, constant support, and invaluable guidance of the research with enthusiasm during my time at UCR.

I also would like to thank Prof. Ming Liu for his guidance which helped me navigate my way through physics which I could not have experienced and achieved without working with him. He has helped me considerably in understanding the physics behind many of the measurements in my research.

I also would like to acknowledge the valuable insights provided by Prof. Juchen Guo and Prof. Bryan Wong as members of my dissertation committee.

I am also indebted to Prof. Yeonho Im and Nosang Myung for his extremely helpful consultations about my career as a researcher.

This journey would have been a lot more difficult without my lab mates. I would also like to express my thanks and appreciation to all the friendly and wonderful lab mates in both the Yan and Liu groups, my first lab mate Peter, who spent much times and efforts to build the new lab with me for the first year; Qiushi, who I had excellent discussion about and also helped me understand the physics behind the research since the very beginning; Yangzhi, who took care of all the things in our lab and who I spent the most of my time in the lab; Xuezhi, who spent much time to help k-space images; Ning, who provided sharp silver nanowires for my research; Lenny, who discussed late night about SERS listening to loud music; Da, who I shared ideas about CNTs.

Next, I am extremely grateful for my family, specifically my parents, Hoyup and Upja, for their love and support. My brothers Taeyeol and Kijong and my sisters in law have also been a source of support and inspired me to pursue my ambitions without giving up.

Last but not least, I would like to dedicate this work to my lovely wife, Eunseon. I would not have come this far if I was not with her. I appreciate my big girl Mina, for the patience that she shows for the past year although I could not spend enough time with her. I also appreciate my little girl Damhee, for being born healthy during my dissertation preparation.

I also would like to specially thank my parents in law, Yeongtaek and Okhui who allow me to marry such a lovely woman and have two beautiful princesses and for their continuous support and words of encouragement which kept me going.

Sanggon Kim

Riverside, California,

June 2018

ABSTRACT OF THE DISSERTATION

Plasmonic Nanowire Waveguide for Chemical Sensing and Imaging at Nanoscale

by

Sanggon Kim

Doctor of Philosophy,
Graduate Program in Chemical and Environmental Engineering
University of California, Riverside, June 2018
Dr. Ruoxue Yan, Chairperson

In the past century, electric current dominated the field of information generation, transportation, and process. In the last decades, the photon has been replacing the electric current due to its extraordinarily large bandwidth and faster transmission speed. 1D nanostructures possess an exceptional advantage over the other nanostructures for the guidance of light because it has a smaller small footprint and high mechanical stability and flexibility and requires low materials. Metal nanowires that are synthesized with a polyol method exhibit atomically smooth surface, high crystallinity, and low impurities, has been intensively studied recently due to its ability of deep-subwavelength confinement. Recently, localized surface plasmon resonance (LSPS) using a plasmonic hotspot formed in the gap (<5nm) remotely excited by metallic nanowire waveguide have stirred-up great research interests in chemical imaging and sensing. In this work, I seek to improve the performance and reliability of chemical imaging and analysis at the nanoscale by developing an effective method for the confinement and guidance of the light. The enabling technology is a novel adiabatic nanofocusing to concentrate light to a nano-confined Raman sensing volume with

high efficiency and energy throughput. Here, the adiabatic means no energy loss in the process of focusing light at the nanoscale. The critical component of the adiabatic nanofocusing is selective excitation of fundamental surface plasmon polariton (SPP) modes in AgNW using a tapered optical fiber with a minimal scattering and propagation losses. The SPP propagates along the NW and eventually creates a localized light at the sharp NW tip, with a hotspot size (<5nm). This optical path can be used not only for concentrating of light to but also extracting the vibrational spectra from the hot spot. Compared to the objective lens based conventional light focusing method, this NW waveguide works as a tunnel for light to propagates without a significant propagation loss due to a high absorption or diffraction in or reflection from the liquid sample. Therefore, imaging or sensing in the liquid phase is also available such as living cell analysis in culture media. The versatility and performance of our adiabatic nanofocusing were successfully demonstrated by measuring Raman spectra of specific molecules on the solid surface and in a single living cell. The transformative advances in light focusing and extracting are instrumental in increasing the prevalence of chemical imaging and analysis at the nanoscale as a practical, reliable and powerful tool for researchers in materials science, catalysis, energy conversion, electronics, and biology. This novel light focusing technique will be the pillar of the chemical imaging and analysis at the nanoscale and contribute to innovative findings in diverse scientific fields in the future.

# Table of Contents

# List of Figures

# List of Tables

# Chapter 1

# Introduction: One-dimensional nanostructure waveguide

Photon as a transporter for tele/data communication has shown remarkable performance regarding bandwidth and high transmission speed. As a result, the photon continues to dominate the fields that electric current ruled for the last century. Long distance communication was firstly replaced by optical fiber, and now it is moving to chip-to-chip scale optical circuits. For the last two decades, nanowire (NW) has attracted intensive attention as a promising candidate for the path of the light for the optical circuits due to its small footprint, low cost, and low power consumption. Photonics has also dominated material characteristics due to its high sensitivity and fast response time. Above all, photon-matter interactions provide a unique property of the materials which allows for compositional characteristics. Further demand for improvement of sensitivity with a high spatial and temporal resolution has prompted attempts to use NW for the guidance of light. In this chapter, we are going to classify the NW waveguide into metal or dielectric and describe the detailed differences of the two materials including optical properties, synthesis, and pros and cons in regard to applications that have demonstrated with remarkable performances recently in the fields that have brought or will bring a significant impact or change to our life. Due to the limited space, covering too many details is not available. We recommend referring to references for further details.

## 1.1. Light propagation in dielectric and metallic nanowire waveguide

### 1.1.1. Wave equation

In this chapter, we will consider only linear, isotropic and nonmagnetic media for the sake of simplicity.

The propagation of light within or on the surface of nanowires that there are no free electric charges can be described in the frame of classical Maxwell equations:

$$\boldsymbol{\nabla} \cdot \mathbf{D} = 0 \tag{1}$$

$$\boldsymbol{\nabla} \cdot \boldsymbol{B} = 0 \tag{2}$$

$$\boldsymbol{\nabla} \times \boldsymbol{E} = -\frac{\partial \mathbf{B}}{\partial \mathbf{t}} \tag{3}$$

$$\boldsymbol{\nabla} \times \boldsymbol{H} = \boldsymbol{J} + \frac{\partial \boldsymbol{D}}{\partial \boldsymbol{t}} \tag{4}$$

where D is electric field displacement vector, B is magnetic flux density vector, $J$ is current density vector and $\boldsymbol{\nabla}$ and $\times$ denote divergence and **c**url operator respectively.

The constitutive relations are then given by:

$$\boldsymbol{D} = \varepsilon_0 \varepsilon \boldsymbol{E} \tag{5}$$

$$\boldsymbol{B} = \mu_0 \mu \boldsymbol{H} \tag{6}$$

$$\boldsymbol{J} = \sigma \boldsymbol{E} \tag{7}$$

Where $\varepsilon$ is the relative permittivity or dielectric constant, $\mu$ is the relative permeability which is 1 in the case of nonmagnetic medium, σ is the conductivity of the material.

By substitution of the constitutive relations, Maxwell equations can be given by:

$$\boldsymbol{\nabla} \cdot \mathbf{E} = 0 \tag{8}$$

$$\boldsymbol{\nabla} \cdot \boldsymbol{H} = 0 \tag{9}$$

$$\boldsymbol{\nabla} \times \boldsymbol{E} = -\mu \frac{\partial \mathbf{H}}{\partial \mathbf{t}} \tag{10}$$

$$\boldsymbol{\nabla} \times \boldsymbol{H} = \sigma \boldsymbol{E} + \varepsilon \frac{\partial \boldsymbol{E}}{\partial \boldsymbol{t}} \tag{11}$$

For the time-harmonic waves, electrical conductivity can be included in the generalized dielectric permittivity $\varepsilon_g$,

$$\varepsilon_g = \varepsilon - i\sigma/\omega \tag{12}$$

Using vector identities, combination of the four Maxwell equations can be simplified in the following forms:

$$\nabla^2 \mathrm{U} + k^2 U = 0 \tag{13}$$

Which is known as Helmholtz equation where U denotes E and H vector fields and k is defined as

$$k = \omega(\varepsilon_g \mu_0)^{1/2} = n k_0 \tag{14}$$

For the waveguide in a Cartesian coordinate aligned along the z-direction, the propagating waves at the surface boundary can be described as:

$$E(r,t) = E(x,y)e^{i(\omega t - \beta z)} \tag{15}$$

$$H(r,t) = H(x,y)e^{i(\omega t - \beta z)} \tag{16}$$

Where $\beta$ is $k_z$, propagation constant of traveling waves.

By substituting equations (15 and 16) into the Maxwell equations, the following relations can be obtained:

$$\frac{\partial \boldsymbol{E_z}}{\partial y} - \frac{\partial \boldsymbol{E_y}}{\partial z} = -\boldsymbol{i\omega}\mu_0 \boldsymbol{H_x} \tag{17}$$

$$\frac{\partial \boldsymbol{E_x}}{\partial z} - \frac{\partial \boldsymbol{E_z}}{\partial x} = -\boldsymbol{i\omega}\mu_0 \boldsymbol{H_y} \tag{18}$$

$$\frac{\partial \boldsymbol{E_y}}{\partial x} - \frac{\partial \boldsymbol{E_x}}{\partial y} = -\boldsymbol{i\omega}\mu_0 \boldsymbol{H_z} \tag{19}$$

$$\frac{\partial \boldsymbol{H_z}}{\partial y} - \frac{\partial \boldsymbol{H_y}}{\partial z} = -\boldsymbol{i\omega}\mu_0 \boldsymbol{E_x} \tag{20}$$

$$\frac{\partial \boldsymbol{H_x}}{\partial z} - \frac{\partial \boldsymbol{H_z}}{\partial x} = -\boldsymbol{i\omega}\mu_0 \boldsymbol{E_y} \tag{21}$$

$$\frac{\partial \boldsymbol{H_y}}{\partial x} - \frac{\partial \boldsymbol{H_x}}{\partial y} = -\boldsymbol{i\omega}\mu_0 \boldsymbol{E_z} \tag{22}$$

For cylindrical coordinates, the Maxwell equations can be expressed as:

$$\frac{1}{\rho}\frac{\partial \boldsymbol{H_z}}{\partial \varphi} - \boldsymbol{i}k_z \boldsymbol{H}_\varphi = -\boldsymbol{i\omega\varepsilon_g E_\rho} \tag{23}$$

$$ik_z \boldsymbol{H_\rho} - \frac{\partial \boldsymbol{H_z}}{\partial \rho} = -\boldsymbol{i\omega\varepsilon_g E_\varphi} \tag{24}$$

$$\frac{1}{\rho}\left[\frac{\partial (\rho \boldsymbol{H_\varphi})}{\partial \rho} - \frac{\partial \boldsymbol{H_\rho}}{\partial \varphi}\right] = -\boldsymbol{i\omega\varepsilon_g E_z} \tag{25}$$

$$\frac{1}{\rho}\frac{\partial \boldsymbol{E_z}}{\partial \varphi} - \boldsymbol{i}k_z \boldsymbol{E H}_\varphi = \boldsymbol{i\omega\mu_0 H_\rho} \tag{25}$$

$$ik_z \boldsymbol{E_\rho} - \frac{\partial \boldsymbol{E_z}}{\partial \rho} = \boldsymbol{i\omega\mu_0 H_\varphi} \tag{26}$$

$$\frac{1}{\rho}\left[\frac{\partial (\rho \boldsymbol{E_\varphi})}{\partial \rho} - \frac{\partial \boldsymbol{HE_\rho}}{\partial \varphi}\right] = \boldsymbol{i\omega\mu_0 H_z} \tag{27}$$

Where $\beta$ is $k_z$, the propagation constant of traveling waves.

The final step to obtain a full description of the electromagnetic fields, we need to apply a set of constraints on the surface called boundary conditions to the derived differential equations.

### 1.1.2. *Waveguide mode*

Field distributions in and near the nanowires can be calculated with four Maxwell equations, appropriate boundary conditions, and polarization. Field distributions for the

waveguide with complex geometry such as tapered, bent nanowire or non-rectangular or circular waveguides such as pentagonal cross-sections or anisotropic materials the solutions often rely on numerical finite difference time domain (FDTD) calculation program. Understanding the principle or phenomenon occurs near the surface boundary already accomplish one's goal for the calculation of the field distributions. In the following, therefore, we only consider guided modes with a certain polarization in planner waveguides in Cartesian coordinate for the simplicity and try to understand the field distributions on the near the boundary.

In this chapter, we will consider only linear, isotropic and nonmagnetic media for the sake of simplicity.

#### *1.1.2.1. Dielectric waveguide*

In a dielectric waveguide, the light is guided by total internal reflection. When a plane wave passing through a boundary layer from a medium with a high refractive index ($n_1$) to the one with a low refractive index ($n_2$), the total internal reflection occurs if an incident angle is smaller than the critical angle $\theta_c = \sin^{-1}\left(\frac{n_2}{n_1}\right)$.

To confine light with a wavelength larger than the radius of nanowire waveguide, larger contrast between core and cladding is necessary. Air is typically chosen as a cladding because it has the lowest refractive index($n_{air}$=1). At least 1.5 refractive index is required for the confinement of light within the core tightly.

**TE-modes**

To confine and guide light tightly in the waveguide, propagation constant (β) must larger than $k_0 n_{cladding}$ where $k_0$ is a wave vector of light in vacuum. For TE modes, $E_y = E_z = 0$ and $H_y = 0$. Thus, the wave equations can be simplified after combining adequately

$$\frac{\partial^2 E_y}{\partial x^2} + [k_0^2 n^2 - \beta^2] E_y = 0 \tag{28}$$

where $k = \sqrt{k_0^2 n^2 - \beta^2} = \sqrt{k_0^2 \varepsilon - \beta^2}$ is determination value of propagating (k>0) and evanescent (k<0) wave in lossless media.

Now, the electric fields can be separately calculated and described as

$$E_y(x) = \begin{cases} A_1 e^{-i\beta z} e^{k_{cladding} x} & x > 0 \\ A_2 e^{-i\beta z} e^{i k_{core} x} & x < 0 \end{cases} \tag{29}$$

$$H_z(x) = \begin{cases} -iA_1 \dfrac{1}{\omega\mu_0} k_{cladding} e^{-i\beta z} e^{k_{cladding} x} & x > 0 \\ -iA_2 \dfrac{1}{\omega\mu_0} k_{core} e^{-i\beta z} e^{k_{core} x} & x < 0 \end{cases} \tag{30}$$

$$H_x(x) = \begin{cases} A_1 \dfrac{\beta}{\omega\mu_0} k_{cladding} e^{-i\beta z} e^{k_{cladding} x} & x > 0 \\ A_2 \dfrac{\beta}{\omega\mu_0} k_{core} e^{-i\beta z} e^{k_{core} x} & x < 0 \end{cases} \tag{31}$$

Depending on the propagation constant and the refractive index of $n_j$, the electromagnetic fields in the j region can be calculated.

**TM-modes**

For TM modes, $H_y = H_z = 0$ and $H_y = 0$. Thus, the wave equations can be simplified after combining adequately

$$\frac{\partial^2 H_y(x)}{\partial x^2} + \frac{1}{n^2}\frac{dn^2}{d^2x}\frac{dH_y(x)}{dx} + [k_0^2 n^2(x) - \beta^2]H_y(x) = 0 \tag{32}$$

For a constant refractive index, the second derivative equations on the left side will be 0 and can be similar form as (1)

$$\frac{\partial^2 H_y(x)}{\partial x^2} + [k_0^2 n^2(x) - \beta^2]H_y(x) = 0 \tag{33}$$

Now, the electromagnetic fields can be separately calculated and described as

$$H_y(x) = \begin{cases} A_1 e^{-i\beta z} e^{k_{cladding} x} & x > 0 \\ A_2 e^{-i\beta z} e^{ik_{core} x} & x < 0 \end{cases} \tag{34}$$

$$E_z(x) = \begin{cases} -iA_1 \dfrac{1}{\omega \varepsilon_g} k_{cladding} e^{-i\beta z} e^{k_{cladding} x} & x > 0 \\ -iA_2 \dfrac{1}{\omega \varepsilon_g} k_{core} e^{-i\beta z} e^{k_{core} x} & x < 0 \end{cases} \tag{35}$$

$$E_x(x) = \begin{cases} -A_1 \dfrac{\beta}{\omega \varepsilon_g} k_{cladding} e^{-i\beta z} e^{k_{cladding} x} & x > 0 \\ -A_2 \dfrac{\beta}{\omega \varepsilon_g} k_{core} e^{-i\beta z} e^{k_{core} x} & x < 0 \end{cases} \tag{36}$$

For TE and TM modes in a dielectric waveguide, exponential decaying wave can be expected in the cladding due to k<0 while propagating one can be expected in the core.

### *1.1.2.2.* Metallic waveguide

In a metallic waveguide, conduction electrons in the metal interact with the incident light strongly and therefore results in polaritons on the surface of metallic ($\varepsilon_m < 0$) and dielectric ($\varepsilon_m > 0$) materials which is called collective oscillation of free electrons. The propagating wave on the surface of the metal is called propagating surface plasmon polaritons (PSPP) propagates and the electromagnetic fields are strongly confined on the surface of the metal while the one is confined in core and propagates as total internal reflection in dielectric waveguides. To have a propagating wave in the waveguide, $\mathrm{Re}[\varepsilon_m] < 0 \; and \; |\varepsilon_m| > |\varepsilon_d|$and the $\omega < \omega_p$ must be satisfied. The wave equations and analogous sets derived for dielectric waveguide can be still valid except that the generalized dielectric permittivity $\varepsilon_g = \varepsilon - i\sigma/\omega$ is not any more real but complex value ($\sigma \neq 0$).

**TE modes**

From the equation set (29, 31), the condition for the continuity of $E_y$ and $H_x$ must be fulfilled and result in $A_1$ =$A_2$=0. Thus, TE polarization cannot be supported in the metallic waveguide.

**TM modes**

From the equation set (34, 35), with continuity of $H_y$ and $D_{x,z} = \varepsilon_j E_{x,z}$, $A_1$ =$A_2$ must be required on the interface and the following relations can be obtained

$$\frac{k_{dielectric}}{k_{metal}} = -\frac{\varepsilon_{dielectric}}{\varepsilon_{metal}} \tag{37}$$

To fulfill the above relations, the dielectric constants of metal must be negative since $\varepsilon_{dielectric}$ is positive. Now, $k_{metal} = \sqrt{k_0^2\varepsilon - \beta^2}$ is positive, so that also the fields components for TM modes in both materials are exponential functions. Thus, the fields are confined on the interface between a metal and dielectric medium.

Let us now think about the influence of the imaginary part of a dielectric constant which will results in Ohmic loss due to the damping of electron oscillation in metal. From equation ($k_{metal} = \sqrt{k_0^2\varepsilon - \beta^2}$), k is not only real but complex. The wavevector k can be separated into real and imaginary parts and expressed as $k_c = \mathrm{k} - \mathrm{ia}$.

The electric field propagating along metal for a plane monochromatic wave will be defined by

$$E(z) = Re\left[E_0 e^{i(\omega t - k_c r)}\right] = Re[\, E_0 e^{-\mathrm{ar}} e^{i(\omega t - kr)}\,] \qquad (38$$

An indicating value to determine its intensity attenuation for absorbing media such as metal and its feasibility for the waveguide applications is propagation length can be expressed in the following way:

$$L_z = \frac{1}{2\mathrm{a}} \qquad (39)$$

The wavevector of SPPs at the interface between dielectric and metallic materials can be derived by equation (21) with combining $\mathrm{k} = \sqrt{k_0^2\varepsilon - \beta^2}$, which is given,

$$\beta = k_0 \sqrt{\frac{\varepsilon_m \varepsilon_d}{\varepsilon_m + \varepsilon_d}} \tag{40}$$

Generally, the permittivity of dielectric material ($\varepsilon_d$) does not vary considerably in the visible or near NIR range. On the other hand, the permittivity of the metal ($\varepsilon_m$) is dependent on the frequency. Dispersion relation can be now obtained by substituting the permittivity in the equation (24) and, the wave vector corresponding to frequencies is shown in Figure 1.1.1a.

Now, we shall compare the field distribution in a metallic waveguide with dielectric one. There are two significant differences in the wave equations between the different materials. First, the wave equation in the dielectric waveguide is sinusoidal function while one is an exponential function in the metallic waveguide. This difference results from the sign of real part of relative permittivity. Consequently, electromagnetic fields are confined in the vicinity of the interface as evanescence wave and circumvent the diffraction limit. As can be seen in Figure 1.1a, SPPs has a higher wavevector (shorter wavelength) than vacuum light which is another way to understand the evanescence wave of SPPs.

Second, the wave equation in the metallic waveguide has exponential damping term in propagating direction which is contributed by the imaginary part of relative permittivity while dielectric waveguide has no imaginary part. Consequently, there is energy loss as light propagates in the metallic waveguide which increases with more extensive field confinement. The field distributions in nanowire waveguide in dielectric and metallic

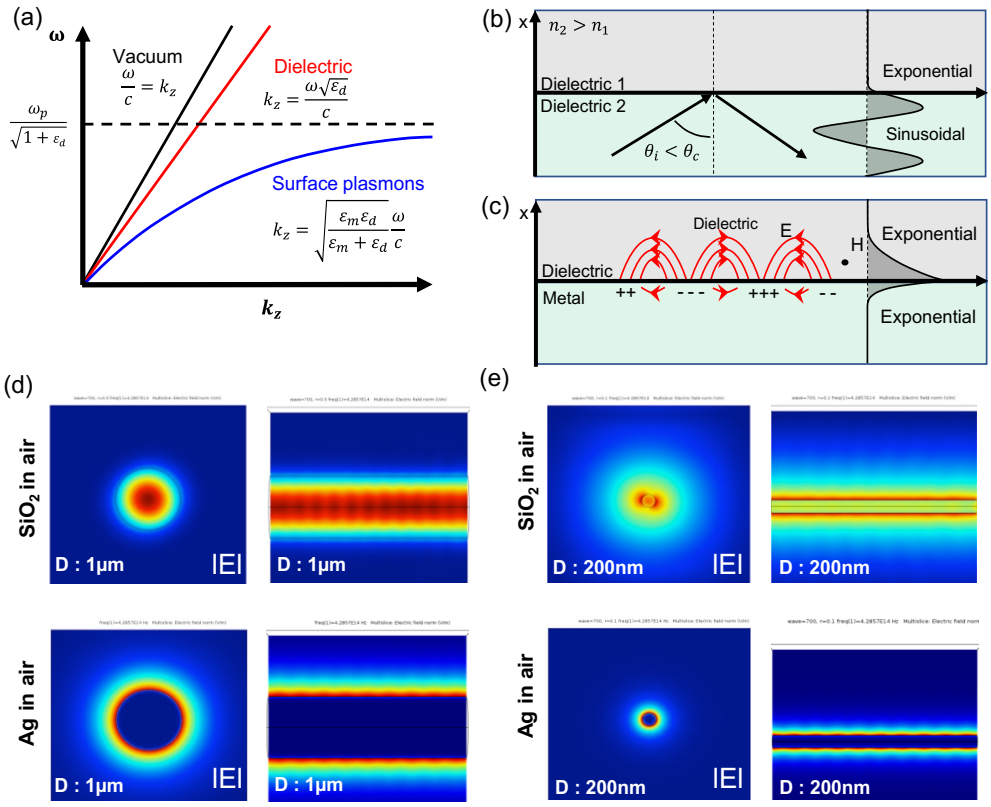


**Figure 1.1.** Comparison of light propagation in dielectric and metallic waveguide. (a) The dispersion relation of SSPs (b) Total internal reflection of wave in dielectric waveguide (c) light propagation as SPPs at the interface between metalic and dielectric materials. Electric-field distribution in $SiO_2$ and Ag NW waveguide with 1um diameter (d) and 200nm diameter(e). The wavelength of the incident light is 700nm.

materials were visually compared in Figure 1.1. Figure 1.1(b, c) shows the mechanism of light propagation and field distribution at the interface. Numerical simulation results are shown in Figure 1.1d that electric fields are confined in a $SiO_2$ waveguide with 1μm diameter. However, the divergence of light with a large evanescence fields due to diffraction limit can be observed with the same $SiO_2$ nanowire but with different diameter (200nm). Both AgNWs with 1μm and 200nm diameter that electric fields are localized at the boundary between dielectric and metal demonstrate diffraction-free guidance of light.

## 1.2. NW synthesis methods

### 1.2.1. Top-down

A top-down approach is a nanofabrication method that produces nanostructure materials from bulk ones, usually silicon wafer or other types of semiconductors, by etching. Nanopatterning is required to leave the aimed structures and etch rest of the parts which can be realized by lithography. The lithography mainly consists of four categories: Optical lithography, E-beam lithography, soft lithography, and nanoimprint lithography. Optical lithography is the most conventional and economic methods for the fabrication of nanostructure materials since it was first introduced in 1960's[14]. The maximum resolution of the nanopatterns is limited by diffraction and the minimum distance (d) of the pattern is given by Rayleigh criterion, $d=0.61\cdot\lambda/NA$, where $\lambda$ is the wavelength of light and NA is a numerical aperture of the objective lens. Therefore, the lithography resolution limit is around 240nm with 400nm (near UV region) and NA=1(upper limit). Using immersion media such as water and a shorter wavelength (193nm) which is adapted for commercial use, 38nm resolution could have been obtained with optical lithography[15]. However, complex multi-patterning processes and expensive equipment are prerequisites for the high resolution. E-beam lithography uses electron beam which has much smaller wavelengths. Theoretically, the resolution is unlimited but practically limited by an objective lens system which will be ~0.1nm[16]. Therefore, synthesis of NWs with a desired size and structure is available. Nevertheless, its high price and relatively slow speed hinder the prevalence of the system for the NW synthesis. Soft lithography and nano-imprint are non-photolithographic methods and they are simple and low-cost. In addition, high productivity

with a large area is the most attractive advantage of the non-photolithographic methods. Soft lithography uses elastomeric stamps to create patterns on a substrate by printing or molding or embossing while nanoimprinting method uses hard mask to mechanically press plastic resists that later can be solidified thermally or by UV exposure. The resolution of the non-lithography methods is mainly determined by the change in shape of the soft materials and its interface properties with mold [17]. All the methods introduced above have a great advantage of the creation of multiple NWs at desired locations for the integrated optoelectronics. However, rough sidewall roughness is always a stumbling block resulting in a high propagation loss.

### 1.2.2. *Bottom-up*

The bottom-up approach is the method to build nanoscale architectures from atomic or molecular components. NWs synthesized with the atom or molecule building blocks exhibit an excellent single crystallinity which results in a low propagation loss due to the atomically smooth surface and high diameter uniformity. Top-down approach has a much higher NW growth rate compared to bottom-up approaches. On the other hand, the bottom-up approach synthesizes myriad NWs simultaneously. Therefore, bottom-up approach has advantages of sample quality and efficiency over top-down approach. Also, different optical properties can be obtained with a single NW by tuning composition, structure, and lattice during growth procedures. Diverse methods for the synthesis of NWs based on bottom-up approach have been demonstrated: CVD, CVT, molecular beam epitaxy, vapor-

solid-solid, vapor-solid, oxide-assisted growth, templated growth, solution-liquid-solid growth, supercritical fluid liquid solid growth, solvothermal/hydrothermal synthesis, directed solution phase growth and etc[18]. In this chapter, the most common synthesis routes will be discussed mainly since the other techniques have been approved only for the synthesis of a specific semiconductor and have many issues to be addressed to be adopted as a general synthesis route for 1-D nanostructure fabrication.

#### *1.2.2.1. Gas phase synthesis technique*

The vapor-liquid-solid method is 1-D structure growth technique by adsorbing gas phase reagents on to a catalytic liquid alloy which finally starts to be crystallized from the interface between liquid alloy and solid due to supersaturation. The optimum catalyst for a liquid eutectic alloy for the 1-D structure of interest can be chosen on the basis of the phase diagram. Si has been typically synthesized and this approach has been applied for the synthesis of the other semiconductor NWs such as Si[19] and Ge[20], group III–V (GaAs, GaP, InAs, InP, GaAsP, InAsP), II-VI (ZnS, ZnSe, CdS, CdSe), and IV-VI (PbTe)[18, 21]. The diameter of the 1D nanomaterial is determined by the catalyst droplet size at the tip of the NW. However, a decrease of the droplet size for the synthesis of 1D structures in nanoscale is not easily achieved due to a significantly large chemical potential difference of the component species in the liquid droplet and Ostwald ripening. Also, it suffers from the diffusion of the metal catalyst into the NW resulting in recombination of a charge carrier or scattering center[18, 22]. Other synthesis techniques without catalyst have been studied

intensively such as vapor-solid growth, oxide-assisted growth, and templated growth although they are not as popularly used as VLS are.

#### *1.2.2.2. Solution phase synthesis technique*

While synthesis of NWs with VLS is conducted in the vapor phase with the assistance of a catalyst alloy, the Solution-Liquid-Solid (SLS) approaches synthesize NWs in solution with a surfactant that allows the growth of the nanomaterials only in one direction. Growth temperatures are usually low(<350°C) compared to VLS and NWs with a diameter even smaller than 10nm with a better distribution can be achieved due to easier size control of the metal catalyst particle using surfactants in solution. However, the metal must exist not only as a liquid form but also as an alloy with the semiconductor of interest. Therefore, it has limited choices of the available metal catalyst due to the low synthesis temperature. Even with such limitation, various semi-conductor NWs such as IV(Si, Ge)[23-24], II-VI(Cds, CdTe, ZnS, ZnSe, ZnTe)[25-29], and III_V(InP, InAs, GaAs)[30].

Solvothermal/hydrothermal method has been considered as the most attractive synthesis route in the past decades since it has many avenues to control the diameter of NWs such as solution pH, reaction temperature, reaction time, solute concentration, additives, and solvents. Compared to gas phase synthesis routes, this approach offers several advantages such as lower energy consumption, simplicity, high growth speed, environmentally friendly and so on. Moreover, this approach does not suffer from difficulties to choose low melting temperature catalyst in SLS method. Highly ordered semi-conductor NW arrays

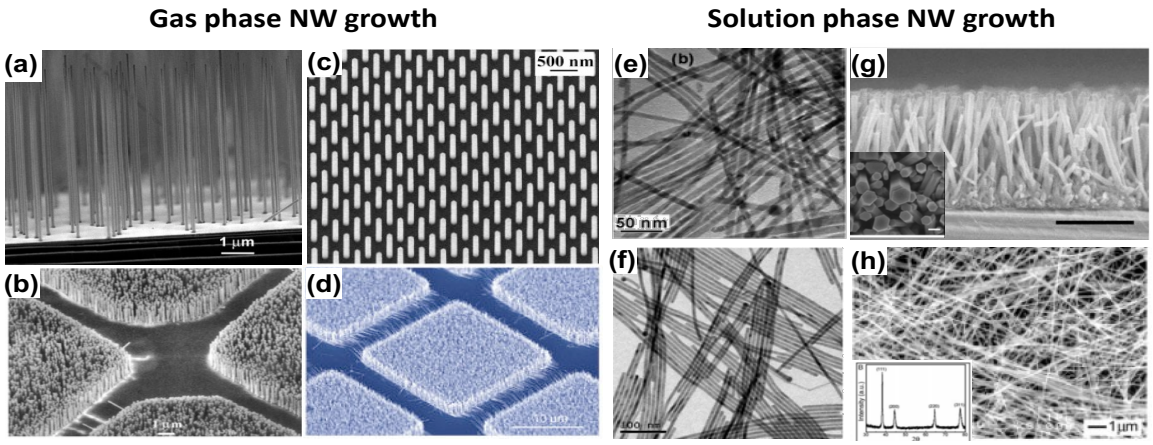


**Figure 1.2.** SEM and images of NWs grown with different methods (a) SEM image of silicon NW arrays grown with VLS. (b) SEM image of ZnO NW arrays grown with VLS. (c) SEM image of periodically aligned InP NW arrays grown with MOCVD. (d) SEM image of GaN NW arrays grown with VLS. (e) TEM images of InAs NWs with SLS. (f) TEM images of CdTe NWs grown with SLS. (g) Cross-sectional SEM image of ZnO NW arrays grown with hydrothermal method. The inset shows the TEM image and XRD pattern of the NWs. (h) SEM image of AgNWs grown with polyol process. The inset shows the TEM image and XRD pattern of the NWs. Reproduced with permission: a[22], b[23], c[24], d[25], e-f[20], g[26], h[27].

grown epitaxially from the substrate have stranded out as a promising material for the application not only for optoelectronics but also for sensors, catalysts and solar cells due to their large surface areas with a high density.

Capping agents enables the change of the free energies of crystallographic surfaces and thus change the growth rate of the nanostructures on certain facets leading to a synthesis of 1D nanostructures. In the last decades, synthesis of metallic NWs in a solution at a low temperature has been intensively studied and demonstrated. This synthesis method requires four main functional chemicals: Metal ions, reducing agents, complexing agents, and capping agents. Ag, Cu, And Au are the common metal NWs that extensively studied and synthesized due to their high conductivity for the path of electrical current. On the other

hand, Ag has been considered the most favorable materials for optical waveguide due to its high real and low imaginary parts of dielectric constants. Bulk and uniform silver NWs have been synthesized using polyol methods by Y. Sun et al. in 2002 and this method are commonly adopted for the commercial production of silver NWs this day. In this synthesis, Ag ions were supplied by $AgNO_3$ and ethylene glycol was used not only as a reducing agent but also growth solvent. PVP is used as a capping agent, and Ag ion is complexed with Cl resulting in a slow chemical reaction[36].

### 1.3. Dielectric NW

The dielectric material is a typical material for 1D NW waveguide due to the low propagation loss and high thermal and chemical stability. The basic concept of light propagation in a dielectric medium is a total internal reflection. Light is confined and propagates in a high refractive index media (core) surrounded by median (cladding) with a lower refractive index. To confine light with a wavelength larger than the radius of NW waveguide, the larger contrast between core and cladding is necessary. Air is typically chosen and preferential as a cladding because it has the lowest refractive index (n=1). Tightly confining the light in NW is essential not only for passive wave guidance but also for active wave guidance such as light emission because the waveguide emission at the end facet is much stronger than the lateral facet (Cavity should be formed in the direction of the NW) which will finally improve optical feedback[18]. Although silica is the most mature and commercially available among all of the materials for an optical waveguide, it is less

popularly used for the guidance of subwavelength due to its low refractive index contrast. Many semiconductors, on the other hand, has a high refractive index and generally show dielectric optical properties at the frequency below their band gap; no significant absorption. Also, they can be light emitter or detector when the frequency of light or electrical bias is higher than the bandgap. Semi-conductors that are popularly used in the fields of optics are listed in Table 1.1.

In this section, we will overview NW waveguides with a remarkable performance in various applications. Many papers have been already reported regarding NW waveguides for the optoelectronics. Therefore, remarkable research footprints for optoelectronics and other application fields that have not been reviewed would be discussed primarily.

**Table 1.1.** Homogeneous semiconductor nanowires for optoelectronics (UV-Visible).

| Materials | Refractive index (Visible to NIR) | Band gap | Vapor phase | | Solution phase | | Wavelength ranges for photo emitter or detector |
|---|---|---|---|---|---|---|---|
| | | | Synthesis method | Properties | Synthesis method | Properties | |
| ZnO | 2.1~1.7 | 3.37eV | VLS, VS, PVD, MOCVD | D: a few~300 nm L: ~ A few millimeter | HT/ST, ECD, Sol-gel | D: 10~300nm L: ~10μm | UV, Waveguide |
| GaN | 2.6~2.3 | 3.4eV | VLS, VS, PVD, MOCVD | D: A few~100 nm L: >10μm | N/A | N/A | UV, Waveguide |
| CdS | 2.1~1.7 | 2.42eV | VLS, VS, PVD, MOCVD | D: A few~500nmVLS L: ~100μm | HT/ST, SLS, ECD, | D: 10~100nm L: >10μm | Visible |
| CdSe | 2.7~2.4 | 1.74eV | VLS, PVD | D: A few~30nm L: ~10μm | SLS, ECD | D: A few ~33nm L: >10μm | Visible |
| GaAs | 5.1~3.3 | 1.42eV | VLS, VS, MOCVD | D: A few~200nm L: >10μm | SLS, ECD | D: A few ~40nm L: ~10μm | NIR |
| ZnS | 2.6~2.3 | 3.7eV | VLS, VS, PVD | D: A few~60nm L: >10μm | HT/ST, SLS, ECD | D: A few~15nm L: >1μm | UV |
| GaP | 4.2~3.1 | 2.26eV | VLS | D: A few~30nm L: >10μm | SLS | D: 10~30nm L: ~10μm | Visible |
| GaSb | 5.2~3.8 | 0.726eV | VS, MOCVD | D: ~30nm L: >10μm | N/A | N/A | NIR |
| InP | 4.4~3.1 | 1.344eV | VLS | D: A few~30nm L: ~10μm | SLS | D: A few~20nm L: >10μm | NIR |
| CdTe | 3.7~2.6 | 1.5eV | VLS | D: A few~100nm L: ~100μm | SLS, ECD,HT/ST | D: A few~10nm L: >10μm | NIR |
| ZnTe | 2.7~3.7 | 2.26eV | VLS | D: A few~200nm L: >20μm | SLS, ECD, HT/ST | D: 40~60nm L: >45μm | Visible |
| ZnSe | 2.9~2.4 | 2.7eV | VLS, PVD | D: A few~80nm L: ~10μm | SLS,ECD | D: 10~40nm L: >10μm | Visible |
| Si | 5.6~3.4 | 1.1eV | VLS, VS, PVD | D: A few~20nm L: ~30μm | SLS, ECD | D: A few~50nm L: >20μm | Waveguide |
| $TiO_2$ | 3.3~2.7 | 3.2eV | VLS, PVD | D: A few~500nm L: ~10μm | HT/ST, ECD, Sol-gel | D: 10nm~100nm L: >10μm | Waveguide |
| $SnO_2$ | 2.1~2.0 | 3.6eV | VLS, VS | D: 30~500nm L:~A few millimeter | HT/ST | D: A few ~100nm L: ~100μm | Waveguide |

**VLS** : Vapor-Liquid-Solid **VS** : Vapor-Solid **SLS** : Solution-Liquid-Solid **HT/ST** : Hydrothermal/Solvothermal **ECD** : Electrochemical Deposition **PVD** : Physical Vapor Deposition **MOCVD** : Metallic-organic Chemical Vapor Deposition.

### 1.3.1. *Optoelectronics*

Photon has already replaced copper for the long-distance communication with advantages of broad bandwidth, light, and cost-effective. However, there still many obstacles to exploiting photon for electronic circuits such as processors and memory chips. The primary application of the optical NW waveguide in the field of optoelectronics is the replacement of electrons with photons for the chip to chip or intra chip communications which requires a narrow footprint for the increase of the transmitted communication density. The transfer of information with the electron is currently limited by its frequency (<100MHz) which is proportional to the impedance of the conductor while photon has a much higher frequency ranges from 150-800THz for visible and near-infrared spectrum[37].

The requirements of the NW waveguides for the optoelectronics are followings: stability, low attenuation, low cost, broader bandwidth, small footprint, low heat generation, lower skew and easy Fabry–Perot cavity of NW, and immunity of the signal path to electromagnetic interference[38]. Semiconductor NW (III-V, II-VI, or IV-VI) generally satisfies the requirements except for the limitation of downsizing footprint further due to the diffraction limit and bending loss. Downsizing the footprint results in lower power consumption, dense interconnects, less sensitive to the propagation loss, easier control of temperature, and low fabrication cost.

NW waveguides for optoelectronics are mainly classified into three components: light emitter (active waveguide), passive waveguide, and photodetector.

### 1.3.2. *Light emitter*

The NW that emit light is called active or functional waveguide. Electrically driven lasing from NW is attractive due to the smaller foot print and low energy consumption compared to optically pumped lasing. The electrically driven lasing is called light emitting diode (LED), and it emits light with a certain wavelength through the recombination of the electrons excited by electrical energy. The wavelength of the light is determined by the direct band gap between p and n-type NW. In the early stage, the NW LED was realized by a combination of the top-down grown p-type planar substrate with n-type NW. Large variation of turn-on voltage was inevitable due to poor hole mobility of the planar substrate contributed by the low crystallinity. Afterward, the NW LED was realized by crossing single crystal p and n-type NWs with high electron and hole mobility. Interestingly, the electroluminescence excited at the cross junction can be coupled in and guided through the n-type waveguide with a forward bias. However, the asymmetric point at the junction between the two NW still can act as a scattering spot leading to the inefficient optical cavity and therefore poor spectral resolution. Later, electrically driven single photon source with a good polarization has been firstly demonstrated with an axial hetero-structure NW using GaAs/GaP and n-InP/p-InP[39]. The emission efficiency could have been improved by radial hetero-structure NWs due to a larger area for carrier injection or collection. The introduction of multi-quantum well in the NW with a tunable band gap enables an efficient radiative recombination and control of wavelength spectrum[40]. The radial hetero-structure NWs demonstrated not only a better emission efficiency but also directional radiation along the LED NW which is significantly important in order to couple the light to the passive

waveguide[40-42]. However, none of the group has measured the emission efficiency in that point of view. We believe that this work should be accomplished for practical integration of LED NW in the future.

Diverse semi-conducting materials have been used to generate visible or NIR light emission. Visible light generation (1.8~3.1eV) has generally been realized using

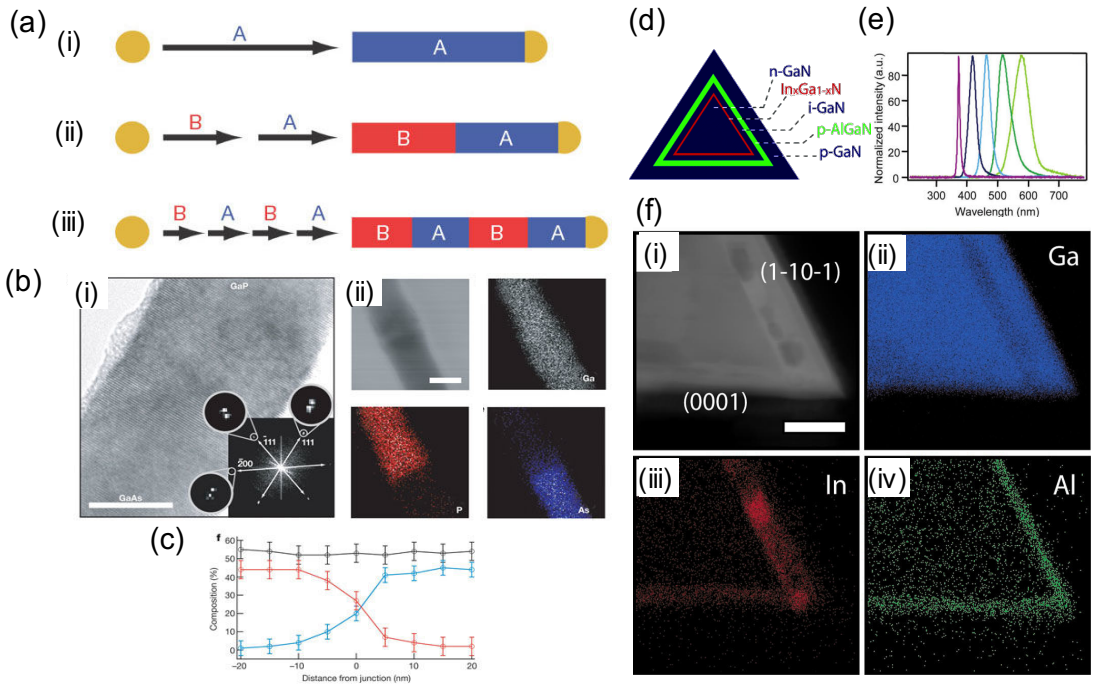


**Figure 1.3.** Heterostructure nanowire photodiode. (a) Schematic illustration of nanowire superlattices synthesis. (i), Au catalyst nucleate (yellow) and one-dimensional semiconductor nanowire (blue) growth. (ii), A different material (red) is grown from the end of the nanowire after completion of the first growth step. (iii) Compositional superlattices within a single nanowire can be synthesized with a repetition of steps (i) and (ii). (b)TEM images of a GaAs/GaP junction (i) and elemental mapping (ii) of Ga(white), P(red), As(blue) in the vicinity of the junction. (c) Line compositional profile across the junction region. (d) Cross-sectional view of a core/multishell(CMS) nanowire structure. (e) Normalized electroluminescence spectra measured from multicolor CMS nanowire LEDs. (f) Dark-field STEM image of GaN/$In_xGa_{1-x}N$/GaN/AlGaN CMS nanowire (i) and elemental mapping of Ga (blue, ii), In (red, iii), and Al (green, iv) respectively. Reproduced with permission: a-c[28], d-

CdS(2.42eV) due to its unique bandgap[43], and its wavelength could have been tuned by compositional variation with CdSe (1.74eV)[44-45] and ZnS(3.7eV)[46]. Generally, the propagation loss is inversely proportional to the increase of the wavelength. Therefore, NIR has a lower propagation loss compared to UV and visible light. However, NIR requires a larger NW diameter for the confinement of the light and Fabry–Perot cavity effects. Otherwise, most of the optical modes exist outside of the NWs and results in a low reflectivity at the end facets. The basic materials used for the lasers were listed in Table 1.1.

Mode excitation with a high effective mode index is desired for the practical application. The excited mode with high index contrast with the environment such as air results in high confinement factor and therefore, a high end-facet reflectivity which consequently enhances optical gain[47-48]. Also, highly resolved frequency mode is necessary to prevent lower data transmission rate and false signaling caused by group-velocity dispersion[49-50]. Typically, nanowire emits single mode light when diameter satisfies $1 \approx {\pi D}/{\lambda}\sqrt{(n_{NW}^2 - n_{air}^2)} < 2.4$, and the ends are cleaved with the NW length that satisfy the Fabry-Perot optical cavity, $L = m\left({\lambda}/{2n_{NW}}\right)$, where D is diameter of NW, $\lambda$ is wavelength of light, $n_{NW}$ and $n_{air}$ are refractive indices of NW and air respectively, L is the length of NW, m is an integer. Because the band structure of semiconuctors relies on temperature, multi frequency modes are easily excited at room temperature unless the lasing cavity becomes much shorter[51]. However, the shortened cavity path result in a lower optical gain and therefore a higher threshold. In 2011, Y Xiao et al. demostrated single mode excitation

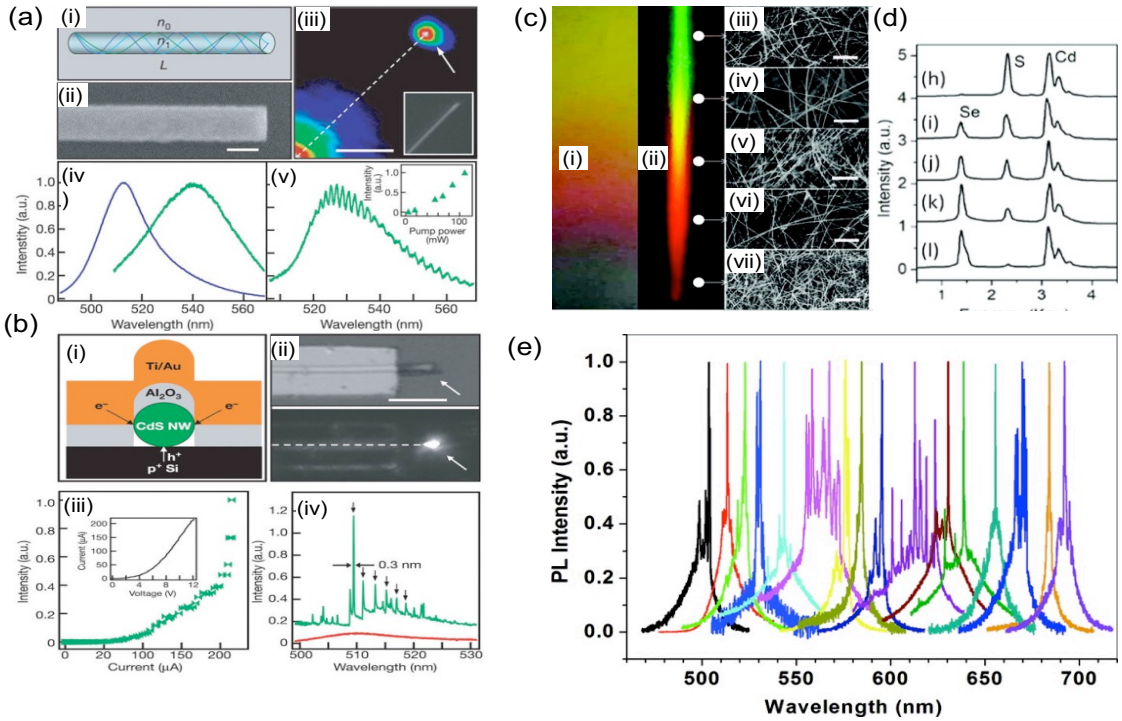


**Figure 1.4.** Optically and electrically pumped nanowire laser (a) Schematic illustration (i) and SEM image (ii) of cleaved CdS nanowire optically pumped laser. (iii) Photoluminescence image of a CdS nanowire excited (low-left corner) about 15 μm away from the nanowire end at room temperature. Inset shows an optical image of the nanowire under white-light illumination. (iv) Comparison of photoluminesence spectra obtained from body (blue) and end (green) of the nanowire at a low pump power (10mW). (v) Photoluminescence spectrum obtained from the nanowire end at higher pump power (80 mW). (b) Schematic illustration (i) and optical images (ii) of the electrically driven CdS nanowire laser at room temperature with an injection current of about 80 μA. (iii) Emission intensity as function of injection current. (iv) Electroluminescence spectra from the nanowire end obtained with injection currents of 120 μA (red) and 210 μA (green). Fabry–Perot cavity modes (black arrows) are clearly shown with an average spacing of 1.83 nm. (c) Real color image of spatially composition-graded CdSSe NWs on a quartz substrate under room lightning (i) and UV-laser illumination (ii). SEM images of CdSSe NWs taken at the white spots in (ii-vii) respectively. (d) In-situ EDS corresponding to the five SEM images of (ii-vii). (e) Photoluminescence spectra obtained at different locations along the CdSSe grown quartz substrate at 77 K showing multimode lasing. Reproduced with permission: a-b[41], c-e[34].

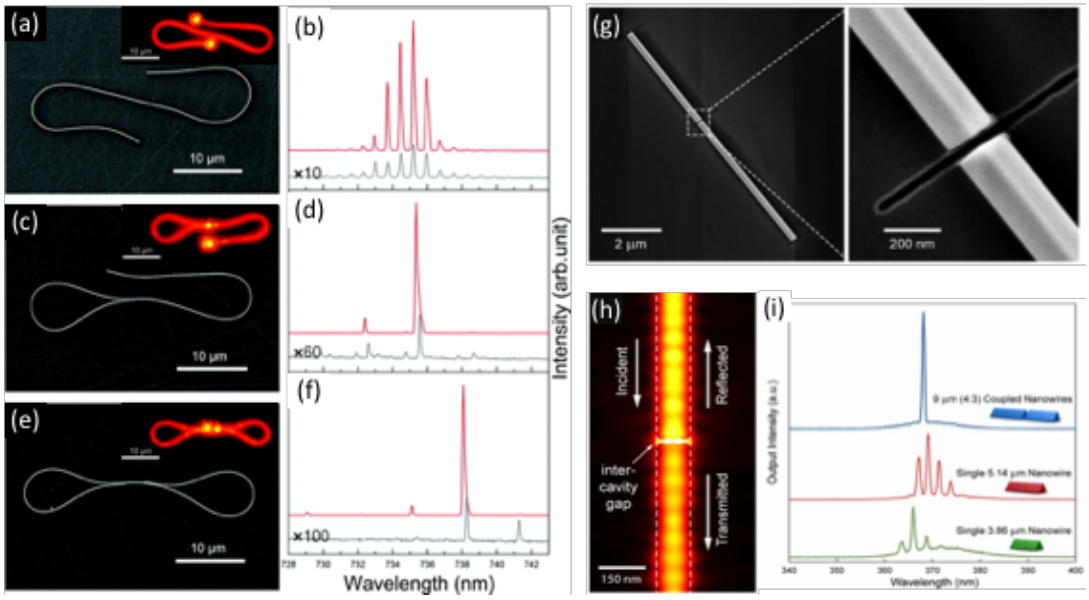


**Figure 1.5.** Mode selection of laser from single nanowire by nanowire structure change. (a-f) Single frequency laser from folded single CdSe nanowire. The folded one or two NW ends create loop mirrors(LMs) and coupled resonant cavities. Scanning electron microscope(SEM) images and lasing spectra of single NW without LM (a and b) and with one LM(c and d), and double LMs(e and f). The insets in the SEM images (a, c, and e) are PL microscope images. The two spectra with different colors (red and black) were measured with pump fluence far above the threshold and near the threshold respectively. B (g-i) Single frequency laser from cleaved-coupled nanowire. (g) SEM images of cleaved GaN nanowires with ~40nm intercavity gap distance. (h) Simulated electric fields in the NWs near the 20nm gap width. (i) Photoluminescence spectra of lasing from individual NW cavity (red and green) and the coupled NW cavity (blue). Single frequency mode was observed with axially coupled NW cavity, while multiple frequency modes were observed with the individual NW cavities. Reproduced with permission: a-f[39] , g-i[43].

from nanowire by manually folding nanowire with fiber probe to form loop mirrors. Higher reflectibility of the loop mirror enables the excitation of the laser with a low threshold. However, manipulation of individual nanowire using fiber probe cannot achive the repeatable and reliable results with the same folding conditions. In 2013, H Gao et al. proposed a cleaved coupled nanowire laser realized by cutting GaN nanowire using

focused ion beam milling. Compared to individual nanowires, the cleaved coupled nanowire with nm gap widths, summation of the both NW lengths provide gain of the laser while the gap distance narrow the optical band. This fabrication method increases the reproducibility significantly compared to the previously proposed methods for single mode selection with a lower threshold[50].

### 1.3.3. *Passive waveguide*

The data transmitted rate for the short distance communication such as the integrated circuits on a board or intra-chip interconnects is also significantly limited by the bandwidth of the passive waveguide because relatively long-distance travel of the light occurs mainly in the passive waveguide. For the passive waveguide, maintenance of the mode with a low propagation loss needs to be considered overbearingly. Surface roughness, high refractive index contrast, and randomly distributed scattering centers (impurity atoms, lattice defects, etc.) are main reasons for the propagation losses in dielectric NW whereas absorption near the band edge is also a considerable source of the loss in semiconductor[53]. Those problems are from material properties which should be addressed and solved in the growth process. Besides the loss from intrinsic material properties, the main loss which occurs during the integration of the NWs into the optical circuits is bend loss. Compact packaging of the waveguides on a small footprint can result in a considerable bend loss. There have been numerous reports that measured and numerically calculated the bending loss of optical waveguide with a high refractive index contrast and sub-diffraction waveguide diameter.

However, the bending losses are dependent on the refractive index difference, waveguide diameter, and wavelength of light which finally determines the number and weight of modes in the waveguide. The only single mode can be excited when the waveguide barely supports the light with a significant fraction of evanescence fields due to either long wavelength or small waveguide diameter. Then, the waveguide packaging for intra-chip communication must carefully be designed because the mode fields in the waveguide will be lost easily by a slight bend. Therefore, the tradeoff between single mode and bending loss should be considered before designing the waveguide. There are various waveguides suitable for a passive waveguide of optoelectronic technology. Silica or silicon NW has great merit over the other materials that it can be integrated on a silicon/silicon substrate via deposition or etching with a lithography technology. The increase of the refractive index silica (1.45) could have been achieved by introducing impurities with high index materials such as SiN. The major concern with the silica or silicon waveguide through the lithography technology was its roughness of the top and sidewalls (~1 dB/cm). Scattering loss due to rough surface or defects can be negligible for the NW waveguide grown using CVD at a high temperature.

### 1.3.4. *Photodetector*

The basic concept of the photodetector is just the inverse of the laser; excited electrons by photons of light are used to create a current. This concept is also same as that of solar cells or sensors. It is well known that NW has larger absorption characteristics than bulk

materials due to a larger physical cross-sectional area and photocarieer collection efficacy[55-58]. III-V compounds are dominantly considered as ideal materials and used due to their high sensitivity and high quantum efficiencies such as InP, GaAs, InAs, InSb, InAsP, InGaAs, and GaAsSb[59]. High responsivity and spatial resolution are required for the commercialization of photodetectors. To achieve a high responsivity, an increase of quantum efficiency by reducing carrier transit time is necessary. Core-shell heterostructure NW photodetector shows that lateral collection of carriers can reduce detrimental carrier recombination. The sensitivity of the detector critically influenced by thermally generated carriers which can be described by temperature-dependent Fermi-Dirac statistics. Therefore, photodetection with a high spectral resolution at room temperatures is required for a lower cost production, smaller size, and lower power consumption. Detection of a broad spectrum ranging from 632nm to $1.5\mu m$ at room temperature has been reported firstly by J. Miao et al. using InAs NW[60]. Other III–V semiconductor NWs operated at room temperature such as GaAsSb and hetro-junction GaSb/GaInSb NWs have been reported for NIR phtodetection[59-62].

In an ideal case, it is favorable to integrate the three waveguide components into an NW or at least by parallel or axial alignments of the waveguides for evanescence mode coupling. This configuration does not require free space light coupling leading to a significant decrease of coupling efficiency and an increase of fabrication cost, size, weight, and complexity of fabrication process, and the possibility to be misaligned due to an external impact. M. Tchemycheva et al. made an effort to integrate the emission and detection of the light using NW waveguide[42]. In their work, core/shell InGaN/GaN with five radial

quantum wells were exploited for emitter and detector to reduce carrier transit time and circumvent the non-radiative recombination on the surface defects[63-65]. The two emitter and detector were connected by SiN waveguide fabricated by nanolithography. However, the on-off transient is extraordinarily slow (<0.5s) even with core/shell heterostructure. Either inefficient injection of a charge carrier or optical coupling among the waveguides might have attributed the slow switching time. Further improvement of on-off transition time is enforced to take full advantage of optical waveguides over copper-based electrical circuit.

### 1.3.5. *Optical sensor*

For the optoelectronics, tightly confinement of the mode in NW waveguide was imperative. For the optical sensor, on the other hand, the vulnerability of the optical modes in the NW to the change of the environment determines the sensitivity of the sensor. Therefore, a larger fraction of evanescence fields outside of the NW is preferred. The optical sensor offers a variety of advantages over the conventional electrical sensor regarding sensitivity, response time, immunity to electromagnetic interference, and multiple routes for the detection of the change of the surrounding materials. The optical fiber is the most popular material used as dielectric waveguide optical sensing because fabrication method is simple and well-developed. The NW can be made by adiabatically stretching an optical fiber, and this method can provide NWs with a uniform diameter and smooth surface. Also, this fabrication method can offer a light coupling without loss because both ends are connected

with adiabatically tapered optical fibers which can be coupled to photodetector and laser easily[66].

In the early stage, sensing the materials surrounding NW has been demonstrated by measuring the change of output intensity. The mechanism is straightforward, and it requires only a photodiode. Later, a variation of phase, polarization, wavelength or transit time of light in the NW waveguide to obtain more information about the surrounding materials have been used. However, they are susceptible to other influences such as stress induced by the NW and temperature variation during measurement. Above all, extreme difficulty to sense or identify specific molecules in a complex medium makes it difficult to be commonly adopted in labs or industry. Later, markers such as dye or quantum dots (QDs) sensitive to a specific molecule with a considerable variation of absorbance or wavelength started to be used for sensing a target molecule regardless of the complexity of the media[67].

In 2012, Yan et al. reported NW based single cell endoscopy which can imaging in living cells without cell membrane damage or significant perturbation of normal cellular process, facilitating the small cross-section of NW waveguide[68]. The NW endoscope was prepared by integrating $SnO_2$ NW with a tapered optical fiber. Efficient light coupling from the optical fiber to the NW was achieved. With this NW endoscope, spot cargo delivery with high spatiotemporal resolution via photon energy was demonstrated. Since then, several NW waveguides have been introduced for specific chemical detection in a living cell[69]. In 2016, J. Lee et al. quantitatively measured $Cu^{2+}$ ions specifically in single living cells using QD embedded polymer NW[70]. A unique property of the endoscopy probe was that the

photoluminescence signal was collected through the same light path used for excitation light. This signal collection configuration can make the device simple since complex optical components to focus or collect light with careful optical alignment are not required.

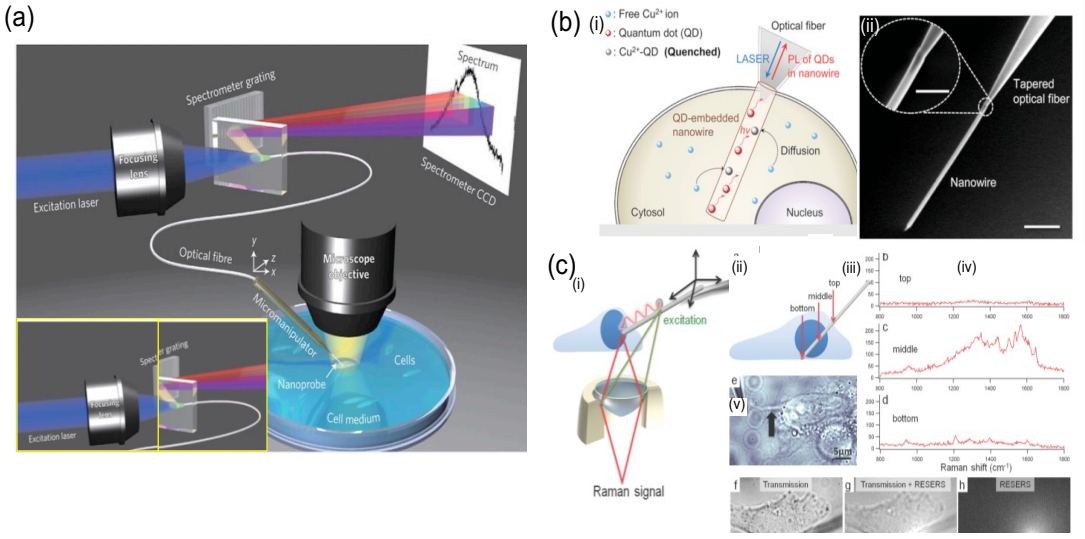


**Figure 1.6.** NW-based single-cell endoscopy probe. (a) Schematic illustration of NW-based optical probe for single cell endoscopy. The inset shows schematic illustration and optical image of coupling light from an optical fiber to a $SnO_2$ NW (c) Schematic illustration (i) and SEM images (ii) of NW endoscopy probe for quantitative sensing of Cu2+ ions in a living cell. (c) Schematic illustration of remotely excited plasmonic NW SERS probe using silver nanoparticle-attached silver NW. Image of optical transmission (ii), remote excitation of SERS under optical transmission (iii), and remote excitation of SERS only in a single living HeLa cell (iv). (v) Remotely excited SERS spectrum from nucleus of the living cell. Reproduced with permission: a[57], b[59], c[60].

### 1.4. Metallic (Plasmonic) NW

As can be seen in Figure 1.1a, wave vector of SPPs is higher than one in free space. To fulfill the momentum conservation, additional momentum must be added by scattering, grating, or evanescent fields, etc. The scattering occurs readily at the end or defects of NW or by placing nanostructures such as nanoparticle or antenna at the vicinity of the NW to break the local symmetry. Another efficient method to excite SPPs is the guidance of light through a high refractive index that matches the wavevector of the SPPs such as silica prism. Recently, smoothly tapered silica demonstrated excitation of propagation SPPs with a high coupling efficiency with transverse evanescence fields. In this case, taper angle, the distance between the two waveguides and metal thickness corresponding to the refractive index of the silica needs to be optimized carefully.

As mentioned early, light coupling from the active semiconducting waveguide to the passive metallic waveguide or vice versa is required for the simplification of optoelectronics. In such case, the phase-matched evanescent coupling between two parallel aligned NWs is the appropriate method. To achieve a high coupling efficiency using laterally aligned NWs, precise control of overlapping length is prerequisite which is dependent on wave vector difference, waveguide geometry, the distance between two waveguides, and propagation loss.

A critical huddle of plasmonic waveguide compared to dielectric one is low propagation length mainly due to ohmic loss. Similar to the dielectric waveguide, the number of modes that plasmonic waveguide can support increases as its diameter increases. As mentioned in

waveguide mode section, the propagation length is a function of imaginary part of the wave vector. Therefore, the different mode has a different propagation length. The effective mode indices and propagation lengths of two lowest order modes are shown in Figure 1.7a. Under 658nm wavelength excitation, only $0^{th}$ order mode (m=0, $H_0$) can be supported when NW diameter is smaller than around 200nm. $1^{st}$ order mode (m=1, $H_1$) is less tightly bound to the plasmonic waveguide. Therefore, less electric fields exist in the metal which results in a higher propagation length compared to $H_0$ mode which propagates being tightly bound to the NW.

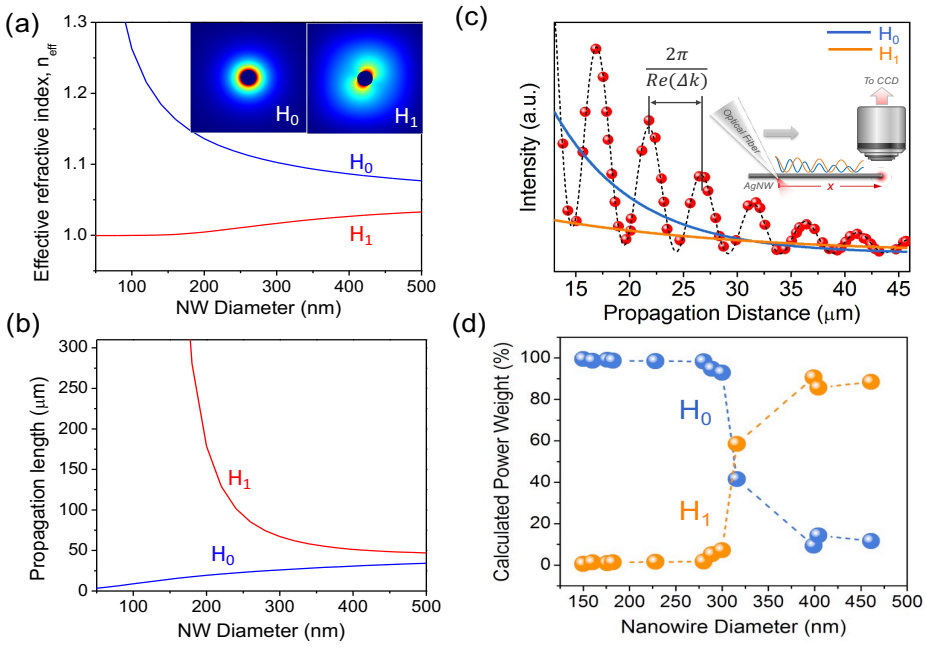


**Figure 1.7.** Two lowest order SPPs modes in AgNW. Numerically calculated effective refractive indices (a) and propagation lengths (b) of two SPP modes in AgNW under 658nm excitation. Insets: Electric field $|E|$ distribution of the two modes in AgNW. (c) Measured emission intensity at the tip of AgNW versus propagation distance. Inset: Schematic illustration of the emission intensity measurement. Attenuation curves of the $H_0$ and $H_1$ modes (Blue and orange lines respectively) are deconvoluted from the experimental data. The wavelength of the incident light is 658nm. (d) Relative weight of two lowest order modes as function of NW diameter under 658nm excitation. Reproduced with permission: c-d[61].

The weight of SPP modes in metal NW relies on NW diameter and polarization. S. Kim et al. successfully decoupled the propagating SPP modes excited with a 658nm wavelength in silver NW and calculated the weight of the modes. The results showed that $H_0$ mode is dominantly excited with an NW diameter lower than 300nm whereas the weight of the $H_1$ increases with beyond 300nm diameter. It is clear that $H_0$ mode can be selectively excited by using a thin NW or a longer wavelength to cut-off higher order mode(Figure 1.7d)[9]. Another method to excite SPP mode selectively is by changing incident polarization. In this method, focused light polarized parallel to the NW excites $H_0$ mode. With the light polarized perpendicular to the NW, $H_1$ is excited dominantly[72]. Selective excitation of the mode in metal NW is critical depending on the application. For example, higher wave vector and localization of strong electromagnetic fields at the tip of NW is preferred for near-field imaging with high spatial resolution. In such case, lowest order mode with the highest momentum needs to be excited dominantly. On the other hand, higher order mode is favorable for in the field of the sensor since it has a longer skin depth. In other words, the electromagnetic fields propagate being less tightly bound to the metal. Therefore, it is more sensitive to change of the surrounding materials. We will go into details of this in each application section.

While dielectric waveguide has a variety of material choices, Ag, Au and Cu are reasonable choices of material based on a propagation loss. The imaginary parts of the metals are lowest in the visible and NIR wavelength range which result in a low propagation length through the relation (39). Among them, Ag has a unique advantage over the others in terms of no absorption in the visible and NIR range. On the other hand, Ag is easily oxidized

even at room temperature. Therefore, Au, chemically more stable material, has also been used often at the expense of slightly increased propagation loss.

As mentioned early, the propagation length varies depending on the weight of SPP modes in a plasmonic waveguide. Therefore, is a considerable deviation between the measured propagation lengths in each report as shown in Table 1.2.

**Table 1.2**. Propagation lengths measured with different techniques.

| Material | Technique | Diameter | Substrate | Wavelength | Propagation length | Ref. |
|---|---|---|---|---|---|---|
| **Ag** | Fabry-Perot resonator modes | 110±15nm | glass | 785nm | 10.1±0.4μm | 1 |
| | Sidewall scattering | ~100nm | glass | 830nm | 3±1μm | 2 |
| | | | sol-gels | 628nm | 9.1μm | 3 |
| | Fluorescence | 50-200nm | glass | 532nm<br>650nm | 6μm<br>11μm | 4 |
| | | 90-170nm | PMMA | 760-860nm | 11-17.5μm | 5 |
| | Tapered fiber | 100nm | air | 532nm | 6.2μm | 6 |
| | | | | 650nm | 11.3μm | |
| | | | | 980nm | 20.2μm | |
| | | 260nm | glass | 532nm<br>633nm<br>980nm | 6.77μm<br>10.56μm<br>13.27μm | 7 |
| | | 750nm | glass | 785nm | 10.6μm | 8 |
| | | 150-461nm | air | 532nm | 150nm : 7.3μm($H_0$), 87.1($H_1$)<br>280nm : 12.7μm($H_0$), 40.5μm($H_1$)<br>458nm : 13.0μm($H_0$), 24.4μm($H_1$) | 9 |
| | | | | 658nm | 150nm : 17.5μm($H_0$), No exist ($H_1$)<br>280nm : 28.2μm($H_0$), 159.1μm($H_1$)<br>461nm : 40.4μm($H_0$), 69.0μm($H_1$) | |
| **Au** | Fluorescence | ~400nm | glass | 532nm | 1.8±0.4μm | 10 |
| | | 60-100nm | PMMA | 760-860nm | 2.4-3.6μm | 5 |
| | | 390 ± 60 nm | glass | 785nm | 3.5μm | 11 |
| | Tapered fiber | 210nm | glass | 980nm<br>785nm<br>650nm | 5.6μm<br>4.9μm<br>3.4μm | 12 |
| | Scanning transient absorption microscopy | 600 ± 220 nm, 380 ± 140 nm | glass | 800nm | 12.3 ± 4.1 μm | 13 |

### 1.4.1. *Optoelectronics*

There have been several studies about plasmonic laser due to its ultra-fast relaxation time and capability of nanoscale confinement of fields. However, all the works under the name of plasmonic NW laser were conducted with semiconductor gain due to the lack of band gap. Therefore, Plasmonic NW generally is used as a passive waveguide. It has unique advantages over dielectric waveguide regarding diffraction-free. Also, electrical communication on the circuits constructed for photonic circuits is available which will increase the function but decrease the size of the device.

In a plasmonic waveguide, a favorable mode for passive waveguide is controversial due to their unique optical properties. $H_0$ mode has an advantage over higher modes because it is less sensitive to the environment, easy to modulate (symmetric radiation at the end), and lower bending radius. On the other hand, $H_1$ has a longer propagation length and higher coupling efficiency with directional mode coupling due to a more extended skin depth. Therefore, selective excitation mode depending on the application of the waveguide is carefully considered.

Bending loss is also inevitable in plasmonic NW waveguide. Wang et al. demonstrated a significant bending loss with a silver NW (Figure 1.8(a-b))[8]. The results showed that the bending radius that the loss starts to increase rapidly is even larger than dielectric waveguide with a high refractive index difference. In the experiment, a long wavelength and thick NW were used which eventually affect the bending loss significantly in the following three ways. A long wavelength of excitation light firstly results in a lower

wavevector (momentum) of SPPs. This wavevector is proportional to the coupling strength between and surface charge oscillation. The higher wavevector, the finer confinement of the modes on the surface of the metal. Since light with long wavelengths were used in the experiment, the SPPs are not tightly bound to the surface of the metal and, as the results, a large fraction of the evanescence fields loses their binding to the metal surface and scatters at the bending part of the waveguide. Secondly, thick NW can support higher order modes whose coupling strength is weaker than lower order mode as can be seen in Figure 1.7a.

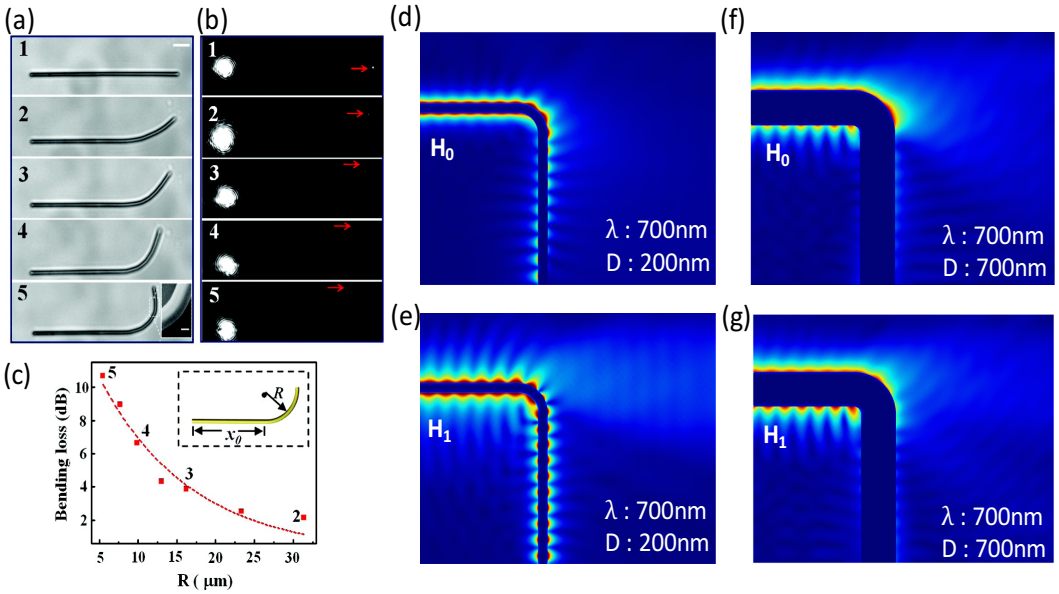


**Figure 1.8.** Dependency of bending loss on bending radius, wavelength of excitation light, and NW diameter. (a) Bright-field optical images of AgNW with different bending radii. The diameter and length of the AgNW is 750nm and 45 μm respectively. The bending radii of the AgNW are 32, 16, 9, and 5μm, respectively. The inset shows SEM image of the curved section. (b) Dark-field optical images with the different bending radii. 758nm laser is focused at the left end of the AgNW and the intensity of emitted light indicated by the red arrows was measured to obtain the bending loss. (c) Calculated bending loss as a function of bending radius after subtracting the propagation loss from the measured values of emitted light intensity in (b). Propagation of $H_0$ (d) and $H_1$ (e) SPPs mode in AgNW with 200nm diameter and 700nm wavelength. Propagation of $H_0$ (f) and $H_1$ (g) SPPs mode in AgNW with 700nm diameter and 700nm wavelength. Reproduced with permission: a-c[70].

Figure 1.8d and e compare the bending loss of two lowest order SPP modes in AgNW waveguide. The lowest order mode ($H_0$) with a high wavevector guided through the AgNW has a lower energy leakage from the bending part than the higher order mode ($H_1$) has. Finally, the coupling strength of even the lowest order mode ($H_0$) decreases as the diameter increase as shown in Figure 1.8f and g. Almost energy leaks from the bending part of the waveguide to free space with a thicker NW diameter. In conclusion, bending loss can be reduced by tightly confining light with surface charge oscillation. However, it finally brings about a large ohmic loss. Balancing of bending loss and Ohmic loss must be considered carefully before designing optical circuits. In addition to them, the weight of each mode should be fully understood which varies depending on excitation methods and condition.

### 1.4.2. *Hybrid plasmonic waveguide*

Besides a short propagation length, plasmonic NW waveguide is the most promising candidate for optoelectronics. For practical application of the plasmonic waveguide to optoelectronics, however, elongating propagation length by reducing the electric field in the metal is prerequisite. This can be realized by inserting insulating layer between a dielectric NW and metal substrate which make most of the electric field confined in the insulator. Oulton et al. have numerically calculated propagation lengths up to the a few hundreds micrometers with high permittivity NW(GaAs)/low permittivity dielectric($SiO_2$)/metal(Ag) structure which is called “hybrid plasmonic waveguide”[73]. The

simulation results showed that strong confinement of electromagnetic energy in the nanometer gap composed of $SiO_2$ and the lossless $SiO_2$ can provide a path for the light propagation leading to a superior propagation length. There is an increasing number of studies to find the optimum structures of hybrid mode via numerical simulations offering a promising balance between field confinement and propagation length. However, most of the studies are limited to just numerical calculations[73-74] and experimentally demonstrated hybrid plasmonic waveguide still suffer from considerable propagation loss to meet the loss required for optoelectronics probably due to the rough surface and poor crystallinity of the top-down grown strip or planar substrates [75-76].

### 1.4.3. *Optical sensor*

Compared with the dielectric waveguide, plasmonic NW has distinct advantages in the field of optical sensing. First, electromagnetic fields are tightly confined at the interface between metal and dielectric environment. Therefore, it has a higher sensitivity to change of environment while dielectric waveguide has the fields inside of it. There have been some efforts to Surface Enhanced Raman Spectroscopy (SERS) a powerful technique that enables the detection of low concentration molecules adsorbed on metal surfaces using amplified electric magnetic fields due to the localized SPPs. With a plasmonic nanogap, SERS has demonstrated a single-molecule detection capability. Also, each molecule has a unique Raman fingerprint so that labeling or even Raman indicators are not necessary. By integrating nanoparticles with plasmonic NW, SERS with high sensitivity is also available.

This is, however, not a unique advantage since this is also available with dielectric waveguide. However, only plasmonic NW waveguide has a still room to reduce the diameter of the waveguide for the applications that smaller cross-section of the waveguide is required such as living cell endoscopy. There have been numerous reports that used plasmonic NW waveguides for SERS. However, all the studies were limited to demonstration of the feasibility of the remote excitation. In 2014, G. Lu et al. measured Raman signals from single living cell plasmonic NW waveguide. This is the first demonstration which applied plasmonic NW waveguide to the practical measurement of biochemical. In this work, the SPP was excited by focusing excitation light in the middle of the NW that a nanoparticle was attached to excite SPP efficiently. Compared to direct excitation of SERS probe by focusing the excitation light at the tip of the NW, remote excitation SERS shows clear Raman spectra of the single living cell due to efficient excitation of SPPs[71].

### 1.4.4. *Near field imaging*

Tip-enhanced Raman spectroscopy (TERS) is a powerful technique that provides compositional information of the samples with a sub-nanometer scale resolution. This technique can be established by irradiating a sharp metal tip with a focused laser beam to create a strong localized SPPs resonances at the tip. A further field enhancement can be achieved when the tip approaches a metal substrate. Conventional TERS tip is created by coating silver on a taper optical fiber or a sharp silicon AFM tip. T. Fujita et al. open a new

avenue in the field of TERS using plasmonic NW waveguide. In this work, silver NW was attached to a sharpened tungsten tip a TERS probe. To guidance of light through the silver NW, gold nanoparticles were integrated into the middle of the NW and used as light coupling point. Compared to direct excitation that excitation light is focused at the tip of NW, the remote excitation configuration demonstrated lower background intensities [77].

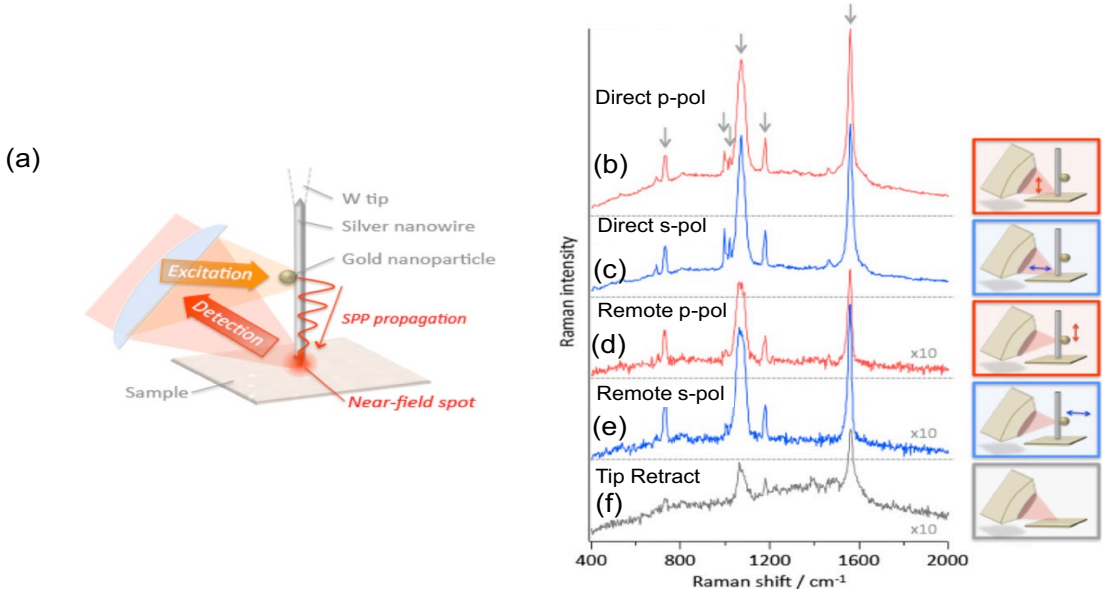


**Figure 1.9.** Remotely excited AgNW TERS probe. (a) Schematic illustration of AgNW TERS probe remotely excited using gold nanoparticle. (b) Raman spectrum of benzenethiol-modified Au with different excitation when excitation laser is directly focused at the tip with (a) and s polarization (b), when the laser is remotely focused at the gold nanoparticle with p (c) and s polarization (d), when the laser is focused on the substrate without AgNW tip. Reproduced with permission [79].

## 1.5. Conclusion and outlook

In this chapter, we compared NW waveguides made of dielectric and metallic materials. Dielectric NW guides light via total internal reflection, and it has several advantages over plasmonic waveguide such as better chemical and thermal stability and no Ohmic loss.

However, diffraction limited diameter of the dielectric NW limits subwavelength light confinement. Propagation of light as SPPs in plasmonic NW enables confinement of the light at the interface between metal and dielectrics. The diameter of the waveguide can be decreased beyond diffraction limit but strong confinement of light due to electron oscillation must be accompanied and therefore, propagation loss increases. To reduce the propagation loss, both longer skin depth and less binding area are required. The hybrid plasmonic waveguide can provide a solution to the propagation loss by having a small mode volume leading to a minimal binding area with the metal surface. A significant increase of propagation length was achieved with subwavelength confinement. However, the loss is still larger than dielectric waveguide, and low coupling in and out efficiency is another problem needs to be solved to be generally adopted. For optoelectronics, we have mainly discussed three main components: light emitter, waveguide, and a light detector. There has been a significant improvement of the main components for the last two decades using NWs made via the bottom-up strategy.

Remarkable performance has been demonstrated with diverse semi-conducting NWs. Nonetheless, to realize optoelectronics, further development with auxiliary elements such as interconnector, coupler, splitter, polarizer, modulator, etc. should be accompanied. Above all, integration technique of chemically synthesized NWs onto semiconducting panel remains challenging and should be addressed to take advantages of single crystallinity.

On the other hand, substantially large room for sensing and imaging with optical NW waveguide still exist. Especially, exploitation of evanescence wave either using dielectric

waveguide and a metallic waveguide for sensing is in its infancy. Combination of the evanescence wave with spectroscopy, label-free analysis with high sensitivity or compositional imaging with nanoscale resolution will open new and promising avenues shortly and bring a bright impact in biology and material characterization fields.

## 1.6. References


1. Ditlbacher, H.; Hohenau, A.; Wagner, D.; Kreibig, U.; Rogers, M.; Hofer, F.; Aussenegg, F. R.; Krenn, J. R., Silver nanowires as surface plasmon resonators. *Phys Rev Lett* **2005,** *95* (25), 257403.

2. Sanders, A. W.; Routenberg, D. A.; Wiley, B. J.; Xia, Y.; Dufresne, E. R.; Reed, M. A., Observation of plasmon propagation, redirection, and fan-out in silver nanowires. *Nano letters* **2006,** *6* (8), 1822-1826.

3. Pyayt, A. L.; Wiley, B.; Xia, Y.; Chen, A.; Dalton, L., Integration of photonic and silver nanowire plasmonic waveguides. *Nature nanotechnology* **2008,** *3* (11), 660-665.

4. Shegai, T.; Huang, Y.; Xu, H.; Käll, M., Coloring fluorescence emission with silver nanowires. *Applied Physics Letters* **2010,** *96* (10), 103114.

5. Wild, B.; Cao, L.; Sun, Y.; Khanal, B. P.; Zubarev, E. R.; Gray, S. K.; Scherer, N. F.; Pelton, M., Propagation lengths and group velocities of plasmons in chemically synthesized gold and silver nanowires. *ACS nano* **2012,** *6* (1), 472-482.

6. Yan, R.; Pausauskie, P.; Huang, J.; Yang, P., Direct photonic–plasmonic coupling and routing in single nanowires. *Proceedings of the National Academy of Sciences* **2009,** *106* (50), 21045-21050.

7. Ma, Y.; Li, X.; Yu, H.; Tong, L.; Gu, Y.; Gong, Q., Direct measurement of propagation losses in silver nanowires. *Optics letters* **2010,** *35* (8), 1160-1162.

8. Wang, W.; Yang, Q.; Fan, F.; Xu, H.; Wang, Z. L., Light propagation in curved silver nanowire plasmonic waveguides. *Nano letters* **2011,** *11* (4), 1603-1608.

9. Kim, S.; Bailey, S.; Liu, M.; Yan, R., Decoupling co-existing surface plasmon polariton (SPP) modes in a nanowire plasmonic waveguide for quantitative mode analysis. *Nano Research* **2017,** *10* (7), 2395-2404.

10. Solis Jr, D.; Chang, W.-S.; Khanal, B. P.; Bao, K.; Nordlander, P.; Zubarev, E. R.; Link, S., Bleach-imaged plasmon propagation (BlIPP) in single gold nanowires. *Nano letters* **2010,** *10* (9), 3482-3485.

11. Nauert, S.; Paul, A.; Zhen, Y.-R.; Solis Jr, D.; Vigderman, L.; Chang, W.-S.; Zubarev, E. R.; Nordlander, P.; Link, S., Influence of cross sectional geometry on surface plasmon polariton propagation in gold nanowires. *ACS nano* **2013,** *8* (1), 572-580.

12. Li, X.; Guo, X.; Wang, D.; Tong, L., Propagation losses in gold nanowires. *Optics Communications* **2014,** *323*, 119-122.

13. Yu, K.; Devadas, M. S.; Major, T. A.; Lo, S. S.; Hartland, G. V., Surface plasmon polariton propagation and coupling in gold nanostructures. *The Journal of Physical Chemistry C* **2014,** *118* (16), 8603-8609.

14. Chiu, G.-T.; Shaw, J. M., Optical lithography: introduction. *Ibm J Res Dev* **1997,** *41* (1.2), 3-6.

15. Tallents, G.; Wagenaars, E.; Pert, G., Optical lithography: lithography at EUV wavelengths. *Nature Photonics* **2010,** *4* (12), 809-811.

16. Kratschmer, E.; Rishton, S.; Kern, D.; Chang, T., Quantitative analysis of resolution and stability in nanometer electron beam lithography. *Journal of Vacuum Science & Technology B: Microelectronics Processing and Phenomena* **1988,** *6* (6), 2074-2079.

17. Khanna, V. K., Top-Down Nanofabrication. In *Integrated Nanoelectronics*, Springer: 2016; pp 381-396.

18. Zhang, A.; Zheng, G.; Lieber, C. M., *Nanowires: Building blocks for nanoscience and nanotechnology*. Springer: 2016.

19. Morales, A. M.; Lieber, C. M., A laser ablation method for the synthesis of crystalline semiconductor nanowires. *Science* **1998,** *279* (5348), 208-211.

20. Wu, Y.; Yang, P., Germanium nanowire growth via simple vapor transport. *Chemistry of Materials* **2000,** *12* (3), 605-607.

21. Law, M.; Goldberger, J.; Yang, P., Semiconductor nanowires and nanotubes. *Annu. Rev. Mater. Res.* **2004,** *34*, 83-122.

22. Choi, H.-J., Vapor–liquid–solid growth of semiconductor nanowires. In *Semiconductor Nanostructures for Optoelectronic Devices*, Springer: 2012; pp 1-36.

23. Heitsch, A. T.; Fanfair, D. D.; Tuan, H.-Y.; Korgel, B. A., solution− liquid− solid (SLS) growth of silicon nanowires. *Journal of the American Chemical Society* **2008,** *130* (16), 5436-5437.

24. Lu, X.; Fanfair, D. D.; Johnston, K. P.; Korgel, B. A., High yield solution− liquid− solid synthesis of germanium nanowires. *Journal of the American Chemical Society* **2005,** *127* (45), 15718-15719.

25. Puthussery, J.; Lan, A.; Kosel, T. H.; Kuno, M., Band-filling of solution-synthesized CdS nanowires. *Acs Nano* **2008,** *2* (2), 357-367.

26. Kuno, M.; Ahmad, O.; Protasenko, V.; Bacinello, D.; Kosel, T. H., Solution-based straight and branched CdTe nanowires. *Chemistry of materials* **2006,** *18* (24), 5722-5732.

27. Sun, J.; Buhro, W. E., The Use of Single-Source Precursors for the Solution–Liquid–Solid Growth of Metal Sulfide Semiconductor Nanowires. *Angewandte Chemie* **2008,** *120* (17), 3259-3262.

28. Fanfair, D. D.; Korgel, B. A., Twin-related branching of solution-grown ZnSe nanowires. *Chemistry of Materials* **2007,** *19* (20), 4943-4948.

29. Wang, F.; Dong, A.; Sun, J.; Tang, R.; Yu, H.; Buhro, W. E., Solution− liquid− solid growth of semiconductor nanowires. *Inorganic chemistry* **2006,** *45* (19), 7511-7521.

30. Fanfair, D. D.; Korgel, B. A., Bismuth nanocrystal-seeded III-V semiconductor nanowire synthesis. *Crystal growth & design* **2005,** *5* (5), 1971-1976.

31. Hochbaum, A. I.; Fan, R.; He, R.; Yang, P., Controlled growth of Si nanowire arrays for device integration. *Nano Lett* **2005,** *5* (3), 457-460.

32. Huang, M. H.; Mao, S.; Feick, H.; Yan, H.; Wu, Y.; Kind, H.; Weber, E.; Russo, R.; Yang, P., Room-temperature ultraviolet nanowire nanolasers. *science* **2001,** *292* (5523), 1897-1899.

33. Mohan, P.; Motohisa, J.; Fukui, T., Controlled growth of highly uniform, axial/radial direction-defined, individually addressable InP nanowire arrays. *Nanotechnology* **2005,** *16* (12), 2903.

34. Kuykendall, T.; Pauzauskie, P. J.; Zhang, Y.; Goldberger, J.; Sirbuly, D.; Denlinger, J.; Yang, P., Crystallographic alignment of high-density gallium nitride nanowire arrays. *Nature materials* **2004,** *3* (8), 524-528.

35. Greene, L. E.; Law, M.; Goldberger, J.; Kim, F.; Johnson, J. C.; Zhang, Y.; Saykally, R. J.; Yang, P., Low-temperature wafer-scale production of ZnO nanowire arrays. *Angewandte Chemie International Edition* **2003,** *42* (26), 3031-3034.

36. Sun, Y.; Xia, Y., Large-Scale Synthesis of Uniform Silver Nanowires Through a Soft, Self-Seeding, Polyol Process. *Advanced Materials* **2002,** *14* (11), 833-837.

37. Lifante, G., *Integrated photonics: fundamentals*. Wiley Online Library: 2003.

38. Tong, X. C., *Advanced materials for integrated optical waveguides*. Springer: 2014.

39. Gudiksen, M. S.; Lauhon, L. J.; Wang, J.; Smith, D. C.; Lieber, C. M., Growth of nanowire superlattice structures for nanoscale photonics and electronics. *Nature* **2002,** *415* (6872), 617-620.

40. Qian, F.; Gradecak, S.; Li, Y.; Wen, C.-Y.; Lieber, C. M., Core/multishell nanowire heterostructures as multicolor, high-efficiency light-emitting diodes. *Nano letters* **2005,** *5* (11), 2287-2291.

41. Brubaker, M. D.; Blanchard, P. T.; Schlager, J. B.; Sanders, A. W.; Roshko, A.; Duff, S. M.; Gray, J. M.; Bright, V. M.; Sanford, N. A.; Bertness, K. A., On-chip optical interconnects made with gallium nitride nanowires. *Nano letters* **2013,** *13* (2), 374-377.

42. Tchernycheva, M.; Messanvi, A.; de Luna Bugallo, A.; Jacopin, G.; Lavenus, P.; Rigutti, L.; Zhang, H.; Halioua, Y.; Julien, F.; Eymery, J., Integrated photonic platform based on InGaN/GaN nanowire emitters and detectors. *Nano letters* **2014,** *14* (6), 3515-3520.

43. Ma, Y.; Guo, X.; Wu, X.; Dai, L.; Tong, L., Semiconductor nanowire lasers. *Advances in Optics and Photonics* **2013,** *5* (3), 216-273.

44. Zapien, J.; Liu, Y.; Shan, Y.; Tang, H.; Lee, C.; Lee, S., Continuous near-infrared-to-ultraviolet lasing from II-VI nanoribbons. *Applied physics letters* **2007,** *90* (21), 213114.

45. Pan, A.; Zhou, W.; Leong, E. S.; Liu, R.; Chin, A. H.; Zou, B.; Ning, C., Continuous alloy-composition spatial grading and superbroad wavelength-tunable nanowire lasers on a single chip. *Nano letters* **2009,** *9* (2), 784-788.

46. Liu, Y.; Zapien, J. A.; Shan, Y.; Geng, C. Y.; Lee, C. S.; Lee, S. T., Wavelength-Controlled Lasing in ZnxCd1−xS Single-Crystal Nanoribbons. *Advanced Materials* **2005,** *17* (11), 1372-1377.

47. Maslov, A.; Ning, C., Modal gain in a semiconductor nanowire laser with anisotropic bandstructure. *IEEE journal of quantum electronics* **2004,** *40* (10), 1389-1397.

48. Yan, R.; Gargas, D.; Yang, P., Nanowire photonics. *Nature photonics* **2009,** *3* (10), 569.

49. Saleh, B.; Teich, M., Fundamentals of Photonics. 2nd Wiley-Interscience. *New York* **2007**, 1200.

50. Gao, H.; Fu, A.; Andrews, S. C.; Yang, P., Cleaved-coupled nanowire lasers. *Proceedings of the National Academy of Sciences* **2013,** *110* (3), 865-869.

51. Duan, X.; Huang, Y.; Agarwal, R.; Lieber, C. M., Single-nanowire electrically driven lasers. *Nature* **2003,** *421* (6920), 241.

52. Duan, X.; Huang, Y.; Agarwal, R.; Lieber, C. M., Single-nanowire electrically driven lasers. *Nature* **2003,** *421* (6920), 241-245.

53. Guo, X.; Ying, Y.; Tong, L., Photonic nanowires: From subwavelength waveguides to optical sensors. *Accounts Chem Res* **2013,** *47* (2), 656-666.

54. Xiao, Y.; Meng, C.; Wang, P.; Ye, Y.; Yu, H.; Wang, S.; Gu, F.; Dai, L.; Tong, L., Single-nanowire single-mode laser. *Nano letters* **2011,** *11* (3), 1122-1126.

55. Garnett, E.; Yang, P., Light trapping in silicon nanowire solar cells. *Nano letters* **2010,** *10* (3), 1082-1087.

56. Yeh, L. K.; Lai, K. Y.; Lin, G. J.; Fu, P. H.; Chang, H. C.; Lin, C. A.; He Jr, H., Giant efficiency enhancement of GaAs solar cells with graded antireflection layers based on syringelike ZnO nanorod arrays. *Advanced Energy Materials* **2011,** *1* (4), 506-510.

57. Kempa, T. J.; Cahoon, J. F.; Kim, S.-K.; Day, R. W.; Bell, D. C.; Park, H.-G.; Lieber, C. M., Coaxial multishell nanowires with high-quality electronic interfaces and tunable optical cavities for ultrathin photovoltaics. *Proceedings of the National Academy of Sciences* **2012,** *109* (5), 1407-1412.

58. Cao, L.; White, J. S.; Park, J.-S.; Schuller, J. A.; Clemens, B. M.; Brongersma, M. L., Engineering light absorption in semiconductor nanowire devices. *Nature materials* **2009,** *8* (8), 643-647.

59. LaPierre, R.; Robson, M.; Azizur-Rahman, K.; Kuyanov, P., A review of III–V nanowire infrared photodetectors and sensors. *Journal of Physics D: Applied Physics* **2017,** *50* (12), 123001.

60. Miao, J.; Hu, W.; Guo, N.; Lu, Z.; Zou, X.; Liao, L.; Shi, S.; Chen, P.; Fan, Z.; Ho, J. C., Single InAs nanowire room-temperature near-infrared photodetectors. *ACS nano* **2014,** *8* (4), 3628-3635.

61. Li, Z.; Yuan, X.; Fu, L.; Peng, K.; Wang, F.; Fu, X.; Caroff, P.; White, T. P.; Tan, H. H.; Jagadish, C., Room temperature GaAsSb single nanowire infrared photodetectors. *Nanotechnology* **2015,** *26* (44), 445202.

62. Ma, L.; Hu, W.; Zhang, Q.; Ren, P.; Zhuang, X.; Zhou, H.; Xu, J.; Li, H.; Shan, Z.; Wang, X., Room-temperature near-infrared photodetectors based on single heterojunction nanowires. *Nano letters* **2014,** *14* (2), 694-698.

63. Mayer, B.; Rudolph, D.; Abstreiter, G.; Bracher, G.; Koblmüller, G.; Finley, J. J.; Schnell, J.; Winnerl, J.; Treu, J.; Müller, K., Lasing from individual GaAs-AlGaAs core-shell nanowires up to room temperature. *Nature communications* **2013,** *4*, 2931.

64. Jiang, N.; Parkinson, P.; Gao, Q.; Breuer, S.; Tan, H. H.; Wong-Leung, J.; Jagadish, C., Long minority carrier lifetime in Au-catalyzed GaAs/AlxGa1− xAs core-shell nanowires. *Applied Physics Letters* **2012,** *101* (2), 023111.

65. Titova, L.; Hoang, T. B.; Jackson, H.; Smith, L.; Yarrison-Rice, J.; Kim, Y.; Joyce, H.; Tan, H.; Jagadish, C., Temperature dependence of photoluminescence from single core-shell GaAs–AlGaAs nanowires. *Applied Physics Letters* **2006,** *89* (17), 173126.

66. Tong, L.; Gattass, R. R.; Ashcom, J. B.; He, S.; Lou, J.; Shen, M.; Maxwell, I.; Mazur, E., Subwavelength-diameter silica wires for low-loss optical wave guiding. *Nature* **2003,** *426* (6968), 816-819.

67. Sirbuly, D. J.; Tao, A.; Law, M.; Fan, R.; Yang, P., Multifunctional nanowire evanescent wave optical sensors. *Advanced Materials* **2007,** *19* (1), 61-66.

68. Yan, R.; Park, J.-H.; Choi, Y.; Heo, C.-J.; Yang, S.-M.; Lee, L. P.; Yang, P., Nanowire-based single-cell endoscopy. *Nature nanotechnology* **2012,** *7* (3), 191-196.

69. Shambat, G.; Kothapalli, S.-R.; Provine, J.; Sarmiento, T.; Harris, J.; Gambhir, S. S.; Vučković, J., Single-cell photonic nanocavity probes. *Nano letters* **2013,** *13* (11), 4999-5005.

70. Lee, J.; Lee, H. R.; Pyo, J.; Jung, Y.; Seo, J. Y.; Ryu, H. G.; Kim, K. T.; Je, J. H., Quantitative Probing of Cu2+ Ions Naturally Present in Single Living Cells. *Advanced Materials* **2016,** *28* (21), 4071-4076.

71. Lu, G.; De Keersmaecker, H.; Su, L.; Kenens, B.; Rocha, S.; Fron, E.; Chen, C.; Van Dorpe, P.; Mizuno, H.; Hofkens, J., Live-Cell SERS Endoscopy Using Plasmonic Nanowire Waveguides. *Advanced Materials* **2014,** *26* (30), 5124-5128.

72. Li, Z.; Bao, K.; Fang, Y.; Huang, Y.; Nordlander, P.; Xu, H., Correlation between incident and emission polarization in nanowire surface plasmon waveguides. *Nano letters* **2010,** *10* (5), 1831-1835.

73. Oulton, R. F.; Sorger, V. J.; Genov, D.; Pile, D.; Zhang, X., A hybrid plasmonic waveguide for subwavelength confinement and long-range propagation. *nature photonics* **2008,** *2* (8), 496.

74. He, X. Y.; Wang, Q. J.; Yu, S. F., Numerical study of gain-assisted terahertz hybrid plasmonic waveguide. *Plasmonics* **2012,** *7* (3), 571-577.

75. Sorger, V. J.; Ye, Z.; Oulton, R. F.; Wang, Y.; Bartal, G.; Yin, X.; Zhang, X., Experimental demonstration of low-loss optical waveguiding at deep sub-wavelength scales. *Nature Communications* **2011,** *2*, 331.

76. Fedyanin, D. Y.; Yakubovsky, D. I.; Kirtaev, R. V.; Volkov, V. S., Ultralow-loss CMOS copper plasmonic waveguides. *Nano letters* **2015,** *16* (1), 362-366.

77. Fujita, Y.; Walke, P.; De Feyter, S.; Uji-i, H., Remote excitation-tip-enhanced Raman scattering microscopy using silver nanowire. *Japanese Journal of Applied Physics* **2016,** *55* (8S1), 08NB03.

# Chapter 2

# Characterization of propagating surface plasmon mode in Ag nanowire

As discussed in chapter 1, SPP modes with subwavelength electromagnetic field confinements can enhance the field strength and have been used as the enabling components for various appealing plasmonic applications such as sensors, plasmonic lasers, and plasmonic optoelectronics. However, the enhanced mode confinement in 1D SPP applications amplifies the plasmonic losses originating from both radiative scattering due to surface roughness and nonradiative decay from Joule heating. Both constrain the SPP propagation length from a few micrometers to hundreds of micrometers, depending on the mode profiles. Therefore, systematically characterizing the propagation lengths and mode indices of various SPP modes is essential for the development and optimization of SPP applications.

Among the candidates for deep sub-wavelength plasmonic waveguides, silver nanowires (AgNWs), which can be chemically synthesized in large scale and with high crystallinity and atomically smooth surfaces, have drawn particular attentions due to their low ohmic damping and negligible scattering loss. AgNWs have been a subject of intensive study and have exhibited as appealing nano-optical components for photonic circuits[1-5], light sources[6], photodetectors[7-8], *etc*. The understanding of the basic characteristics of different 1D-SPP modes in AgNWs, such as effective mode indices and propagation lengths, provides key guidelines for the design of AgNW-based plasmonic devices. During the last

10 years, the effective mode indices and propagation lengths for different nanowire diameters, dielectric environments, and excitation wavelengths have been measured through various techniques, including Fabry–Pérot resonance[9], sidewall-scattering[10-11], fluorescent mapping[12-13], nanofiber coupling[2, 14-15]. However, significant inconsistencies exist among different reports[16]. For instance, at near IR wavelengths (785 to 830 nm), propagation lengths measured for AgNWs around 100 nm in diameter ranges from 3 to 12 μm[9-10, 12], while others report a similar propagation length (12 μm) for much thicker AgNWs (750 nm) under the same condition[15], which should have much lower loss compared to 100 nm nanowires. A major cause of such a large discrepancy is the lack of a method that separately addresses different modes co-existing on the same nanowire, which have different mode profiles and therefore different characteristics. In most studies, the dominating modes determined the measured results.

In this chapter, an interference method to individually characterize SPP modes supported by AgNWs will be introduced and discussed. By extracting information from the propagation-distance-dependent far-field radiation intensity of the scattered light from the nanowire tip, we could distinguish different SPP modes supported by AgNWs of different diameters and under excitation at different wavelengths, and derive their respective mode indices, propagation lengths, and, more importantly, the relative weights of co-existing modes. We also detected the existence of long propagation lengths of more than 100 μm on small-diameter AgNWs. In particular, we proved that SPP modes can be selectively excited by varying the nanowire diameter.

## 2.1. Synthesis of Ag nanowire

AgNW synthesized via polyol-mediated reduction can minimize the scattering loss from grain boundaries, structural defects and surface roughness[5]. These AgNWs have been demonstrated to have a more remarkably lower propagation loss than their lithographically defined counterparts[6]. Such low ohmic loss arises from (1) the single crystalline nature, (2) chemical homogeneity or low impurity level, and (3) atomically smooth surfaces. All of these mentioned factors effectively reduce the electron scattering during the collective electron oscillations in the plasmonic waveguide. Another merit of the AgNW is its sharp tip; where energy (carried as SPs) is released into free space. Due to the sharp tip, the illumination volume is so small that significantly high spatial resolution can be achieved in the application of the near field imaging.

### 2.1.1. Materials

$AgNO_3$ (99+%), PVP powder (avg Mw # 55 000), $CuCl_2 \cdot 2H_2O$ (99.999+%), $Cu(NO_3)_2 \cdot 2.5H_2O$ (99.999%), and CuCl (99.995+%) were all purchased from Aldrich. Ethylene glycol (99%) was purchased from J.T. Baker.

### 2.1.2. AgNW synthesis procedure

Long AgNWs with diverse thickness were first synthesized via polyol-mediated reduction of $AgNO_3$ in the presence of polyvinylpyrrolidone (PVP), which guides one dimensional growth[17]. 1.5ml of a 0.094M $AgNO_3$ and 1.5ml of a 0.147 M PVP in ethylene glycol (EG)

were prepared. $AgNO_3$ dissolved in EG was stored at different temperatures (0 ~ 60 ℃). While it was being prepared, a pear-shaped flask with 5 mL of ethylene glycol and a stir bar was immersed in a silicon oil bath at 152 ℃. Then, it was heated for 15 minutes under magnetic stirring at 400 rpm. After the EG in the pear-shaped flask had been heated, $CuCl_2$ was added and allowed to heat up for an additional 15 minutes. 125 μl of the 0.147 M PVP solution was injected into the heated EG, along with 1.25ul 0.094 M $AgNO_3$ solution. The injection was conducted every minute until all the solutions were consumed[18]. We stopped the reaction upon nanowire formation by removing the flask from the silicon oil bath and letting it cool after the solution color was changed to gray. After cooling for 15 minutes, the products were washed and purified with ethanol by centrifugation at 1500 RPM for 40 minutes at least 5 times to remove all impurities. All the chemicals were purchased from Aldrich except EG which was purchased from J.T. Baker.

## 2.2. Methods

### 2.2.1. Measurement of the emitted light intensity at the tip of the AgNW.

AgNWs with diameters ranging from 100 nm to 500nm dispersed in ethanol were drop-cast on a PDMS film. Ethanol was evaporated slowly while the AgNWs drop was moved on the substrate using a nitrogen gun. The AgNWs with different diameters were picked up with a tungsten probe mounted in a triple-axis micromanipulator (Shutter Instrument) and positioned at the edge of the PDMS. The tapered optical fiber was mounted in the manipulator to move the fiber in three axis directions. The unpolarized laser lights with

532 and 658 nm wavelengths were coupled to the AgNWs from a tapered optical fiber. The intensity (~a few μW) of the light at the tip of the AgNW was measured while the optical fiber tip glides toward to the end of the AgNWs. An upright optical microscope (Nikon Eclipse Ni-U) with a 50X microscope objective with NA 0.6 and black-illuminated CCD camera (Zyla 5.5, Andor, Belfast, UK) was used to collect and capture the light signal at the tip of the NW.

### 2.2.2. Numerical simulation to support the experimental results using COMSOL.

Electromagnetic simulations were carried out using a commercial finite element analysis software (Comsol Multiphysics, v5.1). The propagation lengths and effective mode indices as a function of the AgNW diameter were calculated using a 2-D mode analysis solver. The dielectric constants ($\varepsilon_{r,532nm} = -11.755 - 0.37038i$ and $\varepsilon_{r,658nm} = -19.991 - 0.45028i$) for the AgNWs were obtained from Johnson and Christy[19].

## 2.3. Excitation and measurement of the propagating surface plasmon.

Figure 2.1(a) schematically illustrates the experimental concept. To characterize the intrinsic SPP properties and exclude the effects of the substrate, we placed the chemically synthesized AgNWs on the edge of a polydimethylsiloxane (PDMS) block, with 50–60 μm of their length suspended in air. The tapered tip of a laser-coupled optical fiber, which was controlled by a high-precision motorized micromanipulator, was then brought into gentle contact with the unsupported segment of the AgNW to excite its SPP modes. The effective indices of the SPP modes are higher than the index of air, so light emission appeared only at the fiber–nanowire junction and the nanowire tip through a scattering process. A 50×

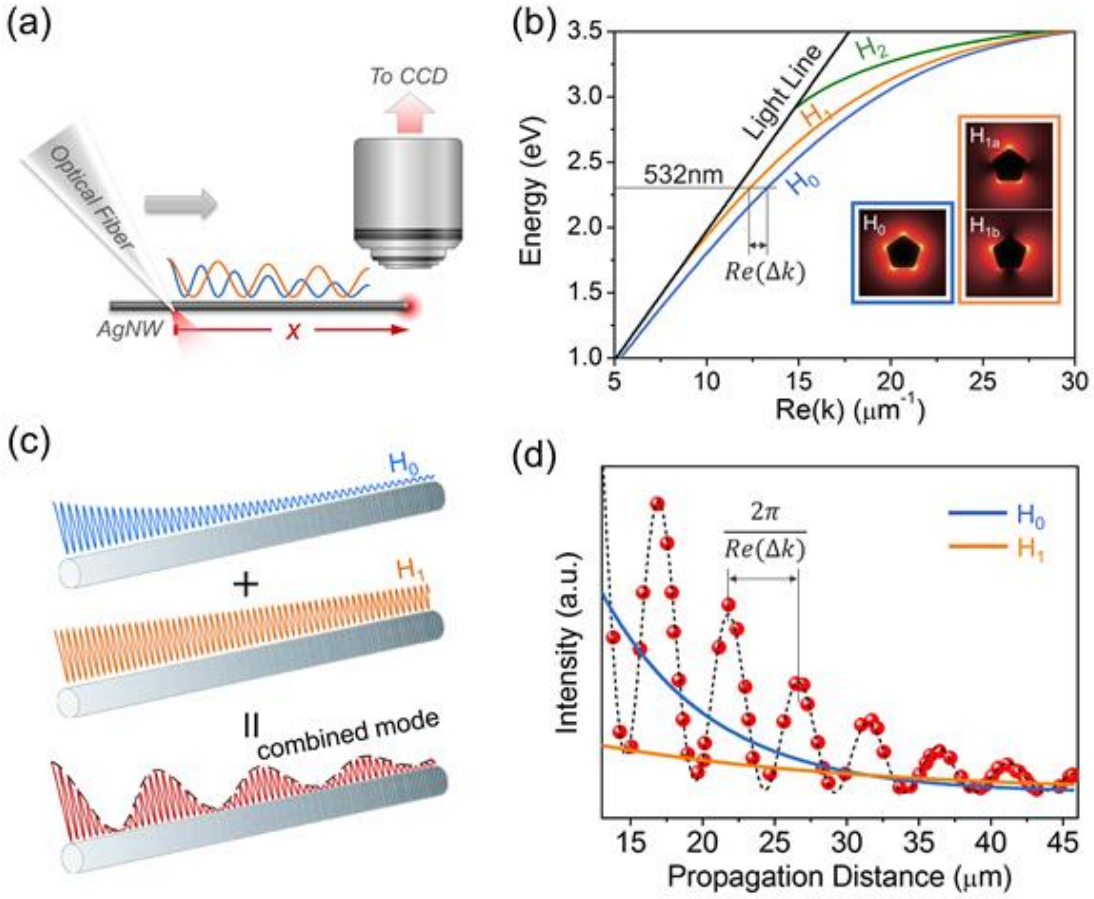


**Figure 2.1** Excitation and propagation of SPP modes on a free-standing AgNW. (a) Schematic illustration of the experimental setup. A tapered optical fiber tip was brought into contact with a suspended AgNW. SPPs were excited at the junction and propagated down to the distal AgNW tip, where they were scattered into free space. The fiber tip was then slid along the AgNW, varying the propagation distance $x$. The AgNW tip emission was collected by an objective lens and recorded by a CCD camera. (b) Dispersion curves of the lowest-order SPP modes ($H_0$, $H_1$, and $H_2$) in AgNW. Insets: electric field ($|E|$) distribution of $H_0$ and the two degenerate $H_1$ modes. (c) Schematic showing the generation of plasmonic beating from interference of the $H_0$ and $H_1$ modes. (d) Measured AgNW tip emission intensity (red dots) plotted as a function of the propagation distance $x$. The plasmonic beating was reflected in the periodic oscillation in the intensity of the AgNW tip emission. The period of the beating is defined by the difference between the wave vectors of the $H_0$ and $H_1$ modes. Blue and orange curves are the attenuation curves of the $H_0$ and $H_1$ modes, respectively, deconvoluted from the experimental data. The AgNW is 160 nm in diameter. The incident light has a wavelength $\lambda$ of 532 nm.

microscope objective lens was used to image the emission patterns, which were recorded by an s-CMOS Charge-coupled device (CCD) camera. The fiber tip was then slid along the AgNW toward its tip (red arrow in Figure 2.1(a)) to vary the distance of SPP propagation x, which is defined as the distance between the contact point and the suspended AgNW tip. To ensure measurement accuracy, we avoided any mechanical deformation of the AgNW during measurement by programming the micromanipulator to move the fiber tip exactly along the AgNW. Because of the uniform nanowire diameter and its atomically smooth surface in the Electronic Supplementary Material (ESM)), we can safely assume that the coupling efficiency between the fiber tip and the AgNW remains constant as the fiber tip glides along the AgNW. The intensity of the collected far-field tip emission, therefore, reflected the strength of the local electromagnetic field at the nanowire tip and can be used to extract information on the intrinsic SPP modes excited on and supported by the free-standing AgNW. The red dots in **Figure 2.1(d)** show the far-field intensities measured as a function of x as the fiber tip glides toward the nanowire tip under 532 nm laser excitation.

### 2.4. Measurement reliability

A possible source of experimental uncertainty in our experiment is the slight variation (±5°) of the fiber-nanowire angle for different measurements. The coupling efficiency and the weight of the SPP modes may be influenced by the change of coupling angles. We performed a series of experiments to check the dependency of effective index, propagation

length, and mode amplitude to the fiber angle. The measurement was conducted under 658 excitation light and shown in **Figure 2.2**.

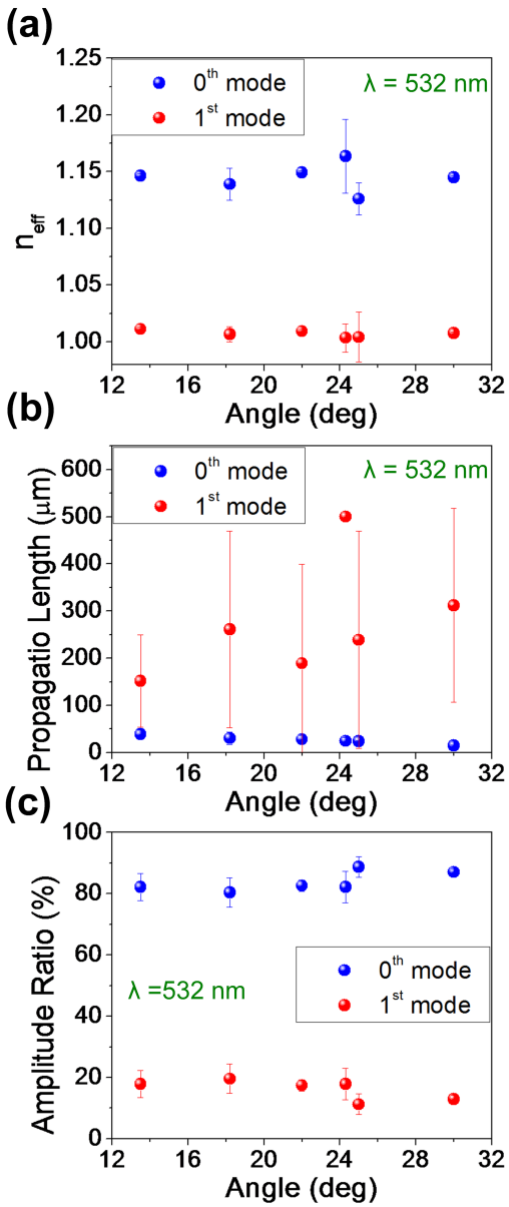


**Figure 2.2.** Reliability of the SPP modes analysis excited by a tapered optical fiber. The dependency of the coupling angle on the effective refractive indices. **(a)**, propagation length **(b)**, and amplitude ratio **(c)** for the two lowest modes are investigated.

The coupling angle between the AgNW and the optical fiber was altered from 13° to 30°, which is the typical range in the measurements. An AgNW with a 160-nm in diameter was used. For each angle, the tip of the optical fiber was handled by the micromanipulator to move toward to the end of the AgNW four times and the intensity of the emitted light was measured. Then, the effective mode index $n_{eff}$, propagation lengths $L_{Hm}$, and amplitudes of the participating modes were calculated using the fitting Equation (1) in the text. Except for the propagation length of the 1st order mode, there is almost no variation of the mean $n_{eff}$, propagation length, and amplitudes with a changing angle. The variation of the propagation lengths for the 1st order mode is natural because (1) the propagation lengths are much longer than the measured distance range of the nanowire and (2) its effective mode index is close to 1 and consequently, it is hard to decouple it from the free space mode when the measured distance is short.

Nevertheless, the results show that the SPPs in the AgNW is independent of the angle in the range of 13° and 30°, which is favorable for accurate mode analysis in our experiment. The small error bars also verify that the consistency of our mode analysis method.

### 2.5. Calculation of mode index and propagation losses

The intensity oscillations of the far-field signals in Figure 2.1(d) originate from beating between multiple SPP modes launched at the fiber–nanowire junction. As shown in Figure 2.1(b), full-wave mode analysis using FEA (finite element analysis) demonstrated that a AgNW 300 nm in diameter can support two SPP modes ($H_0$ and $H_1$) at visible frequencies. To simplify the discussion, we define the diagonal dimension of the pentagonal cross

section of the AgNW as its diameter. The experimentally measured permittivity data were used to describe the silver metal in the simulation (see Methods for details). The

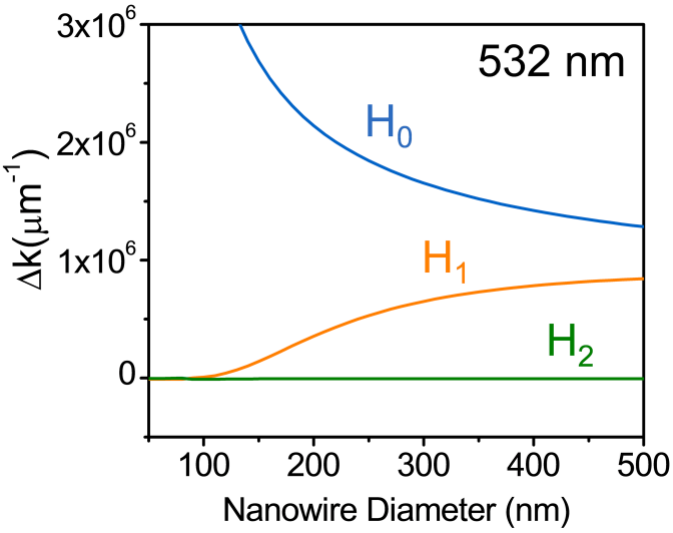


**Figure 2.3.** Momentum difference between free-space photons and the three lowest order SPP modes of AgNWs under 532 nm excitation. The $H_0$ mode doesn't have a cut-off diameter. The cut-off diameter of $H_1$ modes is ~110 nm, where the $H_1$ (orange) curve meets the zero-Δk line. The cut-off diameter of $H_2$ modes is larger than 500 nm.

fundamental mode (labeled $H_0$) has no cutoff frequency, which is similar to the case of the fundamental $TM_0$ mode of a circular metallic nanowire. Owing to the pentagonal ($D_{5h}$) symmetry of the AgNW cross section, the second-lowest mode ($H_1$) of a circular waveguide splits into two degenerate modes (labeled $H_{1a}$ and $H_{1b}$, with the *E* field illustrated in the insets of Figure 2.1(b)) with cutoff wavelengths of around 750 nm (1.65 eV) for the calculated diameter in air. The third-lowest mode (denoted as $H_2$) has a cutoff wavelength in the ultraviolet (2.7 eV) and therefore is not excited by the visible lasers used in this work. Although Figure 2.1(b) was derived for 300 nm AgNWs, this conclusion holds true for AgNWs with diameters ranging from ~110 to 500 nm (Figure 2.3 in the ESM).

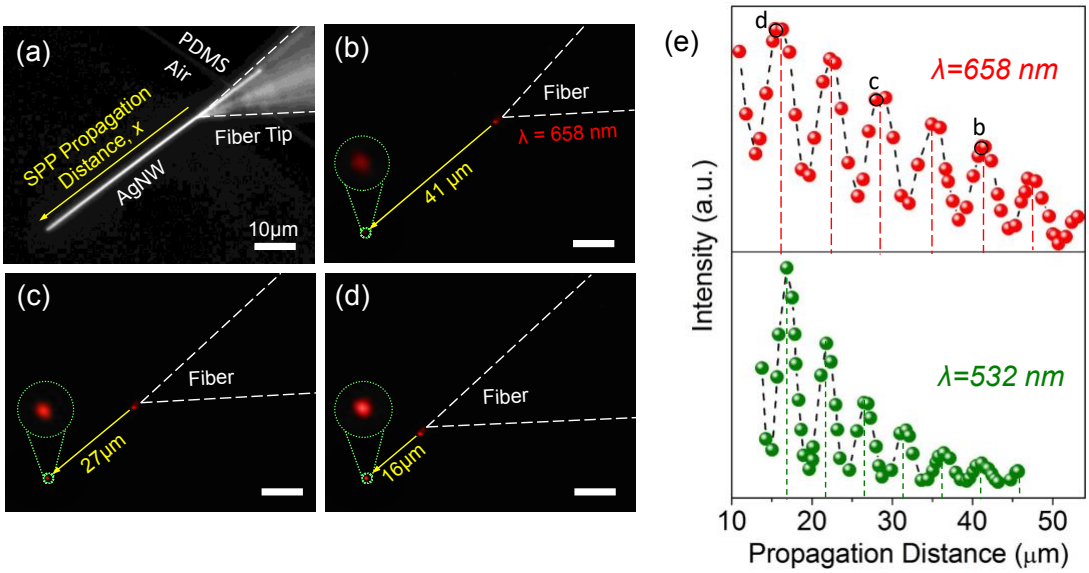


**Figure 2.4** Measurement of the SPP propagation length in a free-standing AgNW. (a) Dark-field optical image of the measurement setup. A AgNW was placed on a PDMS substrate with 50–60 μm suspended from the edge. The tapered tip of a laser-coupled optical fiber was put into physical contact with the AgNW to excite its SPPs. The SPPs propagated along the AgNW to its distal end, where they were scattered back into free space. The far-field emission at the suspended AgNW tip was collected as the optical fiber tip was slid along the AgNW. (b)–(d) Waveguide images (back illumination off, laser on) of the AgNW at different SPP propagation distances *x*. Insets: enlarged images of the tip emission spot, the intensity of which increased as *x* decreased. (e) Tip emission intensity measured as a function of *x* under 658 nm (top) and 532 nm (bottom) excitation. Circled points labeled b–d correspond to images (b)–(d) on the left.

Under a laser excitation of 532 nm, three lowest-order SPP modes ($H_0$, $H_{1a}$, and $H_{1b}$) can be launched into the AgNW. To reduce the complexity of the mode analysis, only one of the two degenerate $H_1$ modes was excited in our experiments. This was achieved by setting the polarization in the single-mode fiber to be linear, with the electric field perpendicular to the interface between the AgNW and the fiber, in which case only one of the $H_1$ modes (defined as $H_{1a}$) was excited, and the other ($H_{1b}$) was suppressed. The polarization state was controlled by a manual fiber polarization controller (Thorlabs, Inc.) and was confirmed

by examining the output intensity from the fiber tip through a linear polarizer using a CCD camera placed in front of the fiber tip. Because the two remaining modes ($H_0$ and $H_{1a}$) have different wavevectors ($\boldsymbol{K}_{spp}^{H0}$ and $\boldsymbol{K}_{spp}^{H1}$), a beating pattern with a period ($\Lambda$) of $2\pi/\mathrm{Re}(\Delta k)$ was formed on the nanowire, where $\Delta k$ is the difference between the two wavevectors. This process is illustrated in Figure 2.1(c). Moving the tapered fiber tip along the nanowire is equivalent to changing the propagation distance $x$ for both modes and leads to variation of the SPP intensity at the end of the nanowire, and also modulation of the emission intensity $I$, as shown in Figure 2.1(d). Figure 2.4(a) is a dark-field optical image of the typical measurement setup, where a tapered optical fiber tip was put in contact with the suspended portion of a AgNW sitting on the edge of a PDMS substrate. Figure 2.4(b) is the corresponding wave guiding image, where the laser coupled to the optical fiber was turned on, and the wide-field microscope illumination was turned off. The image clearly shows that the coupling efficiency between the fiber and

the nanowire was high enough to allow a high tip emission intensity, even after >40 μm of propagation, as well as low background noise from the junction scattering, both of which are essential for the success of this approach. As shown in Figuress. 2.2(b)–2.2(d), the nanowire tip emission intensity $I$, which was measured by integrating the total counts of the emission spot, was strongly correlated with the SPP propagation distance $x$, which was characterized by the separation between the scattering spot at the nanowire–fiber junction (large red spot on the upper right) and the emission spot at the nanowire tip (small red spot on the lower left). To guarantee the best accuracy (~10 nm) in estimating $x$ from the images, the positions of the nanowire–fiber junction and the nanowire tip in each image were

calculated by fitting each spot to a Gaussian point-spread function, in a method similar to a localization method reported elsewhere [23]. As shown in Figure 2.4(e), for both 658 and 532 nm excitation, the intensity $I$ shows a general decaying trend as $x$ increases owing to the propagation losses in all the SPP modes. Because the oscillations of $I$ originated from the beating of different SPP modes, the oscillation amplitude decreased concurrently with the total intensity. However, the period of oscillation for 658 nm excitation ($\Lambda_{658}$) differs notably from that for 532 nm ($\Lambda_{532}$). This is because Re($\Delta k$), which is inversely proportional to $\Lambda$, varies with the excitation wavelength or photon energy (Figure 2.1(b)). Further studies on the beating pattern reveal that the oscillation period is related to the diameter of the AgNW. Taking 658 nm excitation as an example, when the diameter increases from 160 to 404 nm, the period $\Lambda$ of the intensity envelope peaks increases from 3.67 to 11.30 μm (Figure 2.5(a)). Figure 2.5(b) further confirms that there is an overall monotonic relationship between $\Lambda$ and the nanowire diameter. As stated previously, the periodic patterns can be attributed to constructive and destructive interference between these modes, and the period $\Lambda$ is determined by $\Delta k$ through $\Lambda = 2\pi/\mathrm{Re}(\Delta k)$. Therefore, this monotonic trend can be explained by the variation of the dispersion curves and Re($\Delta k$) with the nanowire diameter, as shown by the COMSOL simulation results in Figure 2.5(c). We found that the momentum intervals ($\Delta k$) between the two participating modes ($H_0$ mode, solid curve; $H_1$ mode, dashed curve) decrease as the diameter of the nanowire increases. The open and solid circles in Figure 2.5(c) are the measured Re($k$) values derived from the oscillation curves in Figure 2.5(a) (the fitting is discussed in detail in the paragraphs below). These measured values agree very well with the simulation results for the

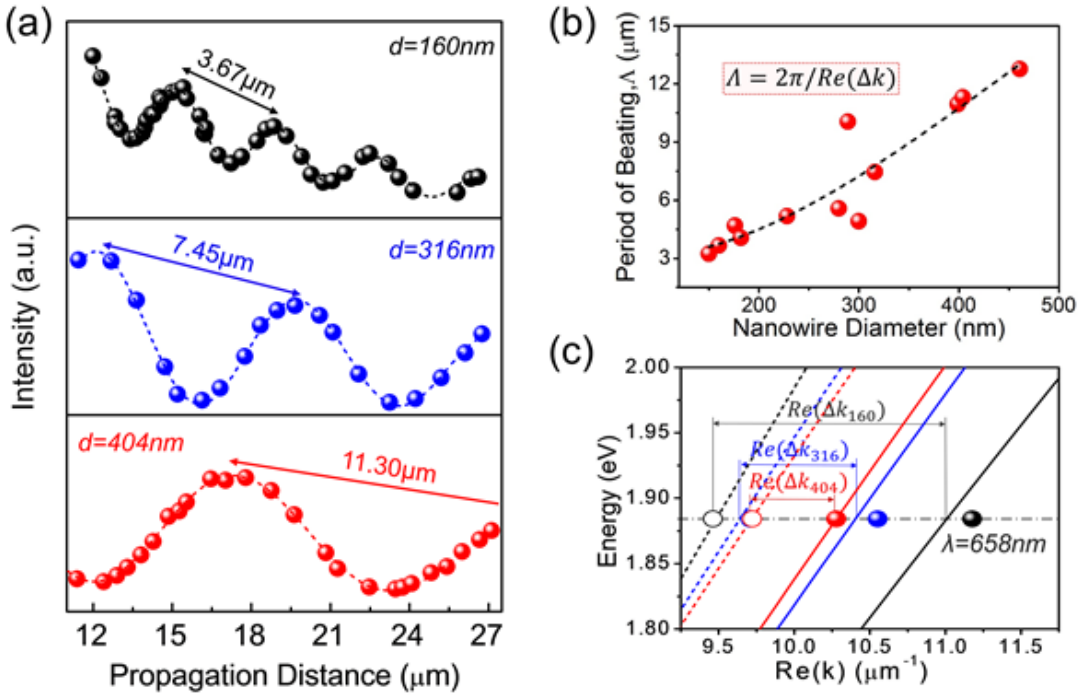


**Figure 2.5** Beating period ($\Lambda$) as a function of AgNW diameter. (a) Measured intensities of the emitted light at the tip of AgNWs with diameters of 160, 316, and 404 nm under 658 nm excitation. (b) Beating periods calculated using the wavevector differences ($\Delta k$) between the two SPP modes as a function of the nanowire diameter. (c) Dispersion curves of $H_0$ (solid curve) and $H_1$ (dashed curve) SPP modes supported by nanowires with diameters of 160 (black), 316 (blue), and 404 nm (red). The open ($H_1$) and solid ($H_0$) circles correspond to measured Re($k$) values derived from (a).

corresponding nanowire diameters at 658 nm. The intensities of the peaks and valleys of the beating patterns are dictated by the sum and difference of the amplitudes of the participating modes ($H_0$ and $H_1$). Because different SPP modes have dissimilar propagation lengths owing to their unique mode profile distributions, the sum and difference of their amplitudes decay at different rates over the propagation distance. Therefore, the beating patterns acquired from the measurements can be used to decouple the SPP modes and derive the corresponding characteristic parameters, including the

effective mode index, propagation length, and mode amplitude. To quantify these parameters for the subwavelength SPP modes, we fitted the experimental beating pattern profiles with a model that includes the exponentially decaying SPP modes and a near-plane-wave free-space mode representing the scattered light from the fiber–nanowire junction [5], which is given by

$$I(x) = \left| \sum_{m=0,1,\ldots} \eta_{\mathrm{H}_m} u_{\mathrm{H}_m} \mathrm{e}^{-\frac{x}{L_{\mathrm{H}_m}}} \mathrm{e}^{-in_{\mathrm{H}_m} k_0 x + i\varphi_m} + u_{\mathrm{sc}} \mathrm{e}^{-in_0 k_0 x + i\varphi_0} \right| \quad (1)$$

where $I(x)$ is the far-field nanowire tip emission intensity as a function of the propagation distance $x$. $\mathrm{H}_m$ represents the participating modes. $\eta_{\mathrm{H}_m}$ is the total collection efficiency (including both the mode emission efficiency and microscopy collection efficiency), $u_{\mathrm{H}_m}$ is the mode amplitude, $L_{\mathrm{H}_m}$ is the propagation length, $n_{\mathrm{H}_m}$ is the effective mode index for mode $\mathrm{H}_m$, and $k_0$ is the wavenumber of the excitation light in free space. $u_{\mathrm{sc}}$ represents the contribution from a free-space photon mode, which is the far-field background originating from the scattering at the fiber–nanowire junction. This model also includes the initial phases ($\varphi_{\mathrm{m}}$ and $\varphi_0$) for each mode, which describe their phase retardations through the mode-coupling process at the fiber–nanowire junction and remain constant throughout the measurements. Note that Eq. (1) considers only the SPPs propagating from the junction toward the free-standing nanowire tip and discounts those reflected by the tip and propagating in the reverse direction, which make no contribution to the scattered light $I(x)$ measured at the nanowire tip. High-order reflections, such as the subsequent reflections from the fiber–nanowire junction toward the free-standing tip, may contribute to $I(x)$, but

the intensity is somewhat attenuated after multiple reflections and long-distance propagation, so they are not considered here. This beating model interprets the interference pattern accurately, as shown by the dashed curves in Figures 2.4(e) and 2.5(a). In Figure 2.5(c), the Re($k$) values of the $H_0$ and $H_1$ modes for the three nanowire diameters (solid and open circles, respectively) were also calculated from the corresponding effective mode indices ( $n_{H_m} = \mathrm{Re}(k_{H_m}) / k_0$ ) extracted from the fitting, which are highly consistent with the simulation, demonstrating the accuracy of the model.

Using this interference model, we could distinguish the propagation parameters of the two supported modes for AgNWs, including the effective mode indices, propagation lengths, and mode amplitudes, for diameters in the range of 150 to 460 nm and two excitation wavelengths (532 and 658 nm). Thinner AgNWs with diameters smaller than 150 nm were not included in this study because thin AgNWs with the long-suspended lengths required for this measurement are highly flexible, and it is difficult to stabilize them against swaying and bending during the measurement to obtain stable readings of $I(x)$.

As shown in Figure 2.6, the measured effective mode indices ($n_{\mathrm{eff}}$) of both modes (orange spheres for $H_1$ and blue spheres for $H_0$) agree reasonably well with the numerical simulation results (orange curve for $H_1$ and blue curve for $H_0$) for all the nanowire diameters tested and both excitation wavelengths. We observed that the effective mode indices of the fundamental ($H_0$) and first-order ($H_1$) modes tend to diverge further as the nanowire diameter decreases for both excitation wavelengths. We also showed that the difference in $n_{\mathrm{eff}}$ between the $H_0$ and $H_1$ modes, which is proportional to Re($\Delta k$) and inversely proportional to the beating period $\Lambda$, is diameter-dependent. In particular, for

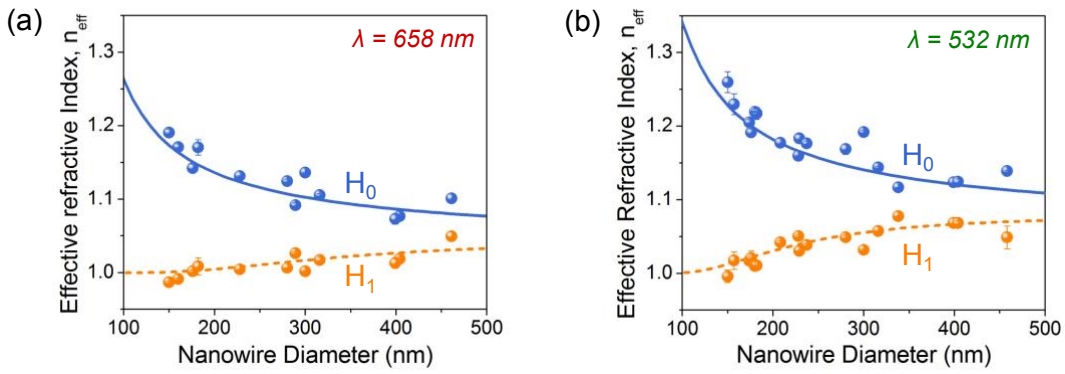


**Figure 2.6** Diameter dependence of effective refractive indices ($n_{eff}$) of the two co-existing SPP modes in AgNWs under (a) 658 nm and (b) 532 nm excitation. Solid and dashed lines represent $n_{eff}$ for the two modes calculated from numerical simulations.

nanowires 160 nm in diameter, $\Delta n_{eff}$ is greater for 532 nm excitation than for 658 nm excitation, suggesting that $\Lambda_{532}$ is smaller than $\Lambda_{658}$, in agreement with the trend observed in Figure 2.6(e). In addition, Figure 2.6 also shows that for the fundamental ($H_0$) mode, there is no cutoff diameter for either wavelength.

The interference model can be used to decouple the SPP modes and evaluate their propagation losses separately. Figure 2.7 shows the dependence of the propagation length $L$ extracted from the fitting on the nanowire diameter for the $H_0$ and $H_1$ modes. For the fundamental mode, $L_{H0}$ is either consistent with or even slightly better than that calculated from the numerical simulation for the 658 or 532 nm measurements, respectively. The numerical simulation presented here uses the permittivity measured on a polycrystalline thin film (see Methods for details) and a physical model of the nanowire with perfectly flat side walls and no surface roughness. Our measured results reflect a considerable reduction in and perhaps even the absence of scattering loss due to surface roughness and domain boundaries in the chemically synthesized nanowires. The propagation lengths of the $H_1$

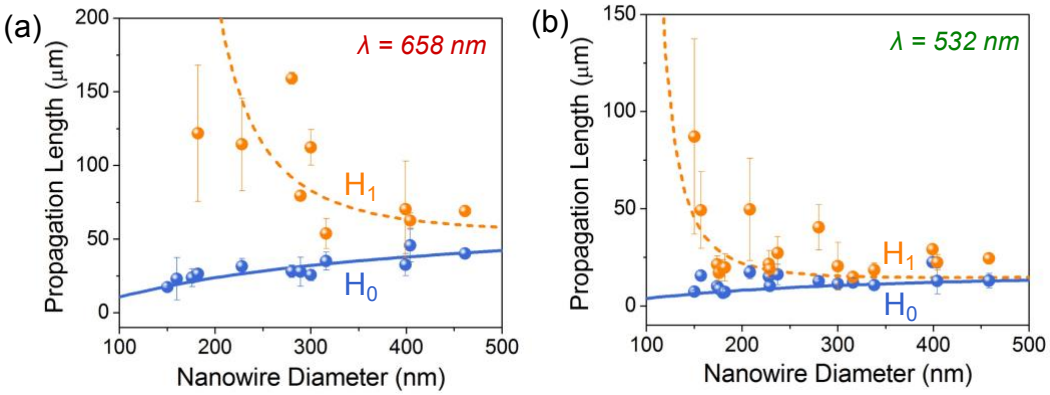


**Figure 2.7** Diameter dependence of propagation length of the two co-existing SPP modes in AgNWs under (a) 658 nm and (b) 532 nm excitation. Solid and dashed lines represent $n_{\text{eff}}$ for the two modes calculated from numerical simulations.

mode align with the simulation results overall. However, they exhibit significant deviations and large uncertainties, in particular for small-diameter AgNWs. As mentioned for the reliability test of our mode analysis method (see more details in the Supporting Information), the reason is that the AgNWs in the experiments were not long enough to support analysis of such long propagation lengths for the $H_1$ mode. For large-diameter nanowires, the propagation lengths are within the range of the nanowire length, and the method provides precise measurements with small deviations.

## 2.6. Calculation of weight of two lowest order modes.

### 2.6.1. Calibration of the mode coupling efficiency

The data fitting using Equation (1) can retrieve the values of the product of the total collection efficiency $\eta_{Hm}$ and the mode amplitude $u_{Hm}$, but cannot decouple these two variables. The total collection efficiency $\eta_{Hm}$ include two parts: (1) the emission efficiency

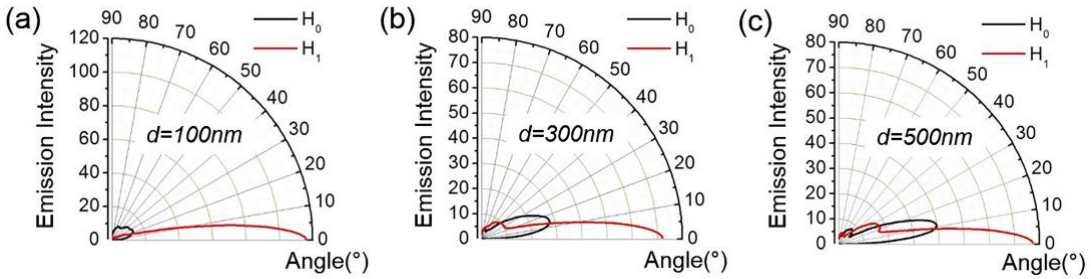


**Figure 2.8.** The far-field radiation patterns in power, coupled from the $H_0$ and $H_1$ modes. The excitation wavelength is 532 nm.

at the nanowire end, where the propagating surface plasmon is coupled into free space wave; and (2) the collection efficiency of the long-working-distance objective lens.

### 2.6.2. Far-field radiation pattern of a nanowire tip

Since the momentum of SPP modes is always larger than that of the free-space light and generate a momentum mismatch, the SPPs cannot be coupled into the free-space mode when they are propagating along the nanowire. However, the crystal facets at the nanowire tip can act as a scatterer to provide a broad range of momentums to compensate this mismatch, leading to the mode-dependent far-field radiation patterns, as shown in Figure 2.8. In general, the $H_1$ mode has higher transmission than the $H_0$ mode for all nanowire diameters, because of the smaller momentum mismatch between the $H_1$ mode and free-space mode. In particular, thin nanowires have $n_{eff}$ close to 1 for $H_1$ and the highest $n_{eff}$ for $H_0$, which leads to the near-unity transmission for $H_1$ mode but low transmission for $H_0$ (Figure 2.9b).

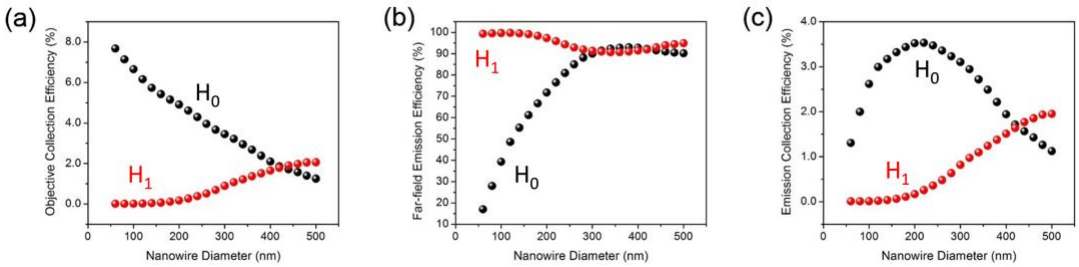


**Figure 2.9. (a)** The collection efficiencies of the objective lens (NA=0.5) for different modes. **(b)** The coupling efficiency (mode transmission) from SPP to free space wave. **(c)** The total collection efficiency $\eta_{Hm}$ for different diameters.

### 2.6.3. Objective lens collection efficiency:

In order to have enough space for the operation of the micromanipulator, a long-working-distance objective lens with a moderate NA (0.5) was used in our experiment. Since the nanowire has to lie in the image plane during the measurement, a significant portion of the emitted light propagates horizontally and cannot be collected by the lens placed above the nanowire. Figure 2.9a shows the collection efficiencies of the objective lens for different modes, which were calculated by integrating the emission power in the cone volume created by the objective lens and normalized by the total radiated power. Since the $H_0$ mode has a larger radiation angle (Figure 2.8), its collection efficiency is, in general, higher than the $H_0$ mode for small nanowire diameters. By multiplying the objective collection efficiency (Figure 2.9a) to the far-field radiation power efficiency (Figure 2.9b), the emission efficiency $\eta_{Hm}$ can be achieved.

Now, considering the collection efficiency, the nominal power ($\left|\eta_{\mathrm{H}_m} u_{\mathrm{H}_m}\right|^2$) of the participating SPP modes can also be derived by fitting Eq. (1). The measured power ratio of the two modes under 658 nm excitation is plotted in Figure 2.10 as a function of the

nanowire diameter. The result shows that the $H_0$ mode is dominant for thin AgNWs (with a diameter smaller than 300 nm), whereas the $H_1$ mode is dominant for thicker AgNWs.

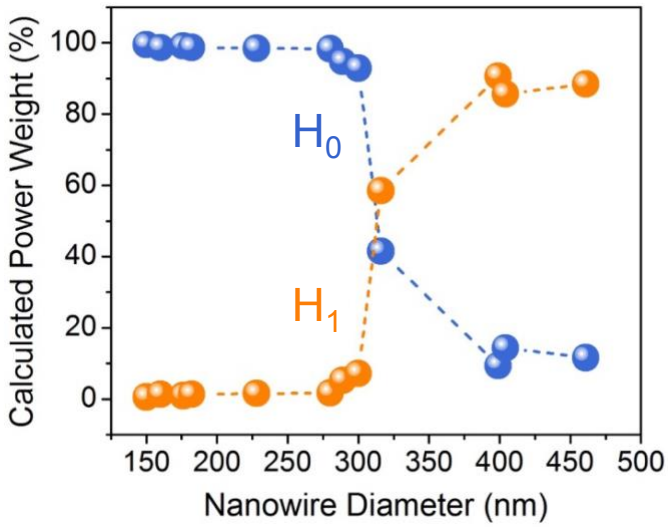


**Figure 2.10** Relative weight of $H_0$ and $H_1$ modes as a function of NW diameter (658 nm excitation).

This selective excitation of SPP modes can be explained by the mode coupling process at the fiber–nanowire junction: A thin nanowire has a compact symmetrical $H_0$ mode that couples efficiently with the uneven component of the evanescent field of a dielectric fiber; on the other hand, the asymmetrical $H_1$ mode is excited by the even component of the evanescent field, which is less efficient in thin nanowires, where the $H_1$ mode is less confined and more widely distributed (more details are available in the ESM).

The coupling efficiency between the tapered optical fiber and an AgNW is confirmed by COMSOL simulation. Figure 2.8 shows the model configuration for the simulation. The taper angle of the optical fiber ($\theta$) and coupling angle between AgNW and optical fiber

($\phi$) were 14 ° and 15 ° respectively. 3.5 μm long AgNW with 3 μm propagation distance was

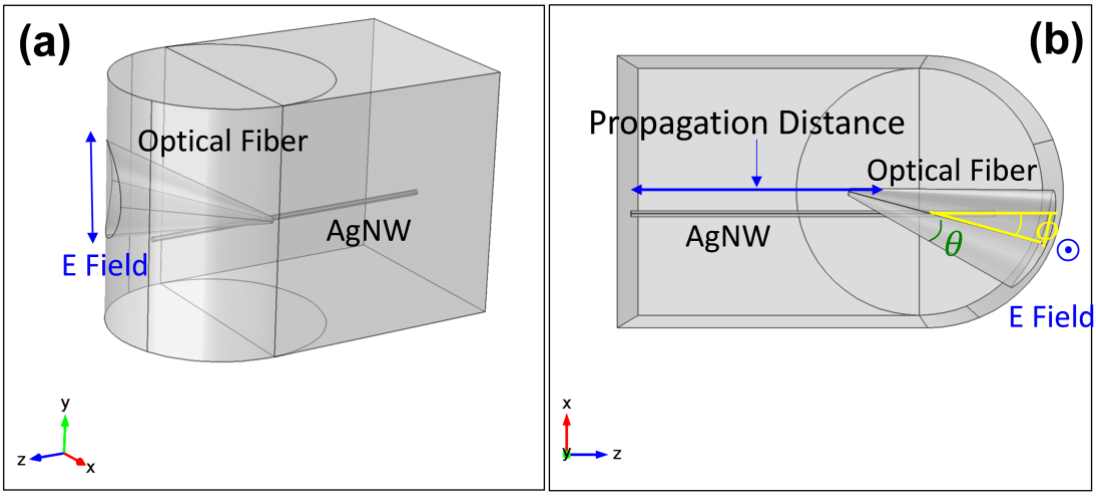


**Figure 2.11.** The side view **(a)** and top **(b)** view of the 3-D geometry used for calculating the amplitudes of the PSP modes in AgNW. The electric field of the incident light in the optical fiber is set to be y direction, to compare with the experimental results.

used and its diameter was changed from 100 nm to 500 nm. The square root of the energy flux, which was calculated by integrating the Poynting vector over the mode cross section at the tip of the AgNW, was used to calculate the amplitude of each mode in the AgNW. In order to compensate the propagation losses of each mode along the propagation distance, the intensity was multiplied by $\frac{1}{e^{-3/L}}$ where L is the propagation length of the two lowest modes.

Figure 2.12 shows the comparison between the simulated result and the experiment result, which confirms the trend that $H_1$ mode is easier to be excited in narrow nanowires than the $H_0$ mode. This trend can be used to guide the design of plasmonic devices where specific modes are needed.

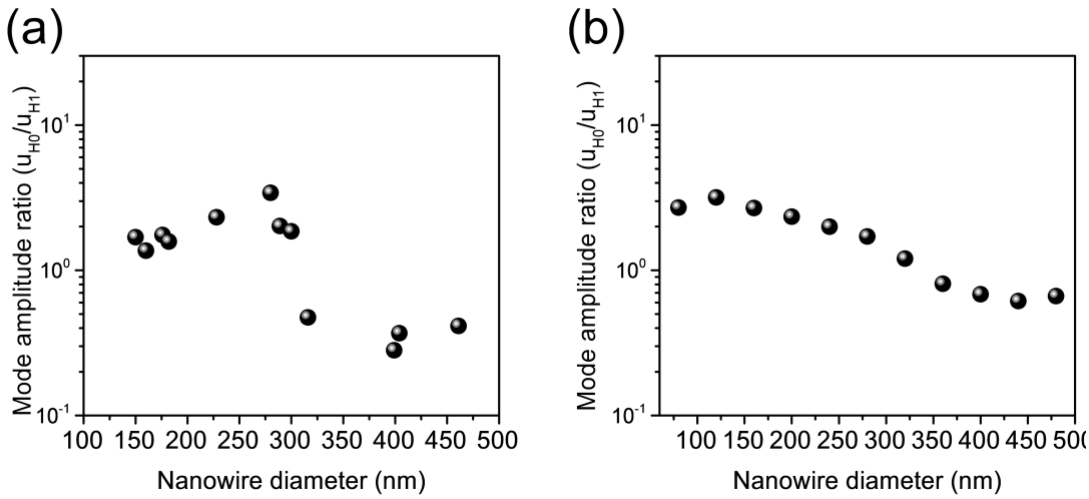


**Figure 2.12. (a)** The extracted mode amplitude from the experiment. **(b)** The simulated results from the model in Figure 2.9.

## 2.7. Conclusion

We demonstrated a new method of decoupling and analyzing SPP modes in a plasmonic waveguide. This method, unlike other techniques, can be used to excite SPPs at an arbitrary position on a AgNW by putting the tip of a tapered optical fiber into physical contact with the NW, which breaks the local symmetry and provides the additional momentum needed to excite the SPP modes in the NW. This also enables monitoring of the emission intensity at the NW tip while gradually changing the propagation distance by moving the fiber tip along the NW. The small scattering loss at the tapered fiber tip and the high coupling efficiency make it possible to observe the interference pattern between the two SPP modes simultaneously excited in the NW. This, in turn, enables analysis of the propagation properties of each individual mode, including the mode indices, propagation lengths, and

relative weights of co-existing modes. The experimental results agree well overall with numerical simulations using dielectric constants measured from polycrystalline Ag films, but show improved propagation lengths owing to the reduced propagation loss originating from the high crystallinity and smooth surfaces of the chemically synthesized AgNWs. The results also show that the propagation parameters, in particular the mode amplitude, are strongly correlated with the nanowire diameter, and different SPP modes can be selectively excited by controlling the nanowire diameter. To the best of our knowledge, this is the first report in which co-existing SPP modes in a plasmonic nanowire waveguide are decoupled and analyzed separately. This new mode analysis technique can be applied to many other metal nanowire waveguides and provides unique insights into the development and optimization of SPP-based applications, including surface-enhanced Raman scattering platforms and nanophotonic devices.

## 2.8. References


1. Guo, X.; Qiu, M.; Bao, J.; Wiley, B. J.; Yang, Q.; Zhang, X.; Ma, Y.; Yu, H.; Tong, L., Direct Coupling of Plasmonic and Photonic Nanowires for Hybrid Nanophotonic Components and Circuits. *Nano Lett* **2009,** *9* (12), 4515-4519.

2. Yan, R. X.; Pausauskie, P.; Huang, J. X.; Yang, P. D., Direct photonic-plasmonic coupling and routing in single nanowires. *P Natl Acad Sci USA* **2009,** *106* (50), 21045-21050.

3. Wei, H.; Li, Z. P.; Tian, X. R.; Wang, Z. X.; Cong, F. Z.; Liu, N.; Zhang, S. P.; Nordlander, P.; Halas, N. J.; Xu, H. X., Quantum Dot-Based Local Field Imaging Reveals Plasmon-Based Interferometric Logic in Silver Nanowire Networks. *Nano Lett* **2011,** *11* (2), 471-475.

4. Xining, Z.; Zhe, M.; Rui, L.; Ying, G.; Chao, M.; Xiaoqin, W.; Qihuang, G.; Limin, T., Single-nanowire surface plasmon gratings. *Nanotechnology* **2012,** *23* (22), 225202.

5. de Leon, N. P.; Shields, B. J.; Yu, C. L.; Englund, D. E.; Akimov, A. V.; Lukin, M. D.; Park, H., Tailoring Light-Matter Interaction with a Nanoscale Plasmon Resonator. *Physical Review Letters* **2012,** *108* (22), 226803.

6. Wu, X.; Xiao, Y.; Meng, C.; Zhang, X.; Yu, S.; Wang, Y.; Yang, C.; Guo, X.; Ning, C. Z.; Tong, L., Hybrid Photon-Plasmon Nanowire Lasers. *Nano Lett* **2013,** *13* (11), 5654-5659.

7. Yang, Z.; Wang, M.; Song, X.; Yan, G.; Ding, Y.; Bai, J., High-performance ZnO/Ag Nanowire/ZnO composite film UV photodetectors with large area and low operating voltage. *Journal of Materials Chemistry C* **2014,** *2* (21), 4312-4319.

8. Zhan, Y.; Li, X.; Wu, K.; Wu, S.; Deng, J., Coaxial Ag/ZnO/Ag nanowire for highly sensitive hot-electron photodetection. *Appl Phys Lett* **2015,** *106* (8), 081109.

9. Ditlbacher, H.; Hohenau, A.; Wagner, D.; Kreibig, U.; Rogers, M.; Hofer, F.; Aussenegg, F. R.; Krenn, J. R., Silver Nanowires as Surface Plasmon Resonators. *Physical Review Letters* **2005,** *95* (25), 257403.

10. Sanders, A. W.; Routenberg, D. A.; Wiley, B. J.; Xia, Y. N.; Dufresne, E. R.; Reed, M. A., Observation of plasmon propagation, redirection, and fan-out in silver nanowires. *Nano Lett* **2006,** *6* (8), 1822-1826.

11. Pyayt, A. L.; Wiley, B.; Xia, Y.; Chen, A.; Dalton, L., Integration of photonic and silver nanowire plasmonic waveguides. *Nat Nano* **2008,** *3* (11), 660-665.

12. Wild, B.; Cao, L.; Sun, Y.; Khanal, B. P.; Zubarev, E. R.; Gray, S. K.; Scherer, N. F.; Pelton, M., Propagation Lengths and Group Velocities of Plasmons in Chemically Synthesized Gold and Silver Nanowires. *Acs Nano* **2012,** *6* (1), 472-482.

13. Shegai, T.; Huang, Y.; Xu, H.; Käll, M., Coloring fluorescence emission with silver nanowires. *Applied Physics Letters* **2010,** *96* (10), 103114.

14. Ma, Y.; Li, X.; Yu, H.; Tong, L.; Gu, Y.; Gong, Q., Direct measurement of propagation losses in silver nanowires. *Optics letters* **2010,** *35* (8), 1160-1162.

15. Wang, W.; Yang, Q.; Fan, F.; Xu, H.; Wang, Z. L., Light propagation in curved silver nanowire plasmonic waveguides. *Nano letters* **2011,** *11* (4), 1603-1608.

16. Guo, X.; Ma, Y.; Wang, Y.; Tong, L., Nanowire plasmonic waveguides, circuits and devices. *Laser & Photonics Reviews* **2013,** *7* (6), 855-881.

17. Sun, Y.; Yin, Y.; Mayers, B. T.; Herricks, T.; Xia, Y., Uniform silver nanowires synthesis by reducing AgNO3 with ethylene glycol in the presence of seeds and poly (vinyl pyrrolidone). *Chemistry of Materials* **2002,** *14* (11), 4736-4745.

18. Korte, K. E.; Skrabalak, S. E.; Xia, Y., Rapid synthesis of silver nanowires through a CuCl- or CuCl2-mediated polyol process. *Journal of Materials Chemistry* **2008,** *18* (4), 437-441.

19. Johnson, P. B.; Christy, R. W., Optical Constants of the Noble Metals. *Physical Review B* **1972,** *6* (12), 4370-4379.

# Chapter 3

# Nanowire waveguide for label-free quantitative sensing of intracellular biomolecules in single living cell

## 3.1. Nanowire waveguide for single living cell endoscopy

Complex inter-reactions among ions, biopolymers and metabolites run living systems and any abnormal cellular processes driven by those biomolecules are closely linked to the origins of human disease. However, any changes of the environs to characterize the biomolecules will vary their intrinsic properties and many of them even cannot be observed after purification or isolation for the characterization[1]. Hence, analysis of biological molecules in living cells with minimal perturbations is essential to gain insights into cell functions, cellular signaling pathways, and gene expression inside single cells, and disease mechanisms. One-dimensional nanostructures, such as glass pipettes, dielectric nanowires, nanotubes, and even photonic crystal waveguides, have been demonstrated as promising platforms of living-cell endoscopy probes for gene or drugs delivery with a temporal resolution because its small diameter enables the insertion of the probe without serious damage to the cell. Furthermore, this nanostructure can be used not only for the delivery of the payloads but also intracellular bio-sensing. The delivery of the payloads have been accomplished by many groups using diverse nanotubes and wires such as carbon nanotubes[2], boron nitride nanotubes[3], silicon nanowires[4], and tin oxide nanowires[5]. On the other hand, chemical/biological sensing inside of a living cell is more sophisticated because

high specificity and sensitivity to trace amounts of target molecule in highly complex chemical/biological environments are required.

Recently, Surface-enhanced Raman Spectroscopy (SERS) has proven to be capable of sensing chemical/biological molecules in living cells by overcoming the extremely low possibility of occurrence of Raman scattering due to strong electromagnetic fields confinement near metal surface[6]. SERS has remarkable advantages of photostability, label-free detection, and multiplex detection capability due to the highly resolved spectra over fluorescence-based analytical assays, indispensable tools for the modern-day cell biologists[7-8], which suffer from photobleaching, fluorescence self-quenching, and disruption of normal cellular processes due to fluorophores. In the early days, CNTs decorated with Au nanoparticles (NPs) were used as a label-free SERS intracellular probe[9-10]. Spectral information of the intracellular fluid could be obtained by locating the probe inserted in a living cell in the center of focused laser beam. Au NP surfaces and small gaps between Au NPs could confine strong electromagnetic fields and boost the intensity of Raman scattering. However, their excitation of Raman using free space light focused by an objective lens has a high possibility to damage the membranes and/or other cell components of living cells.

Remote-excitation using dielectric nanowire (NW) waveguides such as $SnO_2$[5] and polycaprolactone[11] has been demonstrated for the inclusion of nanometer-sized internal light source into a target subcellular region without interfering with or perturbing the outer cell membrane. However, these dielectric waveguides are still limited by diffraction[12], so that the excitation to high-energy, short- wavelength lasers and further scaling down of the

device for long-term monitoring are restricted. On the contrary, metallic or plasmonic NWs offer a means to go below this size limit as they transfer optical signals via surface plasmon polaritons (SPPs). Lu et al. has demonstrated live-cell SERS endoscopy using a silver nanowire (AgNW) waveguide[13]. In their work, remotely excited SERS spectra was measured in the cell nucleus by focusing the laser on an Ag NP that was randomly attached to the side of an Ag NW. However, due to the complexity of the subcellular chemistry, these native SERS spectra were poorly resolved to render truly insightful chemical information, not to mention molecular-specificity or quantitative analysis. In addition, the tip of an Ag NW is a poor SERS cavity, which greatly limits the sensitivity of this technique. Moreover, the optical coupling through NP has an excitation efficiency below 1%, which limits the photon flux deliverable into the cell and further restricts the SERS sensitivity.

In this work, we have developed a novel intracellular sensing probe by integrating a plasmonic NW probe with high-sensitivity SERS antennas functionalized with molecular-specific Raman markers. A chemically synthesized AgNW has been used to deliver light beyond the diffraction limit with a low propagation loss due to its intrinsic properties such as atomically smooth surface and lowest ohmic loss. Excitation laser was guided through the optical fiber to the AgNW with a high coupling efficiency and therefore, any perturbance or damage to the living cell caused by the scattering loss could have been minimized. Ag nanocubes (NCs) were integrated to the tip of the plasmonic NW probe via a repeatable and reliable preparation method not only for local field enhancement for high sensitivity but also as an antenna for the emission of the Raman signal to the free space for

a higher collection efficiency. On this platform, different SERS markers can be integrated on different nano-antennas separately and co-assembled on the nanoprobe for molecular specificity, quantitative analysis, and multiplexed intracellular sensing which have been difficult to demonstrate in many other groups. In order to demonstrate the feasibility of molecular specific quantitate analysis of biomolecules in single living cell, we measured the pH values in a living Hela cell for the first time using enhanced Raman scattering excited by a biocompatible and non-invasive waveguide probe. The schematic detailing Raman scattering inside of a living cell using our antenna coupled plasmonic nanowire endoscopy (ACPNE) probe is illustrated in **Figure 3.1**.

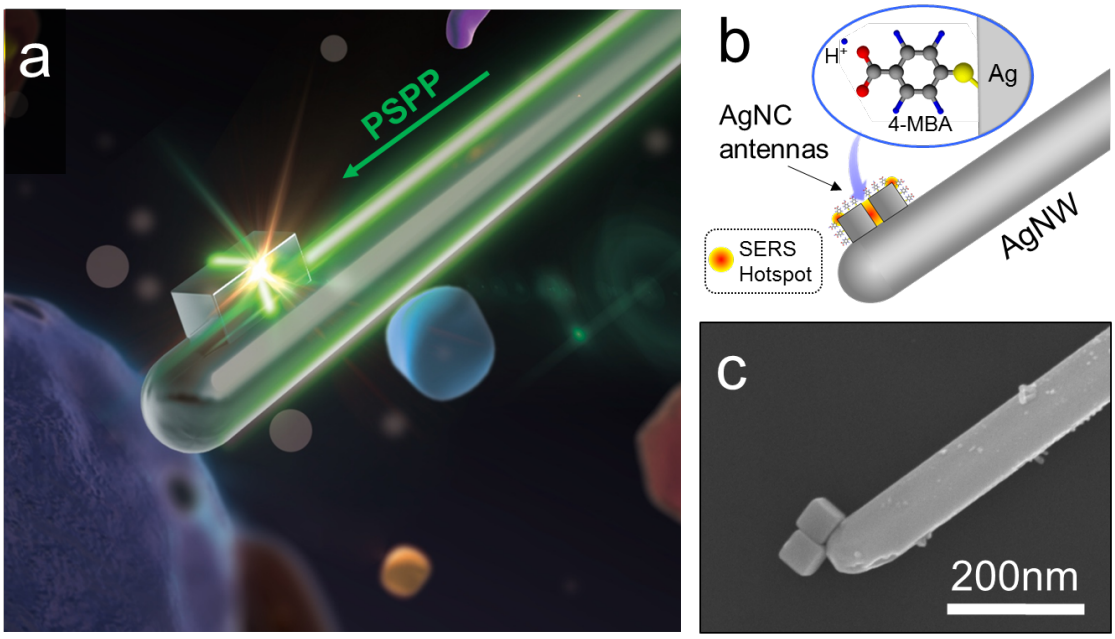


**Figure 3.1.** (a) Schematic illustration of the *in situ* remote sensing in single live-cells with an APN endoscope. (b) Schematic of the structure of an APN endoscope, which is prepared by coupling a AgNW plasmonic nanowire waveguide that delivers light remotely with AgNC antennas to create localized SERS hot spots. The AgNC antennas are functionalized with a pH responsive molecule (4-MBA). (c) SEM image of an APN endoscope.

## 3.2. Materials and Methods

### 3.2.1. Tapering optical fiber

A single mode optical fiber (Thorlabs, S405-XP) was chemically etched in 48% hydrofluoric acid (HF, Fisher-Scientific). Prior to etching the optical fiber, the jacket at the end of the fiber was removed and washed with acetone and DI water. The fibers were immersed in HF covered with isooctane (Fisher-Scientific) and pulled out of the etching solution using a syringe pump[14]. The syringe pump was used to make the optical fiber tip sharper. The fibers then washed with DI water several times.

### 3.2.2. AgNC synthesis

AgNCs shown in Figure 3.2 (a) were synthesized using a polyol process[15]. First, 10ml of 0.06 M $AgNO_3$ including 20µl of 60 mM $CuCl_2$ in 1,5-pentanediol (PD) was prepared in a 20ml glass vial. In another vial, 10ml of 0.18 M of Polyvinylpyrrolidone in repeating unit (PVP, Mw ≈ 55 000) was prepared. 100ml round bottom flask with 20ml of PD under magnetic stirring was then immersed in a silicon oil bath preheated at 190°C. While the PD in the flask was being heated, 1ml of the $AgNO_3$ precursor was placed in ice bath. After 15mins, the 500µl of the cold $AgNO_3$ precursor was suddenly injected to the flask followed by the injection of 250 µl of PVP precursor dropwise. Afterwards, the room temperature $AgNO_3$ and PVP precursors were injected alternately into the flask at a rate of 500 µl /min and 250 µl/30s. After the color of the solution turned red-green, the flask was taken out from the oil bath and cooled down in air for 15mins. Pure AgNCs were obtained by centrifugation with ethanol at 9000rpm for 40mins five times. All the chemicals were purchased from Sigma Aldrich except PD which was purchased from Fisher-Scientific.

### 3.2.3. AgNW synthesis

In the same manner with AgNC, a polyol process was used to synthesize AgNWs[16]. Five milliliters of ethylene glycol (EG) in a 50ml pear shape flask was immersed in a silicon oil bath at 152 °C for 15 mins under magnetic stirring at 400rpm. Then, 40 µl of 4 mM $CuCl_2$ was injected and the solution was heated for additional 15 mins. 125 µl of 0.147 M PVP in repeating unit and 0.094M $AgNO_3$ precursors were injected alternately into the flask every minute until all the all the solutions were consumed. The AgNWs were purified by centrifugation with ethanol at 2000rpm for 20mins 5 times after allowing 15mins to cool down the nanowire solution. EG was purchased from Fisher-Scientific, All the other chemicals used here were the same ones used for AgNC synthesis.

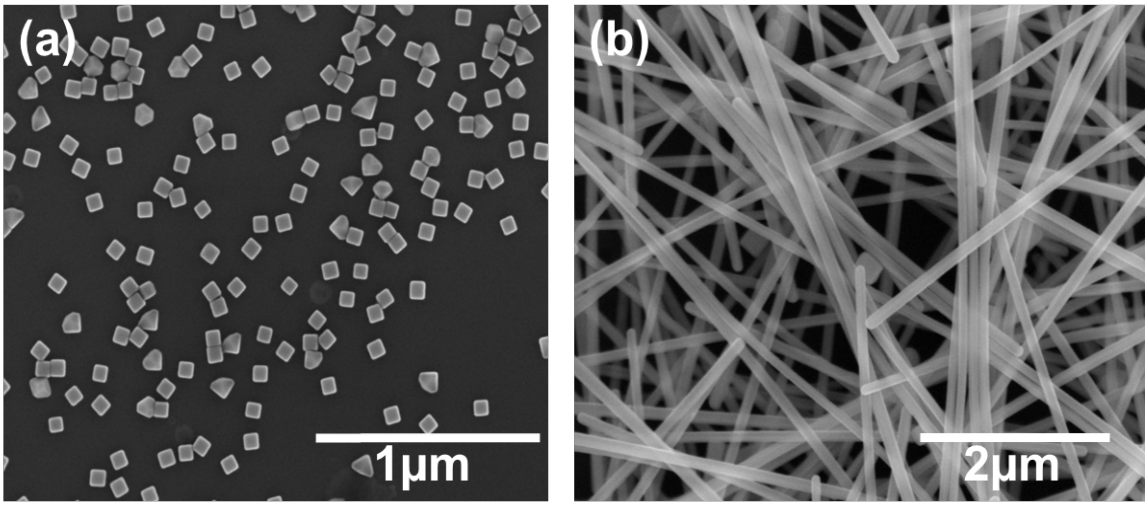


**Figure 3.2**. SEM images of the AgNCs(a) and AgNWs(b) used for the fabrication of an ACPNE probe.

### 3.3. Development of precise and repeatable attachment of AgNCs to the tip of AgNW.

It has been reported that an endoscopy probe with 250 nm in diameter does not damage the cell during the insertion of the probe[17]. Therefore, AgNC and AgNW were prepared with the aim that the diameter of the plasmonic AgNW probe including AgNC monolayer on it does not exceed 250 nm. The diameters of AgNCs and AgNWs prepared in this work ranged from 50 to 60 nm and from 120nm to 180nm respectively. Precise control of number of AgNCs and their locations are notably important not only for the confinement of a strong electric field but also for minimal damage to the cell membrane during insertion and efficient Raman signal collection due to a small focal spot. The small focal spot leads to being capable of using a higher numberical aperture (N/A) which end up with a higher signal collection efficiency through the objective lens.

For the fine control over the number of AgNCs and their locations, we developed a novel method with consistent repeatability to attach a few AgNCs near the tip of a AgNW by benefiting the coffee ring effect which is a troublesome phenomenon occurring in printing. In this method, we first coupled a AgNW to the tip of a tapered optical fiber and glued it with a rapid-setting epoxy. After that, AgNCs functionalized with self-assembly monolayers (SAMs) as Raman indicators in ethanol was added to a drop of water on PDMS. Here, we used 4-aminothiophenol (4-ATP) and 4-mercaptobezoic acid (4-MBA) as the Raman indicators. AgNCs aggregated on the interface between air and water + ethanol near the PDMS substrate could be observed as shown in **Figure 3.3**.

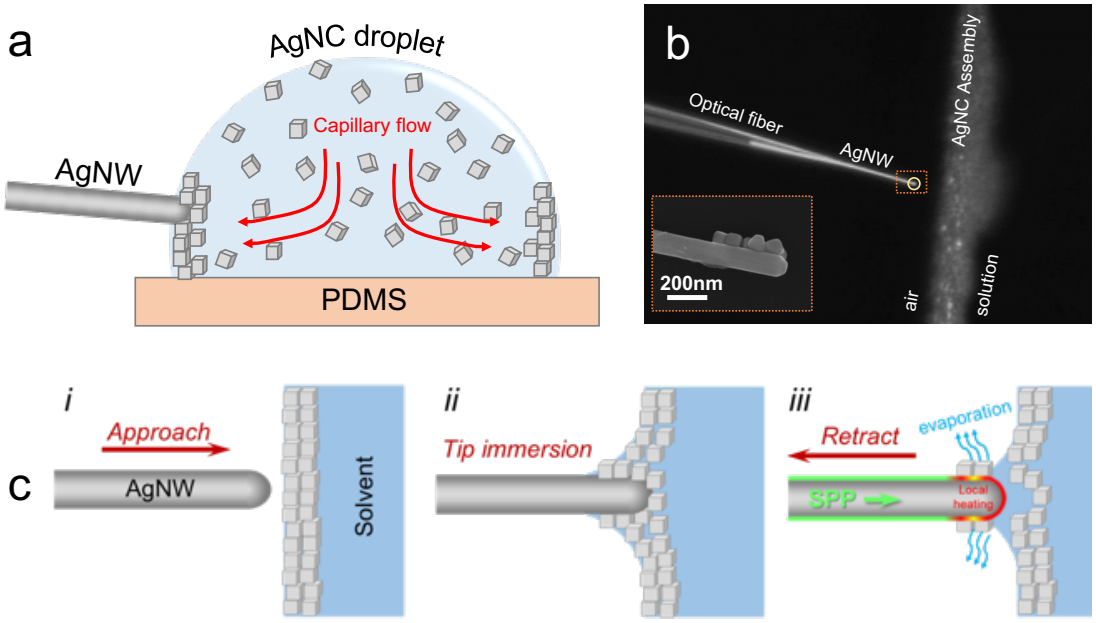


**Figure 3.3.** Chemical-linker-free fabrication of the APN endoscope. **(a),** Schematic illustration fabrication set-up. **(b),** Optical microscope image (top-view) of the fabrication set-up. Inset on the lower left (dashed orange box) is the SEM image of the tip of the APN endoscope showing AgNCs attached to the tip of the AgNW. Insets on the right are optical images of the emission pattern at the AgNW tip obtained before (top) and after (bottom) the attachment of AgNCs. **(c),** Schematic illustration describing the mechanism of the chemical-linker-free attachment of AgNCs to the tip of the AgNW. (i)

The aggregation of AgNCs appears only in water or water-ethanol mixture but not in pure ethanol (**Figure 3.4**). This phenomenon results mainly from capillary flow due to the different evaporation rate across the surface of drop while the drop is being dried and its contact line is pinned[18]. Water on the edge has a higher evaporation flux than that on the top because the water molecules on the interface near the edge have a large contact area with air. Therefore, outward flow occurring in the droplet drags the dispersed particles towards the pinned contact line. This coffee ring effect is prevailing especially in water because Marangoni stress, recirculating flow driven by temperature gradient, is significantly suppressed due to surfactant contaminants[19-20]. Ethanol, on the contrary, has

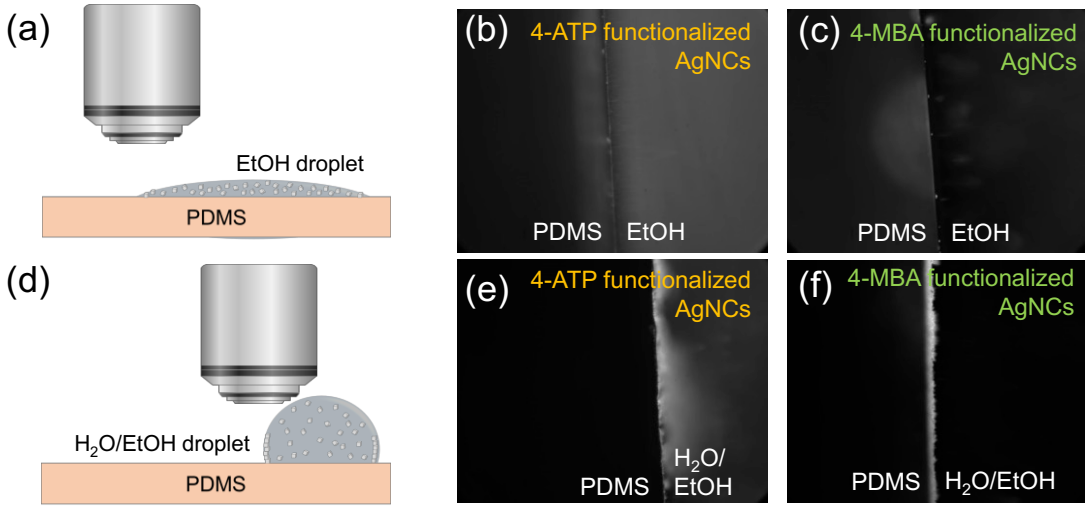


**Figure 3.4.** AgNC self-assembly at the PDMS-liquid–air interface. **(a),** A schematic illustration of an ethanol droplet containing AgNCs on a PDMS substrate. **(b-c),** Dark field optical images of the PDMS-liquid-air interface of an ethanol droplet containing AgNCs functionalized with 4-ATP **(b)** and 4-MBA **(c)**. In both cases, the AgNC aggregation at the interface is not obvious due to the low surface tension of the solvent. **(d),** A schematic illustration of a mixed solvent (50% $H_2O$ in EtOH) droplet containing AgNCs on a PDMS substrate. **(b-c),** Dark field optical images of the PDMS-liquid-air interface of a mixed solvent (50% $H_2O$ in EtOH) droplet containing AgNCs functionalized with 4-ATP **(e)** and 4-MBA **(f)**. and air/ethanol+water/PDMS (e and f). **(d-f),** The schematic and dark field optical images of the PDMS-$H_2O$/ethanol-air interface.

a low contact angle with PDMS. Thus, the capillary flow in ethanol will not be as fast as that in water due to the small deviation of the evaporation flux between top and edge of the drop. Not severe but still considerable Marangoni flow in ethanol will also continuously moves the particles back toward the droplet center.

We approached and immersed only the tip of a AgNW coupled to a tapered optical fiber in the AgNC aggregated area using a triple-axis manipulator. When a AgNW tip touches the surface of the AgNC suspension solution, the solution including some AgNCs climbs up along the AgNW due to the hydrophilic surface of the AgNW. Other than attachment of

AgNCs from the solid substrate, a low binding energy between AgNCs and flexible movement of the AgNC aggregates in the solution allow the attachment of the AgNCs without any physical damage to the AgNW. By anchoring the AgNCs in Brownian motion to the PDMS substrate, the concentration of AgNCs used for the attachment could have been maintained nearly same regardless of the AgNC suspension density or vaporization of the solution during the attachment process because we only use the outermost AgNCs of the aggregates on the boundary.

The target molecule indicators in our probe are located only on the surface of AgNCs so that Raman spectra of the indicators represent the concentration of the target molecules only near the AgNCs. We consistently could have achieved attachment of a few AgNCs within the range of 500nm from the AgNW tip using this method demonstrating that the detection volume of our optical sensor is femtoliter-scale.

In the process of AgNC attachment, we also sent a laser through the optical fiber to the tip of the AgNW to accelerate the evaporation of the solution due to the laser induced heating near the AgNW tip while pulling the AgNW out (**Figure 3.4c**). Here, there is the reason for the usage of ethanol-water binary mixture rather than pure water for the attachment of AgNCs. The ethanol-water binary mixture has a lower surface energy than pure water has. Therefore, the vapor pressure of the mixture is also lower than pure water. Heat induced by the laser can accelerate the evaporation of the solution and facilitate the attachment of AgNCs to the tip of AgNW. Sudden change of the radiation pattern at the tip of AgNW can be exploited for the indication of the attachment of AgNCs. **Figure 3.5b(ii)** shows that a new scattering spot appears at the upper part of the circular radiation pattern which did

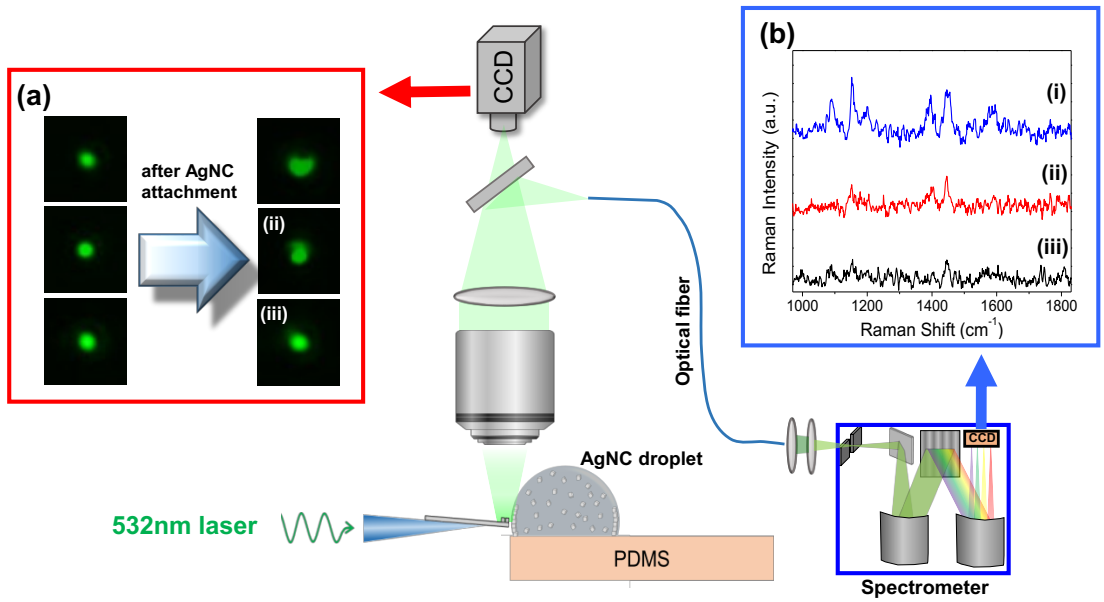


**Figure 3.5.** Schematic illustration of in situ, instant and simultaneous verification of AgNC attachment at the tip of a AgNW. (a), Optical images of the emission pattern at the tip of AgNW before and after attachment of AgNCs. (b), Measured Raman spectra of SAM on AgNCs attached to the tip of AgNW corresponding to the emission pattern changes in (a).

not exist prior to the immersion. The change of radiation pattern at the tip of AgNW is usually observed within immersing it 5 times. The radiation pattern changes enable us not only to confirm the attachment of AgNCs but also to estimate the number of AgNC qualitatively and their location at the tip of AgNW with instant Raman scattering measurement (**Figure 3.5**). As a target molecule for Raman spectroscopy, we functionalized AgNCs with 4-ATP prior to the attachment of AgNCs at the tip of a AgNW. A weak laser output power lower than 3μW was used to avoid any laser-induced melting of AgNCs. Therefore, the signal intensity is not high enough to see all distinct peaks of 4-ATP but it is clear enough to confirm the attachment of AgNCs and obvious that the signal intensity is proportional to the number of AgNCs. This laser power can be increased up to

around 10 μW in air and even higher value than 50 μW in a liquid solution that has a high heat capacity such as water. Clear and strong Raman spectrum with a higher laser output power in air and water were shown in **Figure 3.6**. Those in situ measurements of radiation pattern and Raman scattering can be achieved simultaneously and instantly after the attachment of AgNCs which lead to an increase in the reliability of the probe fabrication significantly.

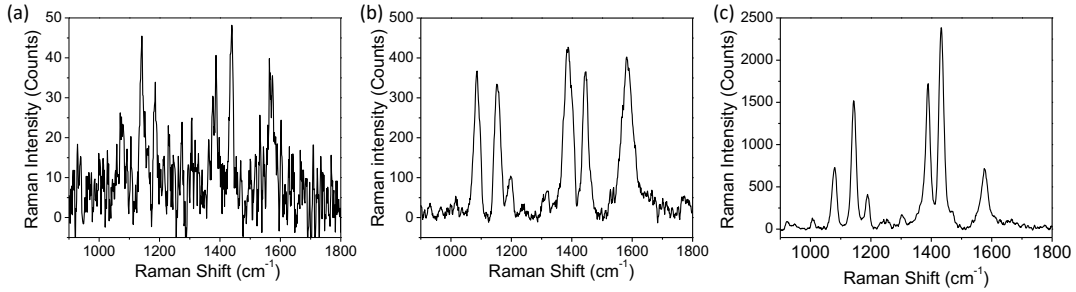


**Figure 3.6.** Raman spectra of 4-ATP SAM on AgNCs at the tip of AgNW. (a) Measured spectrum in air with a minimum laser output power of <3;16to confirm the AgNCs attachment at the tip of AgNW and (b) a maximum laser output power of ~10μW that the AgNCs can withstand without melting. (c) Measured spectrum in water with a laser output power of >50μW.

## 3.4. Enhancement of Raman scattering intensity by integration of AgNCs to AgNW.

**Figure 3.7** compares the Raman scattering of 4-MBA obtained using a AgNW probe with and without AgNCs on the surface, where a SAM of 4-MBA was coated on the surface of the AgNCs and AgNWs as a Raman indicator. Despite the large number of 4-MBA molecules on the surface of the AgNW relative to the surface of the AgNCs due to its larger surface area, the Raman scattering intensity from the AgNW with AgNCs exhibits a stronger signal intensity as shown in **Figure 3.7b**. These results indicate the localization of

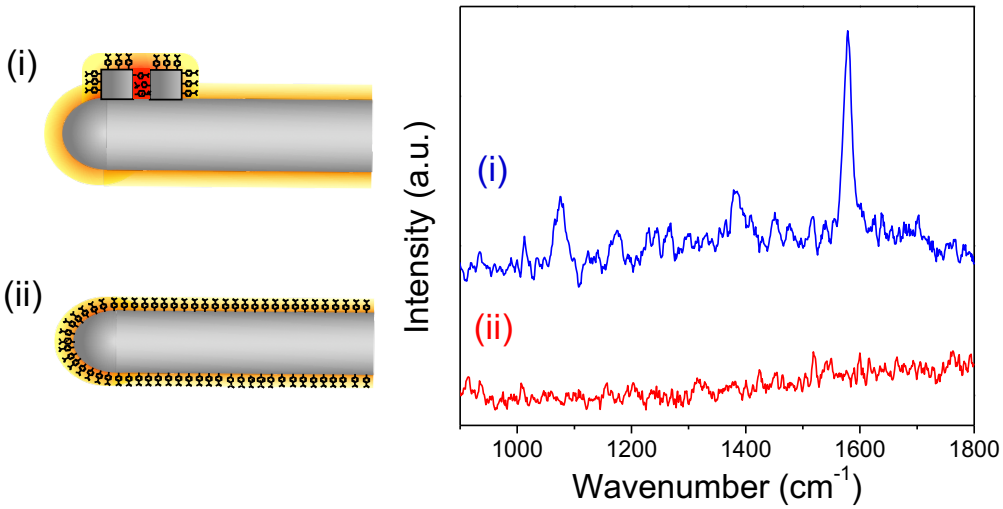


**Figure 3.7.** Raman spectra enhancement of 4-MBA due to the LSPR between AgNCs. (i) Raman spectrum of 4-MBA SAM on AgNCs at the tip of a AgNW. (ii) Raman spectrum of 4-MBA SAM on a AgNW without AgNCs.

a strong electric field around the AgNCs leading to a significant enhancement of the Raman scattering of 4-MBA.

Due to the difficulties in achieving the same surface area coverage with a SAM of a given target molecule, qualitative enhancement of the Raman scattering contributed by AgNCs was demonstrated through the experiment.

For the quantitative analysis of the enhancement, we simulated the electric field distributions near the AgNCs at the tip of AgNW and compared them to a bare AgNW (**Figure 3.8**). The largest electric field enhancement was observed with Edge-Edge oriented dimer AgNCs with an electric field enhancemet factor larger than 1645 and 1526 relative to the incident field value calculated without any nanostructures. With dimer AgNCs at the tip of a AgNW, the Raman scattering magnitude can be enhanced by at least 8 orders of magnitude and as high as 12 orders of magnitude with Edge-Edge oriented dimers, thereby

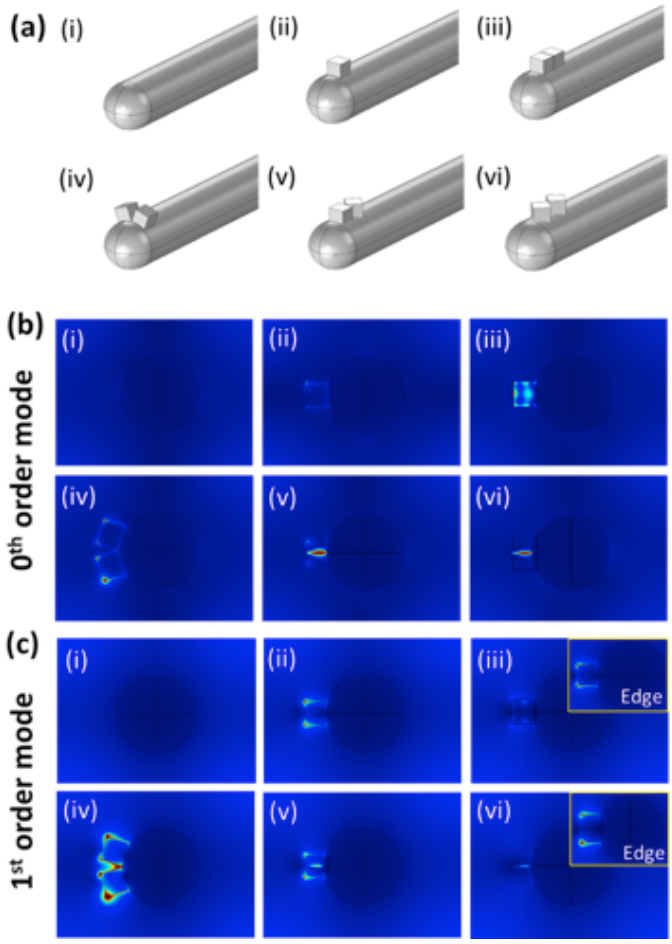


**Figure 3.8.** Enhancement of electric field attributed by AgNC attachment**.** (a) Geometries of the probes in the simulations and (b and c) their localized electric field distribution near the AgNCs excited by two lowest propagating surface plasmon modes. (i) Bare AgNW, (ii) Single AgNC at the tip of a AgNW. (iii-vi) AgNC dimers aligned in different orientations: Face-Face(FF)aligned in the direction of AgNW(iii) and perpendicular to AgNW direction(iv), (v) Face-Edge(FE) and (vi) Edge-Edge(EE) aligned in the direction of AgNW. The electric field distributions were taken on the plane 1nm distant from the edge of AgNC except (iv) which was taken at the edge of the AgNCs to show electric fields both in the gap and at the corners. The maximum electric field for the 1st order mode in (iii) and (vi) were not located in the gap but the outside corners and they are shown in the insets in (b iii) and (b vi).

exceeding the enhancement factor for single molecule detection (**Figure 3.9 b**)[21]. For living cell endoscopy, minimizing photo damage to living cells is an important factor to consider. For a bare AgNW however, long exposure times or a large laser input power are usually

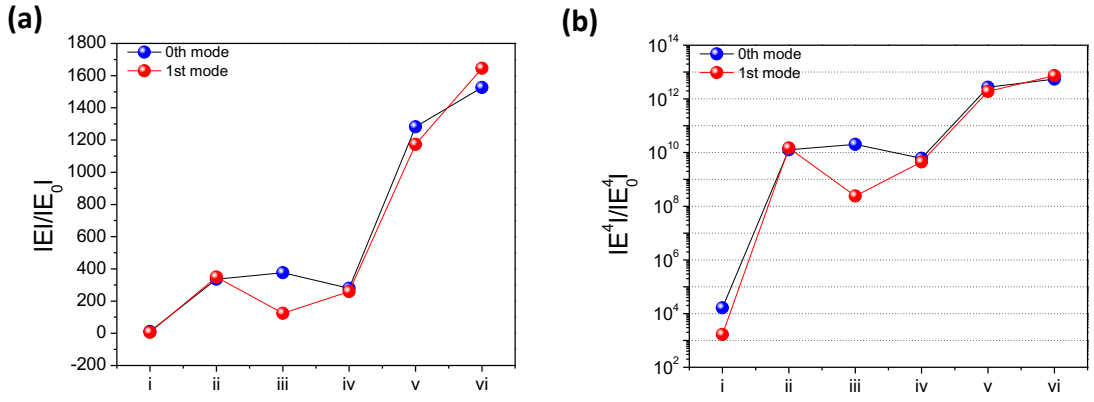


**Figure 3.9.** Electric field enhancement and Raman intensity due to AgNC attachment. (i): Bare AgNW (ii): Single AgNC at the tip of a AgNW (iii-vi): Dimer AgNCs in different orientations: Face-Face (FF) aligned in the direction of AgNW (iii) and perpendicular to AgNW direction(iv), Face-Edge (FE) (v), and Edge-Edge (EE) (vi) aligned in the direction of AgNW. $E_0$ is the electric field value calculated in the absence of AgNC and AgNW. The geometries of the AgNW and AgNCs at the tip of AgNW are shown in Figure S2(a).

required to collect enough Raman scattering due to its low electric field enhancement. By attaching a AgNC monolayer at the tip of a AgNW, most of the electric field is confined near the AgNCs and can be exploited for the excitation of the indicator of the target molecules due to its extraordinary excitation efficiency. As a result, we have achieved not only a highly sensitive endoscopy probe, but also a technique to lower photo-damage within living cells.

As previously mentioned, the top priority of preforming a live cell endoscopy is the intact analysis of intracellular processes while minimizing perturbations caused by the physical insertion of the endoscopy probe or by the incident light. Excitation of the E-field in the AgNC gaps via the nanowire waveguide has the advantage of inducing lower photo damage to the cell membrane while minimizing perturbations of cellular processes caused by the

incident laser beam than a far-field focused laser beam does. The large insertion volume of the probe however, may lead to serious damage or perturbations within the living cells. Although it was demonstrated that AgNC attached at the tip of the nanowire waveguide resulted in an exception al enhancement of Raman signal, the subsequent increase in volume of the nanowire waveguide is an inevitable consequence. An advantage of the AgNW nanowire waveguide is that the reduction of the nanowire diameter is available to compensate for the volume me increase of the waveguide due to the attachment of the AgNCs, which is an insurmountable problem to overcome with a dielectric nanowire due to the diffraction limit. Diverse nanowires with a high refractive index have been used in other groups to guide the light into live cells. Despite $SnO_2$ having the highest mode index(n=2.0)[22] among them, light still cannot be confined in and guided along the nanowire efficiently due to the high refractive index of water when using the diameters that cell viability and membrane integrity were experimentally tested and proven to be safe. On the other hand, the guidance of light as SPPs using a AgNW does not suffer from this diffraction limit, and therefore reduction of the waveguide volume could have been successfully achieved (**Figure 3.10**).

## 3.5. Measurement of pH in a living cell.

### 3.5.1 pH calibration curve

Using AgNC antenna coupled plasmonic AgNW probe, we measured the pH inside of a living Hela cell. 4-MBA is a well-known pH sensitive indicator for SERS[23-25] and has two pH sensitive Raman modes at around 1390$cm^{-1}$ and 1720 $cm^{-1}$ which are assigned to a

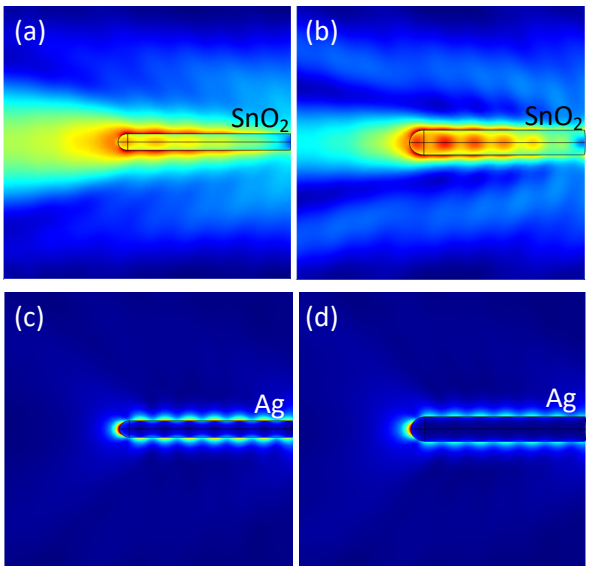


**Figure 3.10.** Two-dimensional projection of the modes excited by a highest effective mode index propagating along nanowire waveguides in water. $SnO_2$ NW with diameters of 120nm(a) and 180nm(b). AgNW with the diameter of 120nm(c) and 180nm(d).

stretching of $COO^-$ and C=O respectively. By comparing the pH sensitive modes with those of the aromatic ring breathing modes that are not sensitive to the pH change, pH calibration curves can be obtained. The non pH sensitive aromatic ring breathing modes are assigned at around 1100 and 1590 $cm^{-1}$. Here, we chose the two peaks at 1390$cm^{-1}$ and 1590 $cm^{-1}$ as a sensitive modes and non-sensitive modes to pH change respectively due to their strong intensities. **Figure 3.11** shows the pH calibration curve we obtained by taking the ratio of the peak intensity at 1390$cm^{-1}$/1590$cm^{-1}$. As pH of the media increases, the intensity of Raman modes at 1390$cm^{-1}$ increases due to the deprotonation of the COOH while the aromatic breathing modes at 1590 $cm^{-1}$ remain the same. **Figure 3.11(b)** was plotted with the relative ratio of 1390 $cm^{-1}$/1590 $cm^{-1}$ at different pH values. Our pH curve is placed in higher intensity ratios than those used for SERS in the other reports. This is

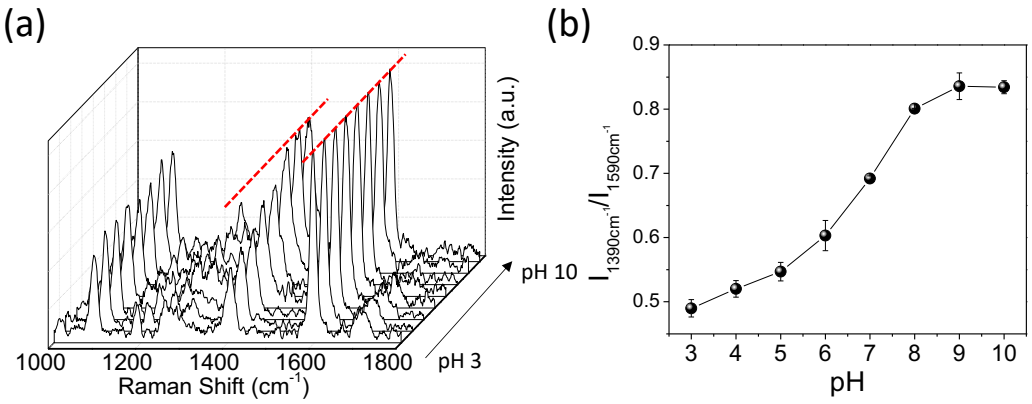


**Figure 3.11.** pH calibration curve (a) SERS spectra of MBA at different pH values from 3 to 10. (b) pH calibration curve obtained from (a) by taking the band ratio of $I_{1390cm-1}/I_{1590cm-1.}$ Each data point was measured 3 times repeatedly and averaged.

because their metallic cluster is not composed of a few but a great number of metallic particles. Therefore, the proton is not easily accessible to the 4-MBA located in the deep inside of the metallic cluster. A large proportion of 4-MBA remains without deprotonation and leads to low intensity of the mode at 1390 $cm^{-1}$. The high accessibility to target molecules of our endoscopy probe is also a promising feature as a sensor because the indicators can be saturated with the target molecule shortly. Based on this calibration curve, the pH in a Hela cell was measured. In order for this to occur, the cell was first incubated for 24 hours. To minimize any noise from the cell culture medium (Dulbecco's modified eagle medium, DMEM), the medium was exchanged with phosphate-buffered saline (PBS). Prior to that, the cell was washed with PBS five times to minimize the residual of the cell culture medium. First, Raman scattering of 4-MBA in the PBS solution in a glass-bottom petri-dish with Hela cells were measured using our ACPNE probe. ACPNE is an abbreviated name of antenna coupled plasmonic nanowire endoscopy that were made of

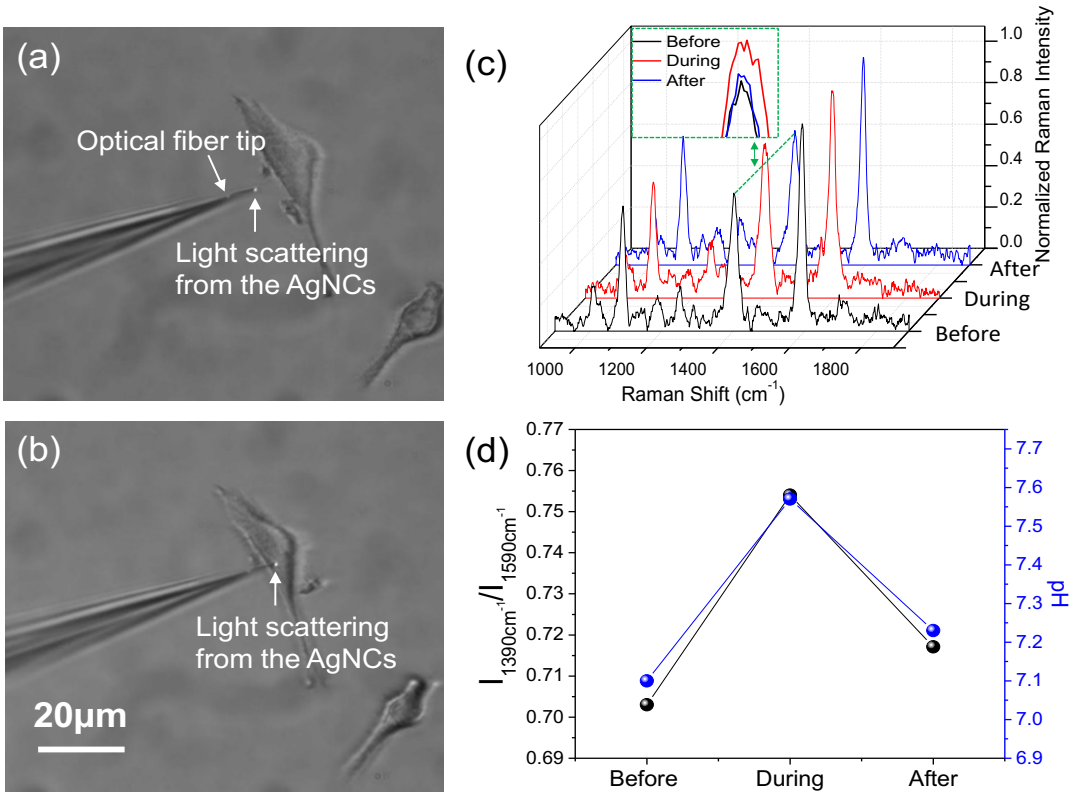


**Figure 3.12.** Measurement of pH in HeLa cell. Bright field optical microscope images before (a) and after (b) insertion of the ACPNE probe into the cytoplasm of a Hela cell. (c) Comparison of SERS spectra of 4-MBA inside and outside of Hela cell. (d) Band ratio ($I_{1390cm-1}/I_{1590cm-1}$) in a HeLa cell and its corresponding pH value calculated from pH calibration curve in Figure 3.11(b).

AgNCs functionalized with 4-MBA at the tip of a AgNW coupled to optical fiber. Using a triple-axis micromanipulator, the probe was inserted into the cytoplasm of a Hela cell and Raman scattering of 4-MBA was measured with 30 mins exposure time. The probe was then retracted from the cell and the Raman scattering of 4-MBA was measured again. More details about the experimental condition are described in the experiment section. **Figure 3.12** shows that bright field optical microscope images taken during the experiment. The

illumination spot at the tip of AgNW shows that the most of the laser input power was used to excite Raman scattering of 4-MBA resulting in the minimum photo-damage to the cell. The Raman spectra of 4-MBA in the cell and PBS solution are shown in **Figure 3.12c**. A slight variation of the peak intensity at 1390 $cm^{-1}$ was confirmed. **Figure 3.12d** shows the intensity ratios of 1390 $cm^{-1}$/1590 $cm^{-1}$ during the insertion of our probe into the cell and their corresponding pH values based on the calibration curve. The increase of pH to 7.57 was observed after the insertion of the probe into the cytoplasm of a Hela cell. This pH value is a 0.2 ~ 0.3 difference from that reported in a previous study (pH : ~7.35)[26]. We believe that the deviation of the pH values may come from the different measurement volume. The Raman indicator of 4-MBA in our probe only exists on the surface of AgNCs which measures the concentration of protons in femto-volume whereas the previous study measured the pH of entire cytoplasm of a Hela cell. The decrease of the pH after the probe retracted from the cell indicates the capability of reversible endoscopy sensing.

### 3.6. Cytotoxicity test of ACPNE

Using a ACPNE probe composed of AgNCs and a AgNW, the capability of pH measurement in a Hela cell was successfully demonstrated. However, it has been recently reported that Ag nanostructure materials are toxic towards human cells. The toxic effect of the Ag nanomaterials is attributed by the release of Ag ions from the nanomaterials [27-29]. The released Ag ions can interact with various biomolecules and affect the function of metabolites in cells [30-33]. Here, we investigated the cytotoxicity of our probe due to not only the physical damage or photo damage but also the toxic effect of the AgNCs and a AgNW during the optical sensing. For the cytotoxicity of our probe, Hela cells were cultured in a DMEM with a 10%

FBS in a 35mm petri-dish with grids (Ibidi) under a humidified air containing 5% $CO_2$ at 37°C for 24 h. Under the microscope, an ACPNE was inserted into the cytoplasm of randomly chosen Hela cells for 1 min. The bright field images of the cells including the surrounding area for references were taken and their locations were recorded using a black-illuminated CCD camera (Zyla 5.5, Andor, Belfast, UK) as shown in Figure S6a. The cell cytotoxicity of the laser irradiation was also investigated by inserting an ACPNE into randomly chosen Hela cells with 10μW laser output power (λ=532nm). After the cells were incubated at 37°C for 12 h again, the cell culture medium was removed and washed with DMEM without FBS two times. 2μM Calcein red-orange AM (Thermo Fisher Scientific) in DMEM was added to the petri-dish and it was incubated at 37 °C for 30 mins in the presence of 5% $CO_2$. Calcein AM is a non-fluorescent and hydrophilic molecules and can permeates live cells. Once the calcein AM is hydrolyzed by intercellular esterase, a strongly fluorescent calcein is produced and retained inside of the cell cytoplasm. Using the calcein AM marker, the verification of the cell viability is available by checking the fluorescence of calcein since the hydrolysis of calcein AM happens only inside of living cells. After staining the cells with the calcein, it was then washed with pure DMEM three times. Bright filed and fluorescent images of the cells were taken with their surrounding areas. In **Figure 3.13,** the cells that our probe was inserted into was split into two after 12 h incubation time and this split indicates that the cells are alive. The fluorescence image in Figure S6c clearly confirms that the split both cells are in good health. Statistical analysis of cell viability tests were performed following the same procedure above (**Table 3.1**). The influence of the

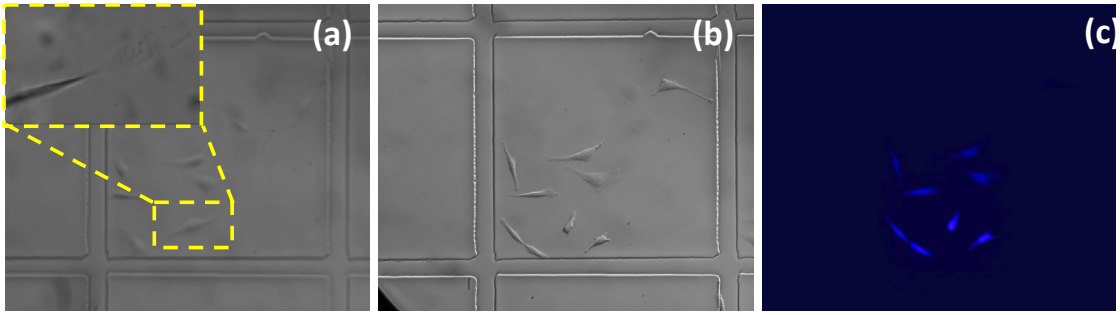


**Figure 3.13.** Cytotoxicity of ACPNE probe during insertion and illumination in a single living HeLa cell. (a) Bright-field image of Hela cell on a petri-dish with grid. The upper inset in (a) shows the ACPNE probe into the cytoplasm of a Hela cell. (b and c) Bright-field and fluorescence image of the cells stained with Calcein orange-red AM 12hrs after the insertion of ACPNE probe.

local illumination on the cell viability was also investigated in the analysis by sending a 30mW laser through the optical fiber (~10 µW output laser power).

The statistical analysis result of the cell viability test shows that all cells survived after the insertion of our probe and local illumination of the light. This result elucidates in a roundabout way that the release of silver ions from our probe is not considerable enough to damage the cell due to the small surface area exposed to the cell directly and short period of the exposure time.

Cell membrane integrity test during insertion of our probe was also investigated. In order for that, Hela cells were cultured in a DMEM with a 10% FBS in a 35mm petri-dish with grids (Ibidi) under a humidified air containing 5% $CO_2$ at 37°C for 24 h. Under the microscope, an ACPNE was inserted into the cytoplasm of randomly chosen Hela cells for

**Table 3.1.** Statistics of cell viability rate after the SERS probe insertion for 1 min.

| | Insertion duration (min) | Cell viability rate |
|---|---|---|
| Without laser | 1 | 100% (10/10) |
| With laser | 1 | 100% (5/5) |

1 min. The bright field images of the cells including the surrounding area for references were taken and their locations were recorded using a black-illuminated CCD camera (Zyla 5.5, Andor, Belfast, UK) as shown in Figure S6a. The cell cytotoxicity of the laser irradiation was conducted by inserting an ACPNE into randomly chosen Hela cells with 10μW laser output power (λ=532nm). After the cells were incubated at 37°C for 12 h again, the cell culture medium was removed and washed with DMEM without FBS two times. 2μM Calcein red-orange AM (Thermo Fisher Scientific) in DMEM was added to the petri-dish and it was incubated at 37 °C for 30 mins in the presence of 5% $CO_2$. Calcein AM is a non-fluorescent and hydrophilic molecules and can permeates live cells. Onc e the calcein AM is hydrolyzed by intercellular esterase, a strongly fluorescent calcein is produced and retained inside of the cell cytoplasm. Using the calcein AM marker, the verification of the cell viability is available by checking the fluorescence of calcein since the hydrolysis of calcein AM happens only inside of living cells. After staining the cells with the calcein, it was then washed with pure DMEM three times. Bright filed and fluorescent images of the cells were taken with their surrounding areas. In Figure 3.5Sb, the cells that our probe was inserted into was split into two after 12 h incubation time and this split indicates that the cells are alive. The fluorescence image in Figure S6c clearly confirms that the split both

cells are in good health. Statistical analysis of cell viability tests was performed following the same procedure above (**Table 3.1**). The influence of the local illumination on the cell viability was also investigated in the analysis by sending a 30mW laser through the optical fiber (~10 μW output laser power).

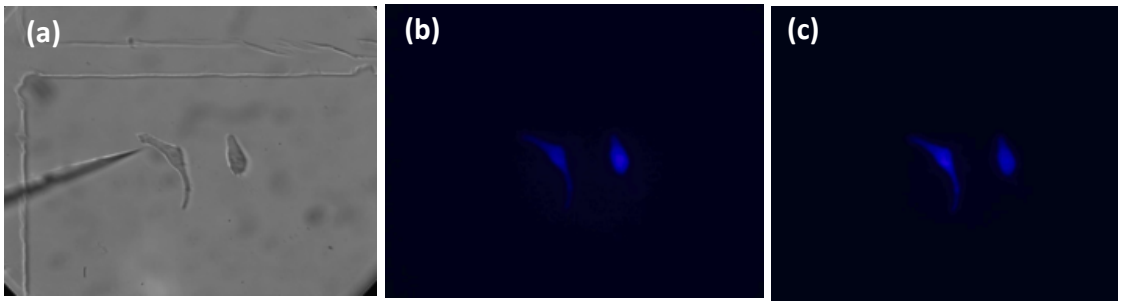


**Figure 3.14.** Cell membrane integrity test during insertion of ACPNE probe. (a) Bright-field image of the ACPNE probe inserted into the cytoplasm of a Hela cell. Fluorescence images of the cells stained with Calcein orange-red AM before (b) and after (d) the insertion of ACPNE probe.

### 3.7. Membrane integrity test

The fluorescence image of the cell stained with calcein was monitored in real time while an ACPNE was inserted and retracted to test the membrane integrity of the Hela cell. The Hela cells were cultured and stained following the procedure described in the previous section. The fluorescence image of the cell was taken with a surrounding area prior to the insertion of an ACPNE. Then the nanowire was slowly inserted into a cytoplasm of a Hela cell. After 1 min, the nanowire was retracted, and its fluorescence image was taken again.

### 3.8. Conclusion

Using a ACPNE probe composed of AgNCs and a AgNW, the capability of pH measurement in a Hela cell was successfully demonstrated. However, it has been recently reported that Ag nanostructure materials are toxic towards human cells. The toxic effect of the Ag nanomaterials is attributed by the release of Ag ions from the nanomaterials [27-29]. The released Ag ions can interact with various biomolecules and affect the function of metabolites in cells [30-33]. Here, we investigated the cytotoxicity of our probe due to not only the physical damage or photo damage but also the toxic effect of the AgNCs and a AgNW during the optical sensing (See supporting information). The statistical analysis result of the cell viability test shows that all cells survived after the insertion of our probe and local illumination of the light. This result elucidates in a roundabout way that the release of silver ions from our probe is not considerable enough to damage the cell due to the small surface area exposed to the cell directly and short period of the exposure time.

## 3.9. References


1. Prescher, J. A.; Bertozzi, C. R., Chemistry in living systems. *Nature chemical biology* **2005,** *1* (1), 13-21.

2. Chen, X.; Kis, A.; Zettl, A.; Bertozzi, C. R., A cell nanoinjector based on carbon nanotubes. *Proceedings of the National Academy of Sciences* **2007,** *104* (20), 8218-8222.

3. Yum, K.; Wang, N.; Yu, M. F., Electrochemically controlled deconjugation and delivery of single quantum dots into the nucleus of living cells. *Small* **2010,** *6* (19), 2109-2113.

4. Shalek, A. K.; Robinson, J. T.; Karp, E. S.; Lee, J. S.; Ahn, D.-R.; Yoon, M.-H.; Sutton, A.; Jorgolli, M.; Gertner, R. S.; Gujral, T. S., Vertical silicon nanowires as a universal platform for delivering biomolecules into living cells. *Proceedings of the National Academy of Sciences* **2010,** *107* (5), 1870-1875.

5. Yan, R.; Park, J.-H.; Choi, Y.; Heo, C.-J.; Yang, S.-M.; Lee, L. P.; Yang, P., Nanowire-based single-cell endoscopy. *Nature nanotechnology* **2012,** *7* (3), 191-196.

6. Cao, Y. C.; Jin, R.; Mirkin, C. A., Nanoparticles with Raman spectroscopic fingerprints for DNA and RNA detection. *Science* **2002,** *297* (5586), 1536-1540.

7. Zipfel, W. R.; Williams, R. M.; Webb, W. W., Nonlinear magic: multiphoton microscopy in the biosciences. *Nat Biotechnol* **2003,** *21* (11), 1369-1377.

8. Thorn, K., A quick guide to light microscopy in cell biology. *Mol Biol Cell* **2016,** *27* (2), 219-222.

9. Singhal, R.; Orynbayeva, Z.; Kalyana Sundaram, R. V.; Niu, J. J.; Bhattacharyya, S.; Vitol, E. A.; Schrlau, M. G.; Papazoglou, E. S.; Friedman, G.; Gogotsi, Y., Multifunctional carbon-nanotube cellular endoscopes. *Nat Nano* **2011,** *6* (1), 57-64.

10. Niu, J. J.; Schrlau, M. G.; Friedman, G.; Gogotsi, Y., Carbon Nanotube-Tipped Endoscope for In Situ Intracellular Surface-Enhanced Raman Spectroscopy. *Small* **2011,** *7* (4), 540-545.

11. Lee, J.; Lee, H. R.; Pyo, J.; Jung, Y.; Seo, J. Y.; Ryu, H. G.; Kim, K. T.; Je, J. H., Quantitative Probing of Cu2+ Ions Naturally Present in Single Living Cells. *Advanced Materials* **2016,** *28* (21), 4071-4076.

12. Gramotnev, D. K.; Bozhevolnyi, S. I., Plasmonics beyond the diffraction limit. *Nature photonics* **2010,** *4* (2), 83-91.

13. Lu, G.; De Keersmaecker, H.; Su, L.; Kenens, B.; Rocha, S.; Fron, E.; Chen, C.; Van Dorpe, P.; Mizuno, H.; Hofkens, J., Live-Cell SERS Endoscopy Using Plasmonic Nanowire Waveguides. *Advanced Materials* **2014,** *26* (30), 5124-5128.

14. Nikbakht, H.; Latifi, H.; Oraie, M.; Amini, T., Fabrication of Tapered Tip Fibers With a Controllable Cone Angle Using Dynamical Etching. *Journal of Lightwave Technology* **2015,** *33* (23), 4707-4711.

15. Gao, B.; Arya, G.; Tao, A. R., Self-orienting nanocubes for the assembly of plasmonic nanojunctions. *Nat Nano* **2012,** *7* (7), 433-437.

16. Korte, K. E.; Skrabalak, S. E.; Xia, Y., Rapid synthesis of silver nanowires through a CuCl-or CuCl 2-mediated polyol process. *Journal of Materials Chemistry* **2008,** *18* (4), 437-441.

17. Yan, R.; Park, J.-H.; Choi, Y.; Heo, C.-J.; Yang, S.-M.; Lee, L. P.; Yang, P., Nanowire-based single-cell endoscopy. *Nat Nano* **2012,** *7* (3), 191-196.

18. Deegan, R. D.; Bakajin, O.; Dupont, T. F.; Huber, G.; Nagel, S. R.; Witten, T. A., Capillary flow as the cause of ring stains from dried liquid drops. *Nature* **1997,** *389* (6653), 827-829.

19. Hu, H.; Larson, R. G., Analysis of the effects of Marangoni stresses on the microflow in an evaporating sessile droplet. *Langmuir* **2005,** *21* (9), 3972-3980.

20. Hu, H.; Larson, R. G., Marangoni effect reverses coffee-ring depositions. *The Journal of Physical Chemistry B* **2006,** *110* (14), 7090-7094.

21. Blackie, E. J.; Ru, E. C. L.; Etchegoin, P. G., Single-molecule surface-enhanced Raman spectroscopy of nonresonant molecules. *Journal of the American Chemical Society* **2009,** *131* (40), 14466-14472.

22. Manifacier, J.; De Murcia, M.; Fillard, J.; Vicario, E., Optical and electrical properties of SnO2 thin films in relation to their stoichiometric deviation and their crystalline structure. *Thin Solid Films* **1977,** *41* (2), 127-135.

23. Pallaoro, A.; Braun, G. B.; Reich, N.; Moskovits, M., Mapping local pH in live cells using encapsulated fluorescent SERS nanotags. *Small* **2010,** *6* (5), 618-622.

24. Jaworska, A.; Jamieson, L. E.; Malek, K.; Campbell, C. J.; Choo, J.; Chlopicki, S.; Baranska, M., SERS-based monitoring of the intracellular pH in endothelial cells: the influence of the extracellular environment and tumour necrosis factor-α. *Analyst* **2015,** *140* (7), 2321-2329.

25. Michota, A.; Bukowska, J., Surface-enhanced Raman scattering (SERS) of 4-mercaptobenzoic acid on silver and gold substrates. *J Raman Spectrosc* **2003,** *34* (1), 21-25.

26. Llopis, J.; McCaffery, J. M.; Miyawaki, A.; Farquhar, M. G.; Tsien, R. Y., Measurement of cytosolic, mitochondrial, and Golgi pH in single living cells with green fluorescent proteins. *Proceedings of the National Academy of Sciences* **1998,** *95* (12), 6803-6808.

27. Ivask, A.; ElBadawy, A.; Kaweeteerawat, C.; Boren, D.; Fischer, H.; Ji, Z.; Chang, C. H.; Liu, R.; Tolaymat, T.; Telesca, D., Toxicity mechanisms in Escherichia coli vary for silver nanoparticles and differ from ionic silver. *ACS nano* **2013,** *8* (1), 374-386.

28. Pal, S.; Tak, Y. K.; Song, J. M., Does the antibacterial activity of silver nanoparticles depend on the shape of the nanoparticle? A study of the gram-negative bacterium Escherichia coli. *Applied and environmental microbiology* **2007,** *73* (6), 1712-1720.

29. Greulich, C.; Braun, D.; Peetsch, A.; Diendorf, J.; Siebers, B.; Epple, M.; Köller, M., The toxic effect of silver ions and silver nanoparticles towards bacteria and human cells occurs in the same concentration range. *RSC Advances* **2012,** *2* (17), 6981-6987.

30. Ahamed, M.; Karns, M.; Goodson, M.; Rowe, J.; Hussain, S. M.; Schlager, J. J.; Hong, Y., DNA damage response to different surface chemistry of silver nanoparticles in mammalian cells. *Toxicology and applied pharmacology* **2008,** *233* (3), 404-410.

31. Morones, J. R.; Elechiguerra, J. L.; Camacho, A.; Holt, K.; Kouri, J. B.; Ramírez, J. T.; Yacaman, M. J., The bactericidal effect of silver nanoparticles. *Nanotechnology* **2005,** *16* (10), 2346.

32. Slawson, R.; Lee, H.; Trevors, J., Bacterial interactions with silver. *Biology of metals* **1990,** *3* (3-4), 151-154.

33. Ruparelia, J. P.; Chatterjee, A. K.; Duttagupta, S. P.; Mukherji, S., Strain specificity in antimicrobial activity of silver and copper nanoparticles. *Acta biomaterialia* **2008,** *4* (3), 707-716.

# Chapter 4

# Plasmonic NW waveguide for near-field imaging

### 4.1. Near fields

Optical microscopy is an imaging method that uses visible light as an illuminating source to observe specimen under high magnification. It is by far the most widely used imaging technique, especially for material/device characterizations and biology because it is fast, easy to use, compact, and for its versatility. Optical microscopy offers a broad spectrum of contrast mechanisms which include the transmission, reflection, fluorescence, Rayleigh and Raman scattering, electronic information, micro and macrostructure of the specimen, and chemical fingerprints. It is also non-invasive and thus can work both in air and liquid. It requires minimal sample preparation; which is especially important for biological imaging.

However, the most significant limitation of optical microscopy is its spatial resolution. The optical spatial resolution is defined by the diffraction limit, which can be estimated by the Rayleigh Criterion (Eq. (1)).

$$\mathrm{D} = 1.220\frac{\lambda}{2nsin(\theta)} \quad (1)$$

Here, D is the distance that two adjacent points can be resolved. λ is the wavelength of the light, $n$ is the refractive index of the medium between the objective lens and specimen, and θ is the half-angle of the angular aperture[1-2]. The highest spatial resolution that can be achieved with the shortest wavelength of visible light ($\lambda = 400\mathrm{nm}$) is about 200 nm. This

resolution limitation motivated the development of Near-field Scanning Optical Microscopy (NSOM)

In 1928, Synge brought a new idea with the optical microscope that can break the diffraction limit by passing light through an aperture whose dimension was much smaller than the wavelength, and by placing the specimen in the proximity of the aperture[3]. This new idea became the foundation of the modern-day NSOM. Here, the highly spatially confined wave near the aperture ($d \ll \lambda$) is called "near field." Angular spectrum representation can understand the wave propagation. The electric field in a plane (z=const.) can be expressed in the form of exp ($i\boldsymbol{kr} - i\omega t$) with amplitudes$\bar{E}(k_x, k_y, \mathrm{z} = 0)$. Then, the time harmonic wave equation can be expressed as follows

$$\boldsymbol{E}(x, y, z) = \iint_{-\infty}^{\infty} \bar{E}(k_x, k_y, \mathrm{z})\mathrm{e}^{-\mathrm{i}(k_x \mathrm{x} + k_y \mathrm{y})}\mathrm{e}^{\pm \mathrm{i} k_z z} dk_x dk_y \qquad (2)$$

where the wave vector $\boldsymbol{k}$ is defined by $|\boldsymbol{k}| = \sqrt{k_x^2 + k_y^2 + k_z^2} = 2\pi n/\lambda$. Considering a polarized wave in x-z plane in air (n=1) for the simplicity, the equation (2) can be simplified to$|k_z| = \sqrt{{2\pi^2}/{\lambda^2} - {k_x}^2}$. Here, the $\pm$ sign in the $\mathrm{e}^{\pm \mathrm{i} k_z z}$ represents the propagation of the wave in positive and negative z direction. If $k_x \leq {2\pi}/{\lambda}$, $k_z$ becomes real and the wave propagates in z direction with an oscillation of $\mathrm{e}^{-\mathrm{i} k_z z}$. However, $k_z$ becomes complex if $k_x \geq {2\pi}/{\lambda}$, and the term $\mathrm{e}^{-|k_z| z}$ accounts for exponential decay of the fields in z direction. As a results, only the wavevectors with $k_x \leq {2\pi}/{\lambda}$ can propagate long distance, while the wave with $k_x > {2\pi}/{\lambda}$ become evanescent and exists only near the light source[4]. By

placing the aperture adjacent to the specimen, the evanescent wave can be utilized, and high frequency spatial resolution can be obtained.

### 4.1.1. Aperture mode near-field optical microscopy (Aperture-NSOM).

The optical microscopy with the probe terminated by the aperture is called Aperture Mode Optical Microscopy. The probe can be fabricated by pulling or etching the tapering optical fibers. Then, the tip of the optical fiber is coated with a variety of metal substances. Light coupled to the optical fiber passes through the aperture with the dimensions much smaller than the wavelength and with higher spatial resolution than the diffraction limit that could be obtained by placing the probe or detector closely to the specimen as shown in Figure 4.1(a). The diameter of the aperture determines its spatial resolution, which ranges from 10 nm to 100 nm[5]. Since the light comes only from the tip of the optical fiber, images with high contrast can be obtained. However, the $10^{-5 \sim -6}$ throughput loss of the laser after passing through the small aperture reduces the scanning speed significantly[6-7].

### 4.1.2. Apertureless mode near-field optical microscopy (Apertureless-NSOM).

Apertureless mode utilizes a sharp metal tip as a local excitation resonator as shown in Figure 4.1(b). The laser beam focused on the metal tip induces a strong, locally enhanced field at its apex. Therefore, the spatial resolution and the signal enhancement are determined by the sharpness of the tip. The apertureless-NSOM can reach a much higher spatial resolution ranging from a few to 20 nm, which is higher than the aperture-NSOM[5]. Since external illuminations are used to create the local field, it has the significantly high

background. Using a tapping mode AFM, the high background can be suppressed by demodulating the optical signal with lock-in detection technique at the fundamental or higher harmonics of the tapping mode frequency[8]. However, it is still not suitable for fluorescence measurements because photobleaching readily occurs due to the intense

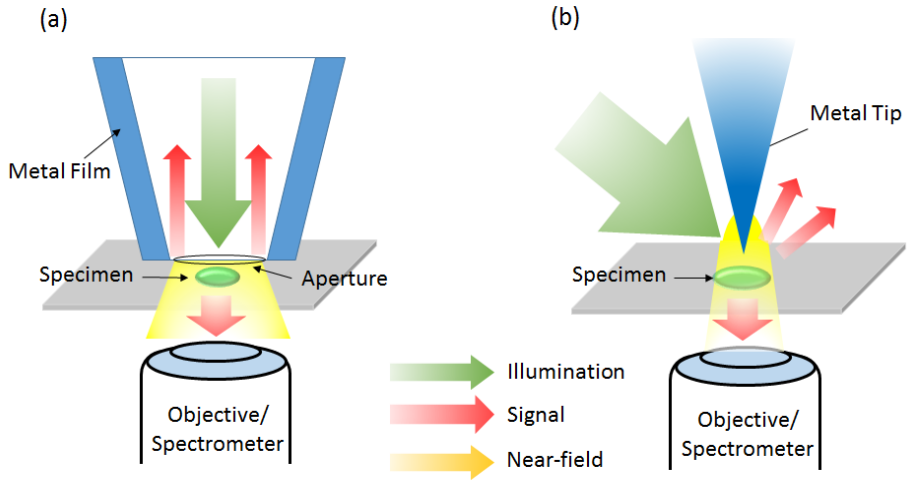


**Figure 4.1.** Schematic illumination of (a) aperture-NSOM and (b) apertureless-NSOM. external illumination.

## 4.2. Adiabatic nanofocusing of surface plasmon polariton (SPP)

It is clear that substantial interferences with a far-field background for apetureless NSOM and low throughput for aperture NSOM are the challenges need to be overcome. In the last decade, there have been significant efforts to improve the constraints of each NSOM modes. An intuitive idea to reduce the background noise of apertureless NSOM is remote excitation employing grating-coupling of SPP modes[9]. With axial polarized far-field excitation, radially symmetric SPP mode radiation at the apex of the probe could have been accomplished.

Although it showed a remarkable reduction of the background noise and excitation efficiency compared to the conventional apertureless NSOM, many issues must be addressed to be commonly used. First, selective excitation condition of the fundamental TM mode (m=0) must be addressed even though the conical tip can act as an effective mode filter. The other higher order mode excited together with the fundamental mode may radiate at the cutoff cone radius and therefore increase the background noise. Second, the inefficient grating coupling can still produce a substantial scattering and result in a lower contrast of the spectra. Third, considerable propagation loss occurs during the delivery of the light to the deep subwavelength dimensions using nanotips due to either the long distance between the grating and the apex of the probe. Especially, the probe fabricated by top-down method produces a considerable scattering loss of the SPP. Also, the fabrication method of the probe with grating is expensive and requires a complicating semi-conducting process. Last but not least, broadband nanofocusing relying on the grating is experimentally challenging.

Although the apertureless NSOM including the nanofocusing probe with grating now provides highest spatial optical resolution, the fiber-based aperture NSOM still has a high potential regarding contrast of the spectral signal. Also, the fiber-based aperture NSOM has exceptional merit that complicated optical alignment may not be necessary if the throughput is high. Recently, there have been a few reports that introduced new fiber based aperture NSOM probes with an efficient light delivery from the fiber to the metal apex[10-12]. Unfortunately, the transmission of the probes from the optical fiber to the metal tip is

still significantly low due to a substantial reflection in the coupling points and scattering and absorption losses originated from top-down grown Au tips.

### 4.2.1. Adiabatic plasmonic nanofocusing from the optical fiber to a AgNW

In this work, we introduce and experimentally demonstrate a fully integrated fiber-based NSOM probe using a sharp metal NW based on "genuine" broadband adiabatic plasmonic nanofocusing and alignment-free fiber-in-fiber-out platform. Here, the adiabatic means no energy loss in the process of focusing light at the nanoscale. The adiabatic nanofocusing of the light was realized by placing a chemically synthesized AgNW at a tapered optical fiber (See Figure 4.2). After fully understanding the coupling mechanism and optimization, selective excitation of the fundamental mode with a high transmission could be accomplished. The adiabatic plasmonic nacnofocusing allows for not only high

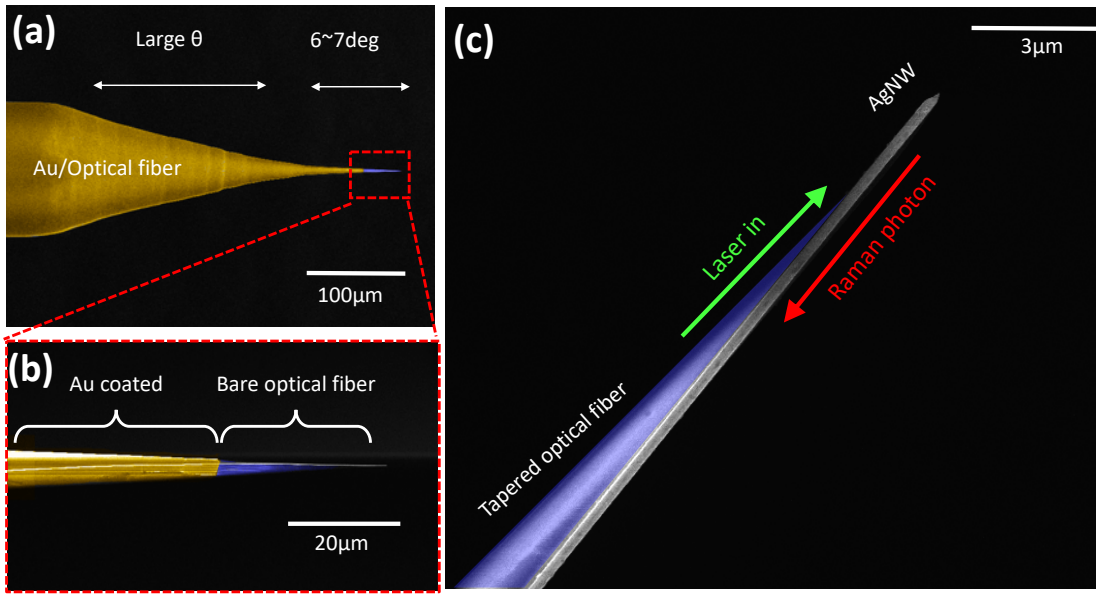


**Figure 4.2.** SEM images of the plasmonic NW NSOM probe. (a) SEM images of Au coated tapered optical fiber with a AgNW at the tip of the optical fiber. (b) Zoomed-in image of (a). (c) High magnification image of the plasmonic NW NSOM probe tip.

transmission but also Raman signal collection through the same light path, for the excitation. These excitation and collection configurations do not require optical components used for focusing light nor a very careful tedious optical system alignment. This new probe design also allows for higher device reliability due to a simple probe preparation method, which is another major limitation for conventional adiabatic nanofocusing NSOM probes.

### 4.2.2. Minimization of losses in the process of adiabatic nanofocusing.

The propagation loss in metallic NWs arises from Joule heating as SPs which is essentially an electrons oscillation wave, which propagates along the waveguide. Therefore, to overcome this issue, Ag, which has the lowest intrinsic ohmic loss of all metals in the visible frequency range, is the natural material choice for this project. However, experimentally obtained losses always deviate from predicted losses accounted for through the relative permittivity of the metal. The difference is originated from the imperfections of the samples such as low crystallinity, rough surface, and impurities, etc. To limit the scattering loss from grain boundaries, structural defects, and surface roughness, the AgNW synthesized via polyol-mediated reduction of $AgNO_3$ in the presence of polyvinylpyrrolidone (PVP) is the ideal choice. These AgNWs have been demonstrated to have a more remarkably lower propagation loss than their lithographically defined counterparts[13]. Such low ohmic loss arises from (1) the single crystalline nature, (2) chemical homogeneity or low impurity level, and (3) atomically smooth surfaces. All of these mentioned factors effectively reduce the electron scattering during the collective

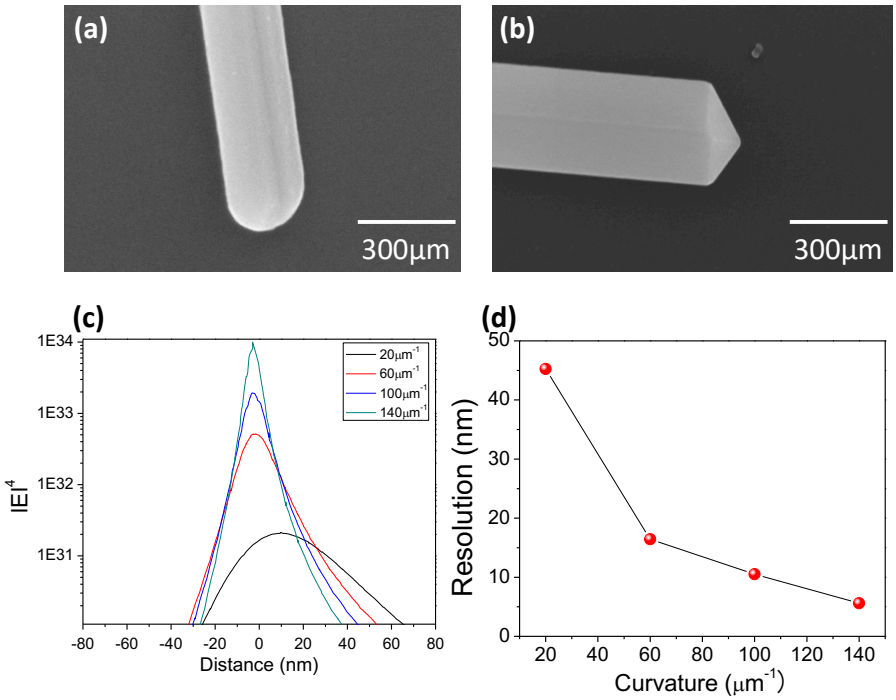


**Figure 4.3.** Raman resolution as function of tip curvature (a) SEM image of AgNW with rounded tip shape (b) SEM image of AgNW with sharp tip. (c) Calculated $|E|^4$ as function of tip curvature (d) Raman resolution as function of tip curvature.

electron oscillations in the plasmonic waveguide. For the application of the AgNW waveguide for the NSOM probe, the tip shape of the AgNW must be considered. Figure 4.3 shows the calculated Raman resolution as a function of the tip curvature. Sharp AgNW must be prepared to increase the spatial resolution of the near field imaging. Then, oxidative etching must be prevented during the synthesis and storage. Figure 4.3a shows the rounded AgNW tip after the oxidative etching. This etching process can be prevented by synthesizing and purified the NWs in the deoxygenated solution. Figure 4.3b shows the tip shape of AgNWs synthesized in the deoxygenated environment.

### 4.2.3. Selective excitation of the fundamental mode with a high coupling efficiency

To utilize the sharp tip of the AgNW, delivery of the SPP to the apex of the NW tip is required. Hence, fundamental mode which does not experience cut off on the corner of the NW tip must be dominantly excited for the high spatial resolution (Figure 4.4). Finding optimum light coupling from optical to the AgNW regarding not only the coupling efficiency but also weight of the mode needs to be considered. The adiabatic nanofocusing light from the optical fiber to AgNW is dependent on taper angle and NW diameter, the polarization of the incident light. In the tapered region of the optical fiber, the light coupling from the optical fiber to AgNW occurs when the reduced effective mode index of the mode in the optical fiber matches with the one of SPP in AgNW. As the taper angle becomes lower, it is predictable that it provides a longer time for the energy of the mode

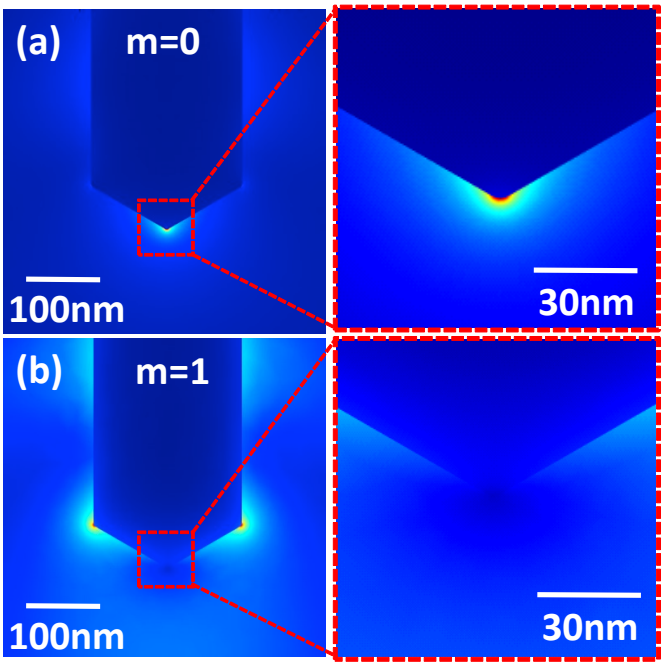


**Figure 4.4.** E-field distribution at the tip of AgNWs excited with m=0 (a) and m=1 (b) mode at 532nm.

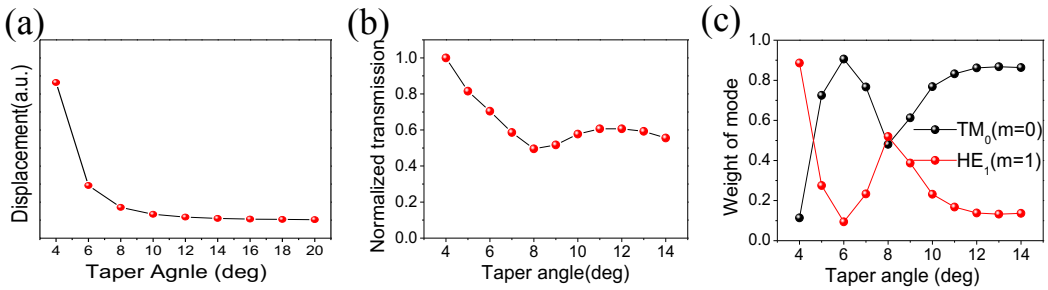


**Figure 4.5.** Dependency of taper angle on the displacement, transmission, and weight of modes of the plasmonic NW NSOM probe. (a) Calculated displacement as function of optical fiber taper angle with a certain shear force applied along the optical fiber. Calculated transmission (b) and weight of modes (c) as function of taper angle with a 200nm AgNW for 532nm excitation wavelength.

in optical fiber waveguide to transfer to the SPP in AgNW waveguide while the mode match length is short for the large taper angle. Therefore, smaller taper angle is prefered to obtain high light coupling. Figure 4.5 shows the dependency of the calculated transmission as a function of the taper angle. The results show that the transmission decrease with the increase of the taper angle.

Vibrational motion of our plasmonic NSOM probe due to the external perturbation limits the spatial resolution of both STM and Raman images. However, lowering the taper angle to obtain high coupling efficiency does not always work. Therefore, the displacement of our waveguide by the external perturbation need to be considered. The Young's modulus of AgNW and optical fiber are 160 GPa and ~70 GPa respectively[14-17]. Considering Young's modulus, it can be assumed that the displacement of the probe relies on the tapered optical fiber dominantly. In addition, Ma et al. demonstrated AFM images with a high spatial resolution using AgNW mounted AFM tips which indicates that the displacement of the AgNW is not significant[18]. Consequently, numerical simulations using Comsol

Multiphysics was conducted to calculate the relative displacement of the optical fiber as a function of the taper angle. The simulation result show that a significant reduction of the displacement was observed after the taper angle becomes larger than 6°. This taper angle also satisfies both a high transmission and high weight of the fundamental mode with a AgNW (200nm in diameter). Based on the simulation results, optical fibers with taper angle 6° were used to scan and obtain Raman spectra of samples for all the following experimental results.

Another important parameter that determines the coupling efficiency is NW diameter. The AgNW with different NW diameter supports SPP with a different effective mode index. The different mode index results in a different propagation loss, different mode coupling between two waveguides due to the propagation constant difference ($\Delta\beta = \beta_{AgNW} - \beta_{OF}$ ) which is also related to the coupling coefficient. Therefore, finding the optimal NW diameter ranges must be fulfilled. Besides the coupling efficiency, selective excitation of the fundamental mode is necessary to deliver the light to the apex of the silver NW without any scattering loss at the tip corner. The far-field radiation of the fundamental mode at the tip of the AgNW has a ring pattern with a radially polarization while that of the second order mode (m=1) has a dot pattern with a linear polarization. In addition, the ring pattern of the fundamental mode radiates with a larger angle compared to the second order mode. This difference can be more clearly distinguished in k-space. Thus, we acquired the both real space and k-space images of far-field radiation from AgNW tips and their polarizations were analyzed to further confirm the mode number (see Figure 4.6). With the p polarized incident light, ring like pattern is observed from the far-field radiation at the tip of AgNW.

The ring like pattern in real space is associated with a large ring (large $k_r$) in k-space compared to s polarization of the incident light. On the other hand, s polarized incident light only can excite second order mode and produce only a dot radiation pattern at the tip of AgNW. In k-space image, a circular shape pattern in the center is dominantly shown which has a low $k_r$. To confirm the ring patterns and circular shape patterns in the center are associated with the fundamental and second order modes respectively, a linear polarizer in front of the CCD camera was installed. Figure 4.7 shows that the ring like patterns excited with a p polarized incident light still exist while the circular pattern in the center excited by s polarized light is almost disappeared. The results agree with the conclusion made with the real space images that the ring pattern is radially polarized while the circular pattern is linearly polarized. By comparing the relative ratio of the outer ring pattern with circular one in the center for the p-polarization, the weight of the modes in the AgNW were calculated as shown in Figure 4.8. For 532nm wavelength, 150nm is the cross point that the fundamental mode can dominantly excited. Based on the mode analysis results obtained here, the Tip-enhanced Raman spectroscopy (TERS) experiments were performed.

## 4.3. Optical scanning probe design

### 4.3.1. Scanning probe microscopy

As discussed in the near field session, placing the aperture in the vicinity of the specimen within a few nanometer distances and movement of the scanning probe maintaining the

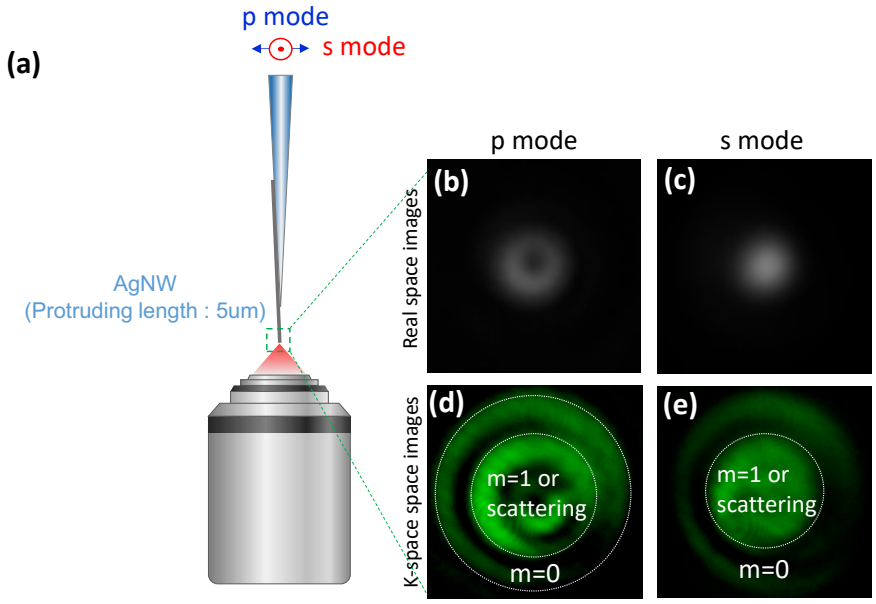


**Figure 4.6.** Real space and k-space images of far-field radiation from AgNW tip. (a) Schematic illustration of experimental setup for the acquisition of vertical far-field radiation pattern from AgNW tip. (b, c) Real space far-field radiation patterm from AgNW tip for p and s polarization of incident light. (d, e) (b, c) k-space far-field radiation patterm from AgNW tip for p and s polarization of incident light. The wavelength of the incident light is 532nm. The NW diameter is 220nm.

discrete distance is necessary. Therefore, an active feedback loop with a combination of controller, amplification, and the piezoelectric element is required. As a feedback parameter, atomic force microscopy employs either attractive force or repulsive interaction forces, and their operating modes are mainly classified into two: contact mode and non-contact mode. In contact mode, the sample or tip is moved along an x-y grid while the tip is in contact with the sample. Feedback loops monitor the deflection of the cantilever, and the height of the samples is adjusted to restore the set-point. Contact mode, therefore, relies on repulsive Van der Waals force as a tip-sample interaction force. On the other hand, non-contact mode exploits attractive Van der Waals force existing in the long distance from the surface of the samples. Tip oscillates at its resonant frequency in the non-contact mode and

lightly or does not contact the surface during scanning the samples. Contact mode AFM has many advantages over non-contact modes such as fast scanning speed, higher resolution, and capability of friction analysis. However, the drawback here is a high lateral force between tip and sample can result in the damage of sample or attachment of the objects from samples which leads to a poor resolution of the topological image. Although non-contact mode does not provide a resolution as high as contact mode does, it damages the samples less and suffers less from the attachment of objects from samples. Due to those reasons, the non-contact mode AFM is more popularly and primarily used for the NSOM probes which needs extreme care for attachment of the objects from samples and damage of the probes.

Si-cantilever is commercially available AFM probes which employees the reflected laser from the top side of the cantilever to monitor the tip-sample interaction [19]. However, it has many disadvantages that it requires an expensive optical measurement system, low stiffness and the requirement of large oscillation amplitude due to the low spring constant

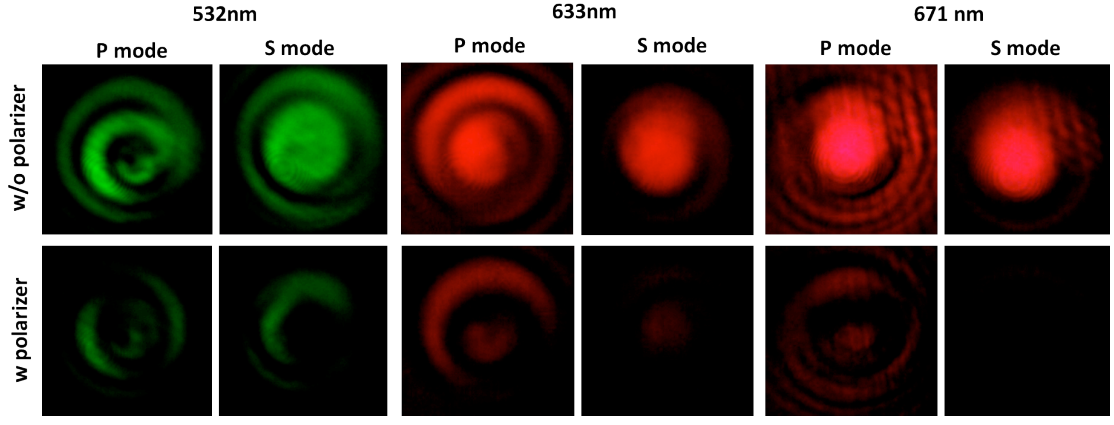


**Figure 4.7.** Polarization analysis of far-field radiation pattern in k-space from AgNW tip excited with p and s polarized light.

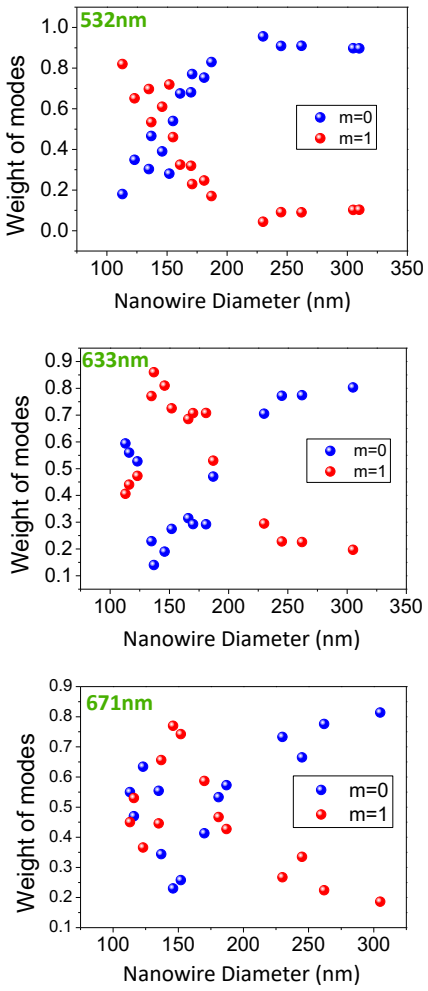


**Figure 4.8.** Weight of modes in AgNW excited with p polarized incident light for three different wavelengths (532, 633, and 671nm).

of Si cantilever results in a fragile and high cost of AFM probe. Another challenging difficulty of usage of Si-cantilever for NSOM probe is that the integration of optical fiber for the guidance of the light is not available due to the structural limitation. Fortunately, a nonoptical mean of monitoring the interaction between the sample and tip was developed for NSOM using a quartz tuning fork. This technique relies on the amplitude or phase change of resonant frequency of the tuning fork due to the tip-sample interactions.

Depending on the orientation of the optical fiber attachment on the tuning fork, either tapping or shear force mode can be used. Most highly resolved AFM images can be obtained using the tip oscillating perpendicularly to the samples (Tapping mode) due to the lower oscillating amplitude is required to detect the variation of attractive Van der Waals force with the movement of the oscillating probe. The deviated phase or amplitude from oscillating frequency is an averaged value within the range of the movement of the oscillating tuning fork. When the tip is close to the surface, the repulsive force ($10^{-9}$N) attributed by overlapping electron clouds compared to the attractive force ($10^{-12}$N) dominates and therefore, placing the probe into proximity of the sample surface is limited. The decrease of the oscillating amplitude is required to lower distance between the tip and samples. However, the limitation of minimizing the weight difference contributed by optical fiber attachment hinders from achieving the gap distance lower than 1nm.

In 1981, scanning tunneling microscope (STM) based on quantum tunneling was firstly introduced by Gerd Binning and Heinrich Rohrer[20]. The quantum tunneling is a phenomenon that electrons tunnel through the vacuum or air when two electrodes are brought into the proximity of each other with a particular bias. Assuming the tunneling current occurs at the pointed tip of the STM probe, the tunneling current exponentially decays with the increased tip-sample distance (z) as

$$I \sim U_b \rho_s E_F e^{-2kz}$$

where $I$ is tunneling current, $U_b$ is bias voltage, $\rho_s$ is the density of states of the sample, $E_F$ is the Fermi energy level and the k is the decay coefficient given by

$$\mathrm{k} = \sqrt{2\mathrm{m}\phi}\Big/\hbar$$

where m is mass of the electron, ϕ is the height of the energy barrier, and $\hbar$ is the Plank constant. Although the STM requires an immaculate surface of the samples and cannot be used on non-conductive samples, the exponential relationship between the tunneling current and tip-sample distance enables the achievement of a single atom imaging with a particular energy barrier[20].

### 4.3.2. Optical scanning probe design of AgNW/OF

TERS signals are proportional to the decrease of the tip-sample distance [21-22]. Therefore, STM was chosen as a feedback system for the demonstration of the feasibility of our plasmonic NW TERS probe due to the short scanning gap distance between the probe and samples. To electrically connect the AgNW to the feedback loop, tapered optical fiber tip was coated with a nail polish first. After then, 100nm Au was deposited on one side of the optical fiber. The nail polish was removed using acetone and the Au deposited on the top of the nail polish could be removed and the bare part of the optical fiber tip was used for the light coupling as shown in Figure 4.2. The methods for nanowire synthesis and tapering optical fiber are described in chapter 3.

#### 4.3.2.1.Removal of capping reagent on the surface of the plasmonic NW

As mentioned in the previous chapter, AgNW synthesized by polyol synthesis method has high crystallinity and atomically smooth surface. However, the capping agent (PVP) remains on the surface of AgNW and cannot be removed even after multiple rinsing. There have been several reports that demonstrated effective removal of PVP from the surface of

metal nanostructures[23-25]. In this work, we used $NaBH_4$ to remove the PVP from AgNW surface which was developed as a universal method for removing capping or functionalized molecules[26-27]. The mechanism is based on the replacement of the capping agent using a higher affinity of the hydride generated from $NaBH_4$ to the metal surface. Two obstacles must be solved to obtain a pure AgNW for TERS probe. First, we must prevent a quick re-adsorption of the PVP onto the AgNW surface due to the depletion of $NaBH_4$ after purification. Also, Ag can be easily oxidized during and after the PVP removal process. The oxidation of AgNW will finally result in a poor resolution of STM images and Raman enhancement. In this work, the removal of PVP from AgNW surface was conducted in a 4ml glass vial filled with a AgNW dispersed in 5mM $NaBH_4$. The vial was capped with a septa screw cap and purged with $N_2$ through syringe needles to prevent the oxidation of the AgNW. After 1 hours purification with $NaBH_4$, the aggregation of AgNWs can be observed in the vial, and the solution is refreshed with new $NaBH_4$ for the additional purification of the NWs for 1 or 2 hours. After then, only the aggregated NWs are transferred to another vial with a clean DI water, and the NWs are rinsed with DI water multiple times and finally stored in a deoxygenated ethanol solution. Here, the transferring only the aggregated AgNWs can reduce the re-adsorption of PVP on the surface of the NWs during the rinsing process, and oxidation of the AgNW was minimized by $N_2$ purgation. Figure 4.9 shows the measured tunneling current during 0.5nm movement toward to the substrate.

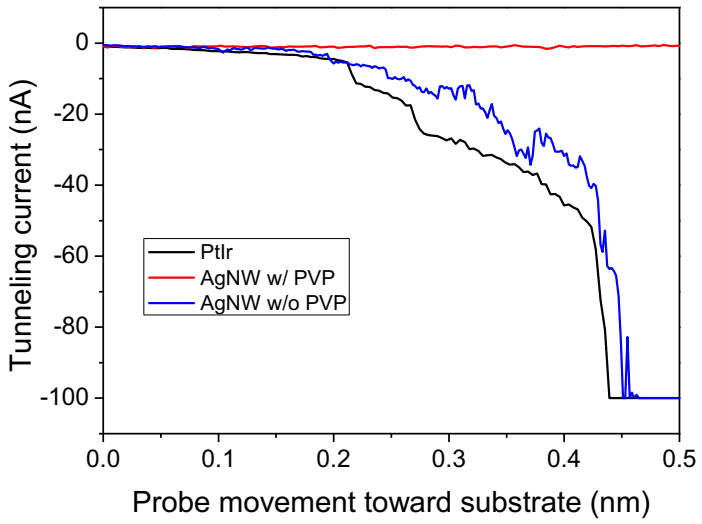


**Figure 4.9.** Tunneling currents with decreased gap distance between tips and samples by moving the tip toward to the substrate.

### 4.4. Demonstration of plasmonic nanofocusing TERS probe performance.

The adiabatic plasmonic nanofocusing of our probe with high transmission enables Raman signal collection through the same light path, for the excitation which ends up with making the NSOM equipment low-cost and straightforward because it does not require optical components used for focusing light nor a very careful tedious optical system alignment. Therefore, the first performance test of our plasmonic NW NSOM probe was aimed to demonstrate Raman signal collection using fiber-in and fiber-out (FIFO) configuration. As mentioned in the previous session, the gap distance in STM is dependent on the tunneling parameters. In this experiment, the current was constant (-1nA) and gap distance was controlled with adjustment of the bias. Figure 4.10(b) shows Raman spectra of R6G measured with different biases and clearly shows that the intensity increases with the

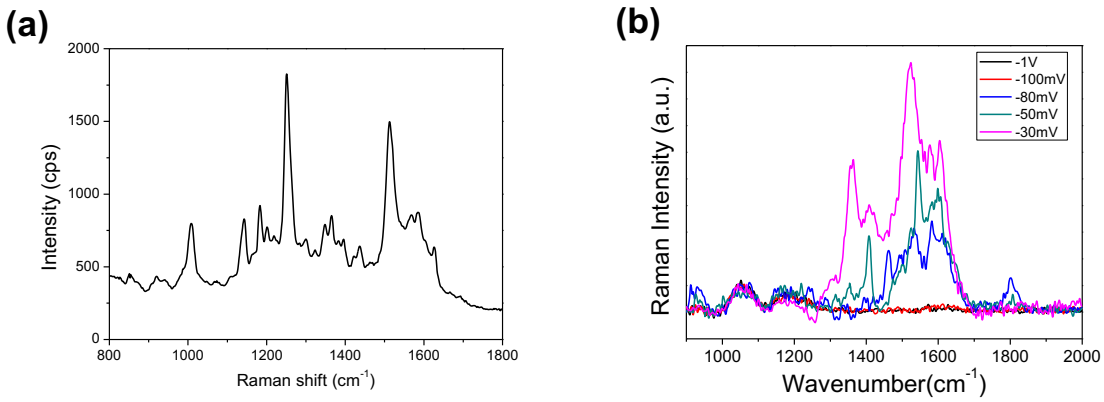


**Figure 4.10.** Raman spectra obtained with FIFO configuration. (a) Maximum count per seconds of 4-ATP Raman spectra. (b) Raman spectra of R6G as function of bias.

decrease of the bias. After optimizing the bias and tunneling current as well as laser output power(~1μW), the maximum Raman intensity of our plasmonic NW TERS with FIFO configuration was acquired using 4-Aminothiophenol monolayer on Au film. To the best of our knowledge, the signal intensity(1600cps) obtained here is the highest Raman intensity among the ones reported in the other studies. Moreover, the high signal intensity confirms the reversibility of the adiabatic nanofocusing at the junction between AgNW and optical fiber and it finally validates our FIFO configuration. This FIFO configuration with a high signal intensity obviates the need for complicated optical alignment and enables the simplification and lowering the cost of the NSOM or TERS system.

In the next step, we scanned SWCNTs on Au to demonstrate the spatial resolution of our probe. Here, the target samples were composed of 30% of conductive and 70% of semi-conductive SWCNTs. For this reason, a bias higher than the band gap of semi-conductive SWCNTs(-0.6V) was inevitable choice even if it would have resulted in lowering Raman intensity. The STM topography of SWCNTs on Au (111) is shown in Figure 4.11(a). The

STM image confirms that the mechanical stability of our plasmonic NW TERS probe is satisfactory. The sequential TERS spectra of SWCNTs acquired along the dotted line in

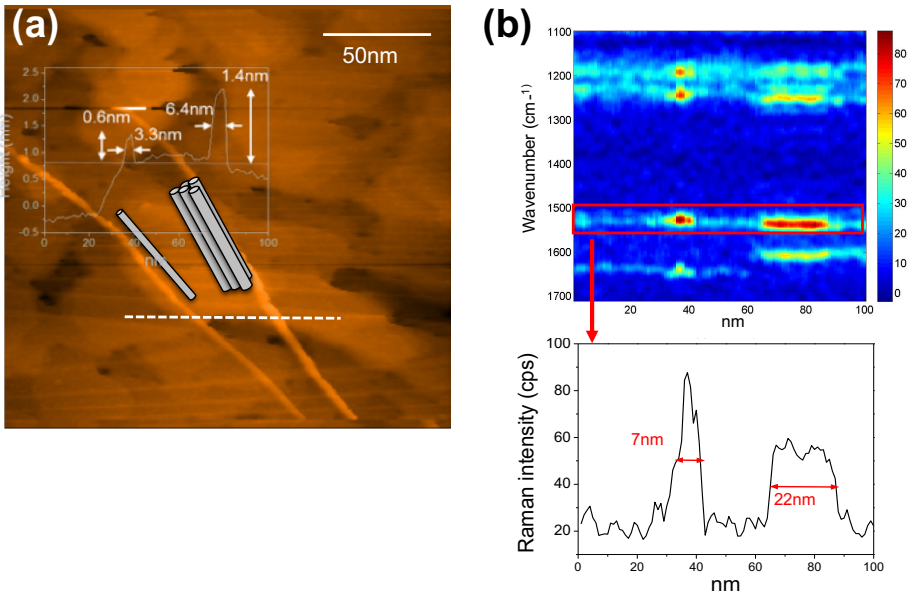


**Figure 4.11.** TERS spectra of SWCNTs using plasmonic NW TERS probe. (a) STM topography of SWCNTs on Au. (b) TERS line scanning of SWCNTs along the dotted line on the STM image (a).

Figure 4.11(a) are shown in Figure 4.11(b). The lateral resolution of the STM image is mainly determined by the AgNW tip radius while vertical resolution is directly related to the number of SWCNTs. Based on the thickness of the SWCNTs measured with the STM, the left one is single CNT and the other one is consist of at least more than five to satisfy measured both vertical and lateral thicknesses. With a single SWCNT, 7nm Raman resouliton was achieved with our plasmonic NW TERS probe. Reduction of Raman intensity was obserbed with multiple NWs due to the longer gap distance between TERS tip and Au film. Here, the spectra exhibit two clear bands at 1540cm$^{-1}$ and 1600~1630cm$^{-1}$ near the SWCNTs are located. The former one is G$^{-}$ band that appears typically at

1550cm$^{-1}$ with a conventional far-field Raman. For the first SWCNTs, the G peak appeared at ~1630cm$^{-1}$ while the second SWCNTs showed the peak at 1600cm$^{-1}$. G peak is usually observed at 1580~1590 cm$^{-1}$ with a conventional far-field Raman. In this experiment, the average diameter of the SWCNTs is around 0.8nm. This small diameter increases the van Hove singularities in the valence and conduction bands and may result in a blue energy shift of the G$^{-}$ band[28-30]. On the other hand, the red energy shift with G band was observed. The shift of the Raman peaks may come from the strong field gradients in the gap due to nano or pico cavity at the tip of AgNW or imperfectly flat or crystallized Au film. The gradient-field effect may also have activated IR active modes near 1180 and 1220cm$^{-1}$ due to molecular quadrupole transitions[31-33].

### 4.5. Conclusion

In this work, we introduce a novel adiabatic nanofocusing method to concentrate light to a nano-confined Raman sensing volume with high efficiency and energy throughput. Instead top-down grown metal tip used in the most of the nanofocusing methods in other groups, chemically synthesized AgNWs with high crystallinity and surface smoothness were used in this work to minimize the propagation loss of SPP to the apex of the probe. P polarization with a NW diameter around 200nm is the optimum condition for the selective excitation of the fundamental mode. Here, three different wavelength lasers were used to demonstrate broadband adiabatic nanofocusing of SPP. Generally, the coupling efficiencies for the all the three wavelengths were >40% which is 6 order higher than conventional aperture less NSOM and 2 order higher than recently developed adiabatic nanofocusing probes. Thanks

to the high coupling efficiency, this optical path can be used not only for concentrating of light to but also extracting Raman signal from the hot spot. Compared to a free space light focused with an objective lens, this NW waveguide works as a tunnel for light to propagate without a significant propagation loss due to a high absorption or diffraction in or reflection from the liquid sample. Therefore, imaging or sensing in the liquid phase is also available such as living cell analysis in culture media.

Lastly, controlling the movement of the NW tip over the sample maintaining a certain distance, the most challenging step, has been accomplished via integration of the nanofocusing probe with a commercial scanning probe microscope. And a successful scanning of SWCNTs with a Raman line scanning could have been accomplished. The transformative advances in light focusing and extracting is instrumental in increasing the prevalence of chemical imaging and analysis at nanoscale as a practical, reliable and powerful tool for researchers in materials science, catalysis, energy conversion, electronics and biology. This novel light focusing technique will be the pillar of the chemical imaging and analysis at nanoscale and contribute to innovative findings in diverse scientific fields in the future.

## 4.6. References


1. Rayleigh, J. W. S. B., *Investigations in Optics, with Special Reference to the Spectroscope*. 1879.

2. Abbe, E., Beiträge zur Theorie des Mikroskops und der mikroskopischen Wahrnehmung. *Archiv f. mikrosk. Anatomie* **1873,** *9* (1), 413-418.

3. Synge, E., XXXVIII. A suggested method for extending microscopic resolution into the ultra-microscopic region. *The London, Edinburgh, and Dublin Philosophical Magazine and Journal of Science* **1928,** *6* (35), 356-362.

4. Hartschuh, A., Tip-Enhanced Near-Field Optical Microscopy. *Angew. Chem. Int. Ed.* **2008,** *47* (43), 8178-8191.

5. Saiki, T. In *Recent advances in near-field optical microscopy*, Microprocesses and Nanotechnology Conference, 2002. Digest of Papers. Microprocesses and Nanotechnology 2002. 2002 International, 6-8 Nov. 2002; 2002; pp 6-7.

6. Valaskovic, G. A.; Holton, M.; Morrison, G. H., Parameter control, characterization, and optimization in the fabrication of optical fiber near-field probes. *Appl. Opt.* **1995,** *34* (7), 1215-1228.

7. Novotny, L.; Pohl, D. W.; Hecht, B., Scanning near-field optical probe with ultrasmall spot size. *Opt. Lett.* **1995,** *20* (9), 970-972.

8. Mauser, N.; Hartschuh, A., Tip-enhanced near-field optical microscopy. *Chem Soc Rev* **2014,** *43* (4), 1248-1262.

9. Ropers, C.; Neacsu, C.; Elsaesser, T.; Albrecht, M.; Raschke, M.; Lienau, C., Grating-coupling of surface plasmons onto metallic tips: a nanoconfined light source. *Nano letters* **2007,** *7* (9), 2784-2788.

10. Bao, W.; Melli, M.; Caselli, N.; Riboli, F.; Wiersma, D.; Staffaroni, M.; Choo, H.; Ogletree, D.; Aloni, S.; Bokor, J., Mapping local charge recombination heterogeneity by multidimensional nanospectroscopic imaging. *Science* **2012,** *338* (6112), 1317-1321.

11. Tugchin, B. N.; Janunts, N.; Klein, A. E.; Steinert, M.; Fasold, S.; Diziain, S. v.; Sison, M.; Kley, E.-B.; Tünnermann, A.; Pertsch, T., Plasmonic tip based on excitation of radially polarized conical surface plasmon polariton for detecting longitudinal and transversal fields. *ACS Photonics* **2015,** *2* (10), 1468-1475.

12. Tuniz, A.; Chemnitz, M.; Dellith, J.; Weidlich, S.; Schmidt, M. A., Hybrid-mode-assisted long-distance excitation of short-range surface plasmons in a nanotip-enhanced step-index fiber. *Nano letters* **2017,** *17* (2), 631-637.

13. Yan, R.; Pausauskie, P.; Huang, J.; Yang, P., Direct photonic–plasmonic coupling and routing in single nanowires. *P Natl Acad Sci USA* **2009,** *106* (50), 21045-21050.

14. Narayanan, S.; Cheng, G.; Zeng, Z.; Zhu, Y.; Zhu, T., Strain hardening and size effect in five-fold twinned Ag nanowires. *Nano letters* **2015,** *15* (6), 4037-4044.

15. Zhu, Y.; Qin, Q.; Xu, F.; Fan, F.; Ding, Y.; Zhang, T.; Wiley, B. J.; Wang, Z. L., Size effects on elasticity, yielding, and fracture of silver nanowires: In situ experiments. *Physical review B* **2012,** *85* (4), 045443.

16. Antunes, P.; Domingues, F.; Granada, M.; André, P., Mechanical properties of optical fibers. In *Selected Topics on Optical Fiber Technology*, InTech: 2012.

17. Pigeon, F.; Pelissier, S.; Mure-Ravaud, A.; Gagnaire, H.; Veillas, C., Optical fibre Young modulus measurement using an optical method. *Electronics Letters* **1992,** *28* (11), 1034-1035.

18. Ma, X.; Zhu, Y.; Kim, S.; Liu, Q.; Byrley, P.; Wei, Y.; Zhang, J.; Jiang, K.; Fan, S.; Yan, R., Sharp-Tip Silver Nanowires Mounted on Cantilevers for High-Aspect-Ratio High-Resolution Imaging. *Nano letters* **2016,** *16* (11), 6896-6902.

19. Edwards, H.; Taylor, L.; Duncan, W.; Melmed, A. J., Fast, high-resolution atomic force microscopy using a quartz tuning fork as actuator and sensor. *Journal of applied physics* **1997,** *82* (3), 980-984.

20. Hansma, P. K.; Tersoff, J., Scanning tunneling microscopy. *Journal of Applied Physics* **1987,** *61* (2), R1-R24.

21. Zhang, R.; Zhang, Y.; Dong, Z.; Jiang, S.; Zhang, C.; Chen, L.; Zhang, L.; Liao, Y.; Aizpurua, J.; Luo, Y. e., Chemical mapping of a single molecule by plasmon-enhanced Raman scattering. *Nature* **2013,** *498* (7452), 82.

22. Zhang, Y.; Voronine, D. V.; Qiu, S.; Sinyukov, A. M.; Hamilton, M.; Liege, Z.; Sokolov, A. V.; Zhang, Z.; Scully, M. O., Improving resolution in quantum subnanometre-gap tip-enhanced Raman nanoimaging. *Scientific reports* **2016,** *6*, 25788.

23. Long, N. V.; Ohtaki, M.; Nogami, M.; Hien, T. D., Effects of heat treatment and poly (vinylpyrrolidone)(PVP) polymer on electrocatalytic activity of polyhedral Pt nanoparticles towards their methanol oxidation. *Colloid and Polymer Science* **2011,** *289* (12), 1373-1386.

24. Ye, J.-Y.; Attard, G. A.; Brew, A.; Zhou, Z.-Y.; Sun, S.-G.; Morgan, D. J.; Willock, D. J., Explicit Detection of the Mechanism of Platinum Nanoparticle Shape Control by Polyvinylpyrrolidone. *The Journal of Physical Chemistry C* **2016,** *120* (14), 7532-7542.

25. Wang, J.; Jiu, J.; Araki, T.; Nogi, M.; Sugahara, T.; Nagao, S.; Koga, H.; He, P.; Suganuma, K., Silver nanowire electrodes: conductivity improvement without post-treatment and application in capacitive pressure sensors. *Nano-Micro Letters* **2015,** *7* (1), 51-58.

26. Ansar, S. M.; Ameer, F. S.; Hu, W.; Zou, S.; Pittman Jr, C. U.; Zhang, D., Removal of molecular adsorbates on gold nanoparticles using sodium borohydride in water. *Nano letters* **2013,** *13* (3), 1226-1229.

27. Luo, M.; Hong, Y.; Yao, W.; Huang, C.; Xu, Q.; Wu, Q., Facile removal of polyvinylpyrrolidone (PVP) adsorbates from Pt alloy nanoparticles. *Journal of Materials Chemistry A* **2015,** *3* (6), 2770-2775.

28. Jorio, A.; Pimenta, M.; Souza Filho, A.; Saito, R.; Dresselhaus, G.; Dresselhaus, M., Characterizing carbon nanotube samples with resonance Raman scattering. *New Journal of Physics* **2003,** *5* (1), 139.

29. Dresselhaus, M. S.; Dresselhaus, G.; Saito, R.; Jorio, A., Raman spectroscopy of carbon nanotubes. *Physics reports* **2005,** *409* (2), 47-99.

30. Piscanec, S.; Lazzeri, M.; Robertson, J.; Ferrari, A. C.; Mauri, F., Optical phonons in carbon nanotubes: Kohn anomalies, Peierls distortions, and dynamic effects. *Physical Review B* **2007,** *75* (3), 035427.

31. Sun, M.; Fang, Y.; Zhang, Z.; Xu, H., Activated vibrational modes and Fermi resonance in tip-enhanced Raman spectroscopy. *Physical Review E* **2013,** *87* (2), 020401.

32. Moskovits, M.; DiLella, D., Intense quadrupole transitions in the spectra of molecules near metal surfaces. *The Journal of Chemical Physics* **1982,** *77* (4), 1655-1660.

33. Ayars, E.; Hallen, H.; Jahncke, C., Electric field gradient effects in Raman spectroscopy. *Physical review letters* **2000,** *85* (19), 4180.

# Chapter 5

# Summary and Future Directions

## 5.1. Summary

In chapter 1, nanowire waveguides, including dielectric and plasmonic nanowires were reviewed in the aspect of the optical properties, synthesis routes, and pros and cons regarding their applications. Dielectric nanowire waveguides have advantages over metallic waveguides in chemical and thermal stability and no ohmic loss. Therefore, the dielectric nanowire especially semiconducting nanowire has a high potential in the generation of light and guidance of light for a long distance data communication. On the other hand, metallic waveguides have a great ability to confine the electromagnetic fields in the vicinity of the surface which can be exploited for sensing or compositional analysis using vibrational spectroscopy.

In chapter 2, the propagating surface plasmon polaritons (PSPPs) modes in AgNW were investigated, and one of the analysis methods to decouple the two lowest order modes was introduced. The PSPPs were excited by contacting a tapered optical fiber along a AgNW and the scattering light at the end of the AgNW was measured. The intensity oscillations of the far-field signals originating from beating between two SPP modes were observed. We fitted the experimental beating pattern profiles using our model and successfully decoupled and investigated the properties of the two lowest order modes in AgNW. The results confirm that the chemically synthesized AgNWs has a lower propagation loss than

the ones measured on a polycrystalline thin film due to a better surface roughness and domain boundaries of the nanowires. The derived power ratio of the two modes shows that the fundamental mode is dominated with a nanowire diameter smaller than 300nm while the second-order mode is dominated by thicker NWs.

In chapter 3, the plasmonic nanowire waveguide, here AgNW, was utilized for label-free quantitative sensing of intracellular biomolecules in the single living cell. The PSPPs were excited by coupling AgNW with a tapered optical fiber. We developed a novel method to attach silver nanocube (AgNC) cavity at the tip of AgNW, and a remarkable enhancement of the Raman intensity by the AgNC cavity has been demonstrated. Even with the integration of AgNCs with the plasmonic nanowire endoscopy probe, the tip diameter of the probe could be maintained less than 250nm because AgNW does not suffer from diffraction limit. This plasmonic nanowire waveguide exhibits better guidance of the light in a high refractive index environment such as water or cells compared to the dielectric waveguide. Using the AgNC nanocavity antenna coupled plasmonic nanowire endoscopy probe, the pH in HeLa Cells was measured for the first time.

In chapter 4, the plasmonic nanowire waveguide was utilized as a near-field scanning optical microscopy (NSOM) probe. Differently from chemical sensing in chapter 3, here, selective excitation of the SPP modes in AgNW is required to achieve high spatial resolution. Also, the AgNW tip must be sharp to confine a strong electromagnetic fields at the tip. We also needed to find a cross point of the taper angle that provides a high enough coupling efficiency and mechanical stability. The results show that p polarized excitation, AgNW diameters thicker than 140nm, taper angles higher than 6 for the 532nm laser is

prerequisite for the selective excitation of the fundamental mode. Generally, the coupling efficiency at the excitation condition is higher than 40% which is three orders higher than that of recently developed so-called adiabatic nanofocusing probes. Such a high coupling efficiency allows for near-field scanning without objective lens and optic alignment using fiber-in fiber-out configuration which collects the signal from the AgNW tip with a same light path for the incident light. This is a remarkable advance in the near-field scanning microscopy because it will reduce the equipment cost significantly and requires less operating skills. We believe that the probe will contribute to the popularization of the NSOM. The probe also has the capability of broadband adiabatic nanofocusing which is experimentally challenging for the other adiabatic nanofocusing methods.

**5.2. Future directions.**

In my dissertation, the studies were focused on understanding the principle and optimization of adiabatic nanofocusing using plasmonic nanowire/tapered optical fiber. Although two practical performances of the probe were demonstrated in the field of biosensing and NSOM, we just took our first step toward the chemical sensing and imaging using this probe. Therefore, the future works will be more focused on the application of this probe to diverse research areas. The two major directions could be as follows.

5.2.1. Development of smart nanoprobe with a capability of cargo delivery and multiplex analysis and extend understanding of intracellular processes.

AgNCs functionalized with different Raman indicators can be prepared separately and be attached to a plasmonic nanowire endoscopy probe using a method developed in chapter 3. Instead of chemical analysis in normal living cells, the probe can deliver chemicals into the living cells such as specific biomolecules, pathogen, or drugs into living cells and monitor the cell response by sensing multi-chemical species simultaneously. The probe fabrication is straightforward. The AgNCs functionalized with different Raman indicators can be prepared separately and attached to a plasmonic nanowire endoscopy probe sequentially or simultaneously.

### 5.2.2. Application of the plasmonic nanowire NSOM probe for material characterization

NSOM probes relying on the objective lens to focus incident light can be only applied to solid samples in a gas environment. On the other hand, our adiabatic nanofocusing configuration can image samples in the liquid environment because the incident light or Raman signal is guided through the NW and OF. Thus, it does not suffer from absorption or diffraction in or reflection from the liquid. We expect many discoveries in catalyst and biomaterials by imaging the samples in the liquid environment.